Numerical investigation of particle deposition in a turbulent boundary layer with forced turbulence in the external flow

Étude numérique du dépôt de particules dans une couche limite avec un forçage turbulent dans la zone externe

THÈSE

présentée et soutenue publiquement le 10 Décembre 2019

pour l'obtention du titre de

Docteur de l'Université de Lorraine

(mention Science des matériaux)

par

Manoj JOISHI

Composition du jury

Rapporteurs :	Jochen FRÖHLICH	Professeur Technische Universität Dresden, Allemagne
	Hervé DUVAL	Professeur École Centrale Supélec Université Paris Saclay
Examinatrices :	Agathe CHOUIPPE	Maître de conférences Icube, Université de Strasbourg
	Nathalie MONNIER	Maître de conférences LRGP, Université de Lorraine
Invités :	Sean SANDERS	Professeur Université d'Alberta, Canada
	Boris ARCEN	Maître de conférences LEMTA, Université de Lorraine
Directeur de thèse :	Jean-Pierre BELLOT	Professeur IJL, Université de Lorraine
Co-directeur de thèse :	Jean-Sébastien KROLL-RABOTIN	Maître de conférences IJL, Université de Lorraine

Institut Jean Lamour-UMR 7198-CNRS, LabEx DAMAS
Campus Artem, 2 allée André Guinier, 54011 Nancy

Abstract

Deposition of particles on a wall plays a significant role in fluid-solid processes such as inclusions recovery from liquid steel in ladle furnace, that controls inclusion cleanliness upstream from solidification. The aim of this work is to study the turbulent deposition and capture of particles on a wall, in a situation where turbulence in the boundary layer originates both from wall shear and from agitation in the external flow. In a ladle furnace, such an agitation would result from bubble injection.

A framework for simulations at mesoscopic scale in which particles are represented as points but the turbulence is fully resolved has been developped using an in-house solver, where a Lattice Boltzmann Method (LBM) solves flow dynamics and linear isotropic forcing generates artificial turbulence. Lagrangian Particle Tracking (LPT) is used to achieve one way coupling between particle motions and turbulent flow. These numerical methods were applied to Direct Numerical simulation (DNS) of a fully developed turbulent boundary layer in which particles smaller than the Kolmogorov length scale are introduced. The deposition mechanisms in aerosol conditions have been analyzed and quantified into a statistical law for deposition velocity in terms of Stokes number, and validated against data from the literature.

Such simulations have provided a better understanding of deposition and capture mechanisms, depending on the turbulent flow in a wall boundary layer and on particle physical properties. Also, preliminary simulations in hydrosol conditions that match actual ladle operation have shown that the framework developed in this work can be applied to investigate inclusion behaviour in secondary steelmaking although statistical analysis in this work focused on aerosols.

Résumé

Le dépôt de particules sur une paroi joue un rôle significatif dans les procédés polyphasiques fluide-solides, tels que la séparation inclusionnaire dans les poches d'acier liquide en métallurgie secondaire qui permettent de contrôler la propreté du métal avant solidification. L'objectif de ce travail est d'étudier le dépôt turbulent et la capture de particules sur une paroi, dans des situations où la turbulence au sein de la couche limite est produite à la fois par la contrainte pariétale et par les forces d'agitation du bain liquide loin de cette paroi.

Les simulations sont mises en œuvre à l'échelle mésoscopique, en considérant des particules ponctuelles mais avec une turbulence complètement résolue. Un code de simulation maison a été développé, utilisant une méthode de Boltzmann sur réseau pour résoudre la dynamique de l'écoulement et en appliquant un forçage linéaire isotrope pour générer artificiellement la turbulence loin de la paroi. Le suivi lagrangien de particules permet enfin d'établir un couplage faible entre le mouvement des particules et l'écoulement turbulent. Ces techniques numériques ont été appliquées à la simulation directe d'une couche limite turbulente dans laquelle les particules de taille plus petite que l'échelle de Kolmogorov sont introduites. Les mécanismes de dépôt pour des aérosols ont été analysés et une loi statistique de vitesse de dépôt en fonction du nombre de Stokes a été extraite et comparée à la littérature.

L'ensemble de ces simulations permet une meilleure compréhension des mécanismes de dépôt et de capture, en fonction de la turbulence du fluide au sein de la couche limite et des propriétés des particules. De plus, les résultats préliminaires obtenus pour des particules hydrosols, qui correspondent à des conditions qui prévalent pour des inclusions dans les poches d'acier liquide, ont montré que l'outil numérique peut être appliqué à l'étude quantitative de la capture inclusionnaire aux parois des réacteurs métallurgiques.

Contents

Acknowledgments

I would like to thank my director and co-director, Jean-Pierre Bellot and Jean-Sébastien Kroll-Rabotin for their trust and their support throughout the duration of the thesis. I am also very grateful to you for having me here and giving me the opportunity to perform my research work and completing my doctorate degree here in Nancy, France.

I address my heartful thanks and appreciation to Hervé Duval and Jochen Fröhlich for accepting to be members of the jury as "rapporteurs". Their questions, comments and remarks have immensely helped me to improve the thesis. Also, I would like to thank my "examinatrices" and "invités" Agathe Chouippe, Nathalie Monnier, Sean Sanders and Boris Arcen for examining my thesis and giving me corrections and reviews so that I could prepare a better version of my final manuscript.

My thanks go of course to Team 301 and the development process team and my working colleagues in general, for their patience, motivation, support, humor and fun times. Very sincere thanks to Matthieu, Rayan, Martin, Ilia, Marvin, Edgar, Julien, Léa, Bassem, Shantanu and so many others to be there with me through the course of my PhD. I hope to keep in touch with you in the future. I would like to thank my friends from India, Afeef, Anurag, Chaitanya, Geetesh and Nitin with whom I had studied together. You guys have really been an inspiration to me and have provided constant support and motivation in my entire work.

From the depth of my heart, I would like to thank my family, especially my parents, my brother and my relatives without whom it is certain that this work would not have happened. They were able to provide logistical support, and above all boosted my morale when I faced difficulties and uncertainities in my research work. Thank you for encouraging me in delicate moments and allowing me to become what I am today.

Finally, I would also like to thank the people of the ASCNB Badminton group along with Marvin and Celina, with whom I have played the 2017–18 season and experienced good sportive moments outside the world of research.

To finish, I thank the people who do not find themselves in these lines and who think they deserve it.

Nomenclature

Symbols	Definition	Units
Operators		
$\bar{\cdot}$	mean value	–
$\langle \cdot \rangle^V$	volume average	–
∇^2	Laplacian operator	–
$[\cdot]$	lattice unit ([lu] for length, [tu] for time)	–
Indices		
0	control value (turbulence forcing parameter)	–
f	fluid property expressed in physical units	–
LBM	LBM quantity, flow property expressed in lattice units	–
PS	flow property expressed in pseudo-spectral units	–
phys	quantity expressed in physical units	–
Exponents		
$^+$	dimensionless quantity (relative to corresponding turbulence chacateristic scale)	–
$'$	turbulent fluctuation	–
Latin		
A	turbulence linear forcing coefficient	s^{-1}
A_p	cross sectional area of particle	m^2
$\vec{c}_i$	lattice velocity associated to direction i	$\mathrm{m\ s}^{-1}$ or [lu]/[tu]

c_s	lattice speed of sound	m s^{-1} or [lu]/[tu]
C	any flow property varying with space and time	–
C_M	added mass coefficient	–
C_O	total oxygen content	–
C_p	concentration of particles	# m^{-3}
C_p^*	dimensionless concentration of particles	–
$\bar{C}_{p0}$	mean concentration of particles over the entire domain	m^{-3}
C_{SL}	lift coefficient	–
d_p	particle diameter	m
D_B	Brownian diffusivity	m^2 s^{-1}
D_T	turbulent diffusivity	m^2 s^{-1}
D	diffusion coefficient in calculation of turbulence statistics	m^2 s^{-1}
e	displacement in origin of velocity profile due to wall roughness	m
E	density of kinetic energy	m^3 s^{-2}
$\vec{f}$	volumic forces acting on the fluid	N
F_i	source term in lattice Bolzmann equation	N
$\vec{F}_p$	forces acting on particle	N
$\vec{F}_B$	buoyancy force	N
$\vec{F}_D$	drag force	N
$\vec{F}_A$	added mass force	N
$\vec{F}_P$	pressure gradient resulting force	N
$\vec{F}_L$	lift force	N
$\vec{g}$	gravity acceleration	m s^{-2}
h	roughness height	m
H_{phys}	length of an edge of the simulated domain	m

J	diffusion flux of particles	$\mathrm{m}^{-2}\ \mathrm{s}^{-1}$
k	turbulent kinetic energy	$\mathrm{m}^{2}\ \mathrm{s}^{-2}$
K_O	kinetic constant	min^{-1}
L	integral length scale in turbulent flow	m
L_D	length scale of dissipation range	m
L_E	length scale of inertial range	m
m_i	weight associated to direction i of the lattice	–
m	mass	kg
m_p	mass of particle	kg
$\vec{n}$	unit normal vector	–
N_i	lattice Boltmann distribution associated to lattice direction i	–
N_i^{eq}	lattice Boltzmann distribution at equilibrium	–
N_x, N_y, N_z	number of fluid nodes in streamwise, spanwise and wall normal directions	–
N_p	number of particles	–
N_{wall}	number of particles deposited on the wall	–
p	pressure	Pa
$[P]$	projection matrix	–
q	second space derivative of strain rate	$\mathrm{m}^{-2}\ \mathrm{s}^{-2}$
Q	second invariant of velocity gradient tensor	s^{-2}
$\mathbf{Re}$	Reynolds Number	–
$Re_{\mathbf{T}}$	friction Reynolds number	–
Re_θ	Reynolds number based on momentum thickness	–
Re_h	Reynolds number based on channel flow height	–
Re_L	Reynolds number associated with larger eddies	–
Re_{force}	forcing Reynolds number	–

Re_λ	Taylor's Reynolds number	–
Re_s	shear Reynolds number	–
Re_p	particle Reynolds number	–
S_u	velocity derivative skewness	–
S_{ij}	strain rate tensor	–
S_{xy}	surface area where particles are deposited	m^2
$\mathbf{Sc}$	Schmidt number	–
t	time	s
t_p	particle time (appears as Δt_p, particle motion integration time step)	s
t_{sam}	sampling period	s
t^*	characteristic time calculated based on friction velocity	s
$\mathbf{T}$	shear stress	Pa
$\mathbf{T}_w$	wall shear stress	Pa
u	velocity	m s^{-1}
$u_\mathbf{T}$	friction velocity	m s^{-1}
u_d	deposition velocity	m s^{-1}
u_i	instantaneous velocity	m s^{-1}
u_L	integral velocity scale in turbulent flow	m s^{-1}
u_η	Kolmogorov velocity scale in turbulent flow	m s^{-1}
u_{rms}	RMS of fluctuation velocity	m s^{-1}
$\vec{u}_p$	particle velocity	m s^{-1}
V_i	volume of bin i	m^3
V_T	total volume of the simulation domain	m^3
w_p	wall normal particle velocity	m s^{-1}
x, $\vec{x}$	position	m

$\vec{x}_p$	particle location	m
z	distance from the wall	m
z_c	distance of capture	m

Greek

α	force coefficient applied to particle acceleration	N m^{-1} s^2
β	force coefficient applied to particle velocity	N m^{-1} s
γ	force contribution independent from particle motion	N
Δ	discrete step	–
δ_ν	viscous length / wall unit	m
δ	the boundary layer thickness	m
ϵ	turbulent dissipation rate	m^2 s^{-3}
η	Kolmogorov length scale	m
κ	wave vector	m^{-1}
$\varkappa$	Von Karman constant	–
λ	Taylor microscale	m
λ_z	spacing between turbulent structures at the wall	m
Λ	solution vector in LBM	–
Λ^-	pre-collision solution vector in LBM	–
Λ^+	post-collision solution vector in LBM	–
μ	dynamic viscosity of fluid	Pa s
ν	kinematic viscosity of fluid	m^2 s^{-1}
$\vec{\omega}$	vorticity	s^{-1}
Ω_i	collision operator contribution along lattice direction i	–
$\Omega_i^{\text{E\&S}}$	collision operator defined by Eggels and Somers [1]	–
Ω_i^{BGK}	collision operator defined by Bhatnagar et al. [2]	–
Ω_{ij}	rotation rate tensor	s^{-1}

$\vec{\Omega}$	rotation vector	s^{-1}
ϕ_i	eigen vectors	–
ρ	density	kg m^{-3}
ρ_p	particle density	kg m^{-3}
σ_h	standard deviation of roughness	m
τ	integral time scale in turbulent flow, eddy turnover time	s
$\bar{\bar{\tau}}$	viscous stress tensor	Pa
τ_η	Kolmogorov time scale in turbulent flow	s
τ_p	particle response time	s
${\tau_p}^+$	Stokes number (dimensionless particle response time)	–
τ^{BGK}	relaxation in BGK collision operator	–
$(\varphi_p)_{wall}$	flux density of particles	m^{-2} s^{-1}

Résumé en français

Étude numérique du dépôt de particules dans une couche limite avec un forçage turbulent dans la zone externe

Introduction

La propreté inclusionnaire demeure un enjeu majeur des opérations de traitement du métal liquide, afin de garantir des propriétés mécaniques élevées des alliages métalliques élaborés. Par exemple, dans un acier bas carbone, 1 kg d'acier contient de 10^7 à 10^9 inclusions, distribuées en taille selon une loi log-normale, comme le montre la figure 1a. Malgré cette importante densité numérale d'inclusions, la fraction massique demeure très faible (de l'ordre de 10^{-5}), c'est-à-dire 10 ppm d'inclusions non-métalliques dans les aciers liquides. Comme on peut le voir dans la figure 1b, une taille classique d'inclusion se trouve entre 1 et 20 µm, et seules très rares particules ont une taille supérieure à 100 µm.

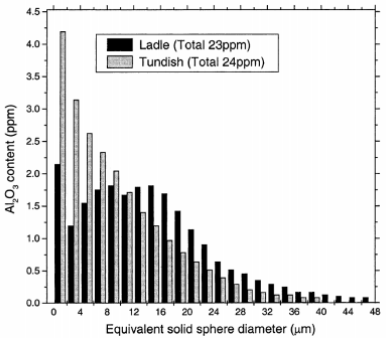

Figure 1 a : Distribution en taille dans un acier bas carbone en poche et au répartiteur.

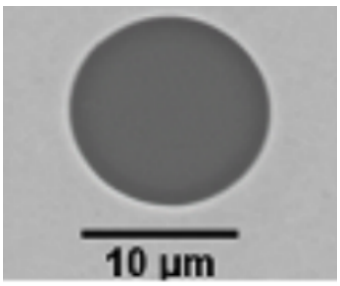

Figure 1 b : Micrographie d'une inclusion Ca_x-Al_2O_{3y} dans un acier calmé à l'aluminium.

Parmi les mécanismes qui influent sur la propreté inclusionnaire, le dépôt de particules sur une paroi joue un rôle significatif dans les poches d'acier liquide en métallurgie secondaire, qui permettent d'éliminer des particules du métal avant solidification. La paroi dans le cas des poches de traitement est soit l'interface avec la couche de laitier ou la surface des parois réfractaires du réacteur, comme le montre schématiquement la figure 2. L'objectif de

ce travail est d'étudier le dépôt turbulent et la capture de particules sur une paroi, dans des situations où la turbulence au sein de la couche limite est produite à la fois par la contrainte pariétale et par les forces d'agitation du bain liquide loin de cette paroi (induites par le fort bullage d'argon dans la poche).

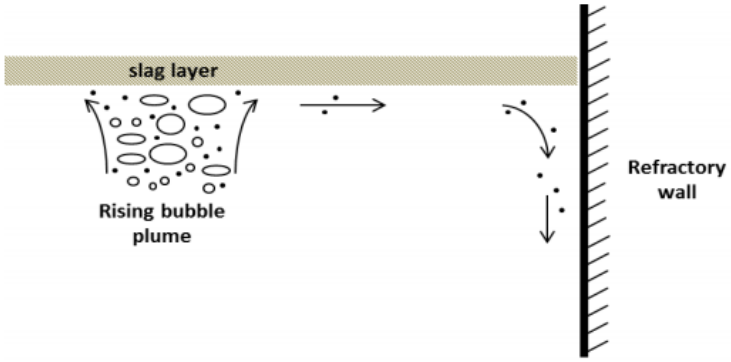

Figure 2 : Schéma du comportement d'une inclusion dans le panache de bulles et à proximité de la couche de laitier et de la paroi réfractaire du réacteur

Méthodologie

Les simulations sont mises en œuvre à l'échelle mésoscopique, en considérant des particules ponctuelles mais avec une turbulence complètement résolue. Un code de simulation maison a été développé, utilisant une méthode de Boltzmann sur réseau pour résoudre la dynamique de l'écoulement et en appliquant un forçage linéaire isotrope pour générer artificiellement la turbulence loin de la paroi. Le suivi lagrangien de particules permet enfin d'établir un couplage faible entre le mouvement des particules et l'écoulement turbulent. Ces techniques numériques ont été appliquées à la simulation directe d'une couche limite turbulente dans laquelle les particules de taille plus petite que l'échelle de Kolmogorov sont introduites.

Une démarche par étape a été suivie tout au long de ce travail de doctorat, comme le montre la figure 3. Après avoir mis au point un forçage linéaire isotrope pour générer la turbulence (1ère étape), la simulation directe de la turbulence près d'une paroi a été mise en place (2ème étape). Deux régions sont sélectionnées, la région haute (voir figure 3) où la turbulence est générée artificiellement, et la région basse où se positionne la paroi et où la turbulence est produite par la contrainte pariétale. Puis dans une 3ème étape, des particules fluides (traceurs) sont introduites dans le domaine pour vérifier le bon fonctionnement du suivi lagrangien. Enfin dans une 4ème étape, des particules (aérosols et hydrosols) sont introduites pour analyser les mécanismes de transport des particules vers la paroi, les accumulations de particules en proche paroi ainsi que les dépôts à la paroi.

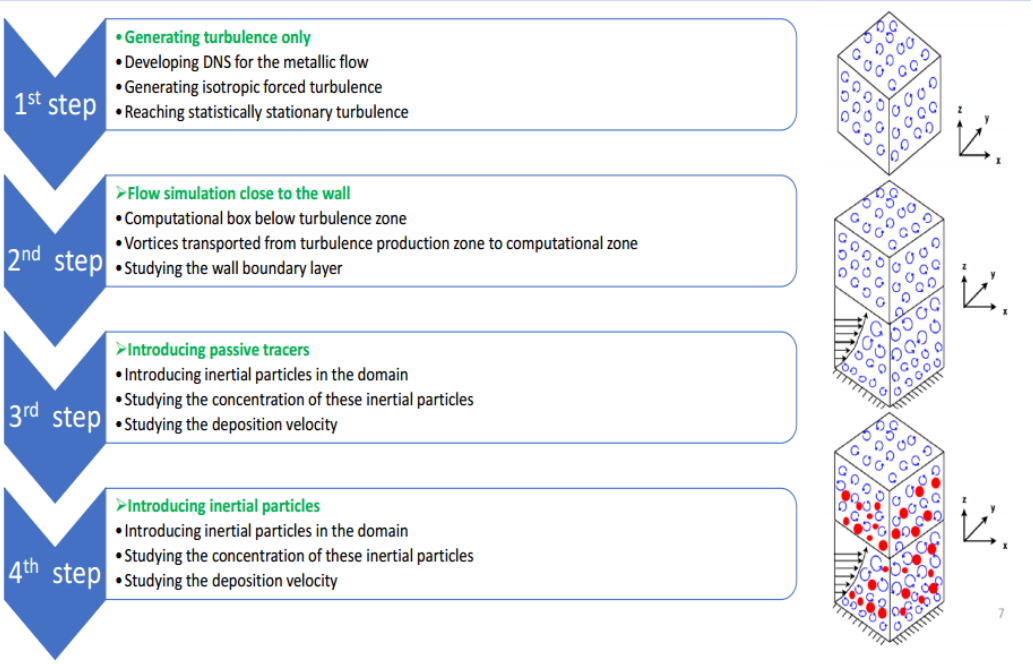

Figure 3 : Méthodologie suivie pendant la thèse.

Résultats

Le travail réalisé a permis dans un premier temps de simuler l'écoulement turbulent en proche paroi (illustrée sur la figure 4), dans des conditions représentatives des procédés d'élaboration métallurgique.

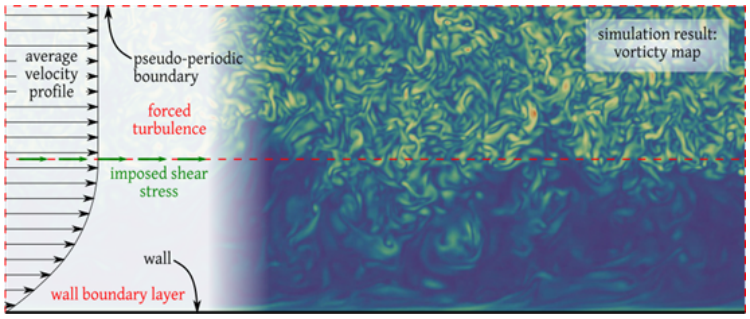

Figure 4 : Illustration schématique et résultat de simulation d'une couche limite turbulente.

Les résultats en termes de vitesses moyennes et de RMS des vitesses fluctuantes sont en bon accord avec ceux obtenus notamment par Moser [1] à proximité de la paroi, pour $z^+ < 100$. Des structures turbulentes ont été mises en évidence à proximité de la paroi, qui apparaissent, le long de chemins dans la direction de l'écoulement principal, sous la forme de tourbillons enroulés dans la direction perpendiculaire. Ces structures connues sous le vocable de 'streak' et de 'horseshoe', dont un exemple est reporté sur la figure 5, sont bien caractéristiques des écoulements turbulents en canal.

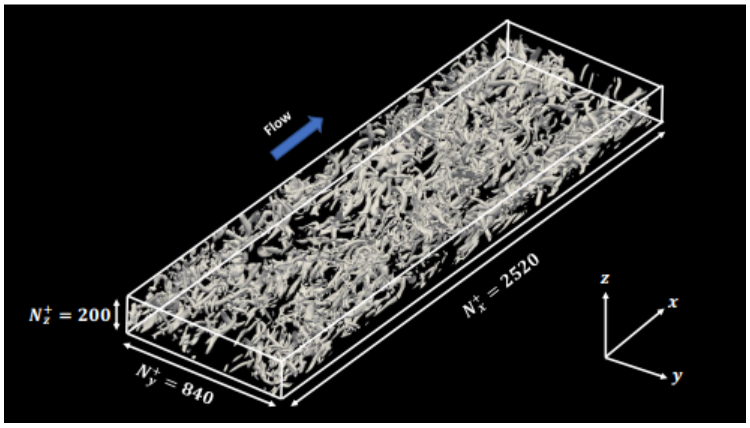

Figure 5 : Iso contours du second invariant du tenseur de gradient de vitesse, $Q^+ = 0,028$.

Les simulations de dépôts turbulents d'aérosols ont permis de calculer la vitesse de dépôt en fonction du nombre de Stokes. La courbe obtenue (figure 6) est en bon accord avec les résultats de la littérature, qu'ils soient numériques ou expérimentaux. On observe bien une augmentation forte du flux déposé avec le nombre de Stokes pour des valeurs de τ_p^+ allant de 0,1 à 20, puis une stabilisation pour des valeurs supérieures.

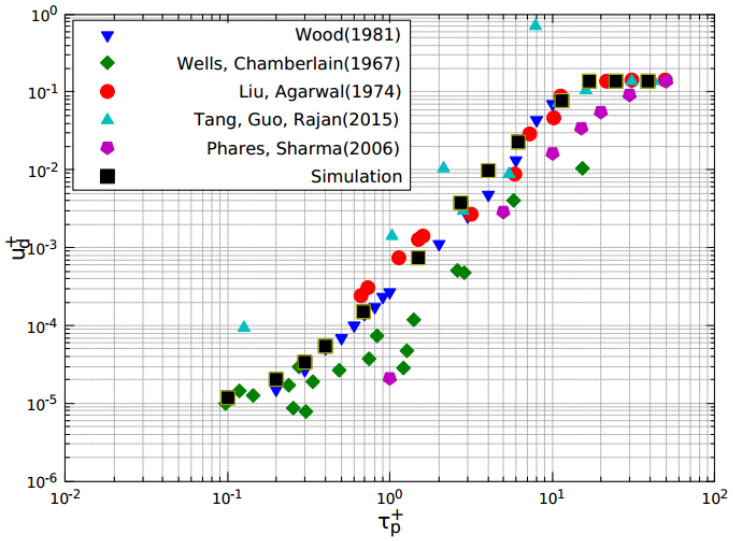

Figure 6 : Vitesse de dépôt d'aérosols en fonction du nombre de Stokes dans un système de coordonnées adimensionnées. Comparaison avec la littérature.

L'accumulation de particules a été clairement mise en évidence à proximité de la paroi ($z^+ < 3$), comme souligné par d'autres auteurs [2,3], et le pic de concentration augmente lorsque l'inertie des particules diminue. Ce comportement s'explique par l'amortissement de la vitesse normale à la paroi des particules ainsi que des fluctuations de vitesses lorsque l'inertie des particules est faible (par exemple $\tau_p^+ = 0,2$). Enfin, les zones préférentielles de dépôt reflètent les régions principales d'accumulation, et correspondent aux chemins

('streaks') observés dans la direction de l'écoulement où la vitesse est réduite. Des simulations ont été engagées pour des hydrosols, en considérant l'ensemble des forces agissant sur les inclusions, force de portance, masse ajoutée et gradient de pression. Les résultats préliminaires obtenus correspondent à des conditions qui prévalent pour des inclusions dans les poches d'acier liquide. Ces travaux doivent cependant être poursuivis pour fournir des données quantitatives fiables.

Références :

[1] R. D. Moser, J. Kim, and N. N. Mansour. Direct numerical simulation of turbulent channel flow up to $\mathrm{Re}_\tau = 590$. Physics of fluids, 11(4):943–945, 1999.

[2] A. Soldati and C. Marchioli. Physics and modelling of turbulent particle deposition and entrainment: Review of a systematic study. International Journal of Multiphase Flow, 35(9):827–839, 2009.

[3] C. Narayanan, D. Lakehal, L. Botto, and A. Soldati. Mechanisms of particle deposition in a fully developed turbulent open channel flow. Physics of Fluids, 15(3):763–775, 2003.

Chapter 1 : Introduction

Contents

This thesis work has been supported and funded by the Labex DAMAS (LABoratory of EXcellence Design of Alloy Metals for low-mAss Structures) in the work Package WP3 called Process Design. The control of metal cleanliness represents a major challenge for alloy producers, because it affects product quality. Lowering the weight of finished parts, continuously improving the mechanical properties and increasing the recycling of used metal, make the metal cleanliness an unavoidable issue. Since the removal of inclusions in secondary steel making is an important concern, this research work focusses on the capture of the inclusions by turbulent deposition.

1.1 Steel treatment in ladle

1.1.1 Importance of steel cleanliness

Whatever the economic ups and downs and contrary to popular belief the world market of metallic materials keeps growing since the beginning of the 21st century. This is particularly the case of the steel industry with a doubling of the world production from 2000 to 2017, the crude steel production reaching 1.7 Bt in 2017 [3]. Another common belief concerns the position of the EU. The EU is the second largest producer of steel in the world after China. Its output is over 160 Mt of steel per year, with 500 production sites and with 1.8 million direct and indirect jobs [4]. With the aim of maintaining its competitiveness and its position, EU faces many challenges of which the cleanliness of steels since the need and value of cleaner steels has been increasing for the last decades.

The scope of the definition of Clean Steel generally relates to steels with a low concentration of solute elements (mainly oxygen, phosphorus, sulfur, nitrogen, hydrogen) and of non-metallic inclusions (NMI). The definition associates also controlled levels of the residual elements such as copper, lead, zinc, nickel, since concentration above a certain level might lead to a drop of steel properties. But the required purity levels vary with the steel grade and its end use, and finally the cleanliness standard desired by the customer is continuously changing (improving) as a function of time and technological improvements. The steel cleanliness is nowadays an important challenge for the competitiveness between the steelmaking companies and more precisely for the steel producers in Europe. The concentration of dissolved elements can have significant effects on the properties of final steel products. Hence these impurities form inter-granular segregations during solidification and thermal treatment processes which result in formation of precipitates and potential cracks. In amounts exceeding 100 ppm Sulfur and phosphorous tend to cause brittleness. The level of dissolved oxygen in liquid steel must be lowered because oxygen reacts with carbon during solidification and forms carbon monoxide and fatal blow holes in the cast.

With the aim of reducing oxygen content, deoxidation process is performed leading to precipitation of oxide or/and sulfide inclusions. Hence prior to deoxidation oxygen levels can range from 200 to 800 ppm oxygen whereas the total oxygen content after inclusion removal falls down to a few tens of ppm. However NMI have great effect on steel properties such as strength, plasticity, toughness, fatigue and the control of the population of this second phase is a key to metal cleanliness. Zhang and Thomas [5] give a complete review

on the control of steel cleanliness and more recently ZHANG et al. [6] brings fundamentals concerning NMI. They demonstrate that most of NMI has a detrimental influence on the mechanical properties. Oxide and nitride inclusions are brittle and hard particles which will induce stress concentration during rolling and could turn into cracks during fatigue cycles. Furthermore the ductility of large sulfide inclusions can lead to form very long inclusions in the rolling process giving anisotropic properties of steel. These negative effects not only depend of the chemical nature of the inclusions but on the morphology, size and amount. Zhang and Thomas [5] report that sometimes a catastrophic defect is due to a single large inclusion in a whole steel heat. Clean steel depends upon not only the control of the inclusion content and type but also upon the elimination of inclusions larger than the critical size harmful to the product (20 µm for tire cord or wire applications for instance).

Industrially a refining treatment has always been applied before casting, one of its purposes being the control of the metal cleanliness and more specifically the inclusion cleanliness. After the metal solidifies the characteristics of inclusions can be determined by either destructive or non-destructive methods, but the inclusion cleanliness can hardly be achieved by the mechanical or thermal treatments of the metal in solid state [7]. In other words when the metal is solidified it is too late to modify chemistry and inclusion cleanliness.

1.1.2 Control of inclusions in the ladle furnace

The ladle furnace (LF) is a key process to achieve metal cleanliness. The most common ladle treatment steps include deoxidation of the steel, optionally desulfurization of the steel, alloying the steel, adjusting the steel temperature for shipment to the tundish and continuous casting process, possibly inclusion modification, and inclusion removal, as shown in Figure 1.1.

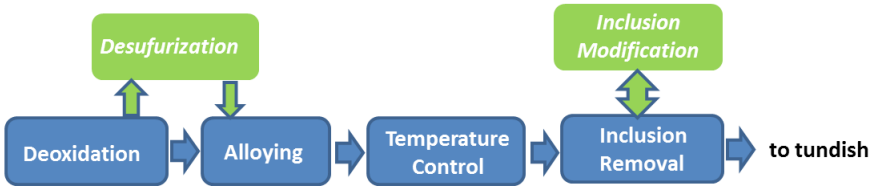

Figure 1.1 – Main steps in the ladle furnace

The type of deoxidation differs from one steel product to another and plays of course an important role in the type of the inclusions. When deoxidant is added to the liquid steel, the dissolved oxygen in the steel reacts with the deoxidant addition to form an oxide, following the chemical reaction:

$$xM + yO = M_xO_y\,(inclusion) \tag{1.1}$$

For most of the structural steel products, the steel is deoxidized with silicon and manganese ($Mn - Si$ killed). For sheet, plate and special bar, the steel is deoxidized with aluminum (Al killed). Some aluminum killed steels are also treated with calcium to modify the alumina inclusions and sulfur containing inclusions to improve castability and mechan-

ical properties of the product [8]. Depending of the chemical nature of the NMI and of the operating temperature, the inclusions can be fully solid, fully liquid or a mixture of solid and liquid.

Figure 1.2 shows the schematic diagram of a gas stirred ladle where the steel in liquid state is treated before continuous casting. The ladle is positioned into a sealed vessel making possible a vacuum degassing treatment (a residual pressure of 1 mbar can be maintained by the pumping device located at the side). An injection of argon through one or more porous plugs usually located at the bottom of the ladle provides both mixing of the liquid metal to achieve thermal and chemical homogeneity and the entrapment of the inclusions by the bubbles known as the flotation mechanism. At the top of the steel bath a molten slag layer covers the liquid making a protection against a possible reoxidation by the gaseous atmosphere. The industrial vessel typically contains 100 t of liquid steel and the argon gas which is fed through the bottom has a blowing rate between 50 Nliter/min to 200 Nliter/min, these values denote the low and high rates of stirring. As it can be seen in Figure 1.2, calcium may be added using a cored wire technology [8].

1.1.3 Origins of inclusions and properties

All the NMI formed during the steel treatment consists of different compounds whose properties are very much different than the parent steel alloy. Zhang and Thomas [5] identified 4 different sources of NMI:

1. Deoxidation products formed due to the chemical reaction between introduced deoxidants and dissolved oxygen. This is much the most important source of NMI. For example in a low carbon aluminum killed steel, the alumina (Al_2O_3) inclusions form the majority of the inclusion population.

2. Slag entrainment, which mainly occurs during high gas stirring or during transfer of liquid steel to tundish.

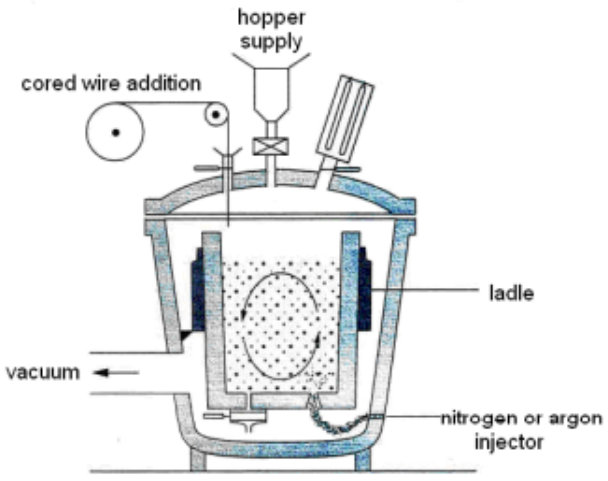

Figure 1.2 – Schematics of a ladle refining facility with degassing [7]

3. Steel reoxidation products, which usually occurs when the gas stirring is above a critical value; the slag layer is then broken leading to a slag open eye [9].

4. Big and irregular exogenous inclusions from wear of ceramic lining and of refractory walls.

Because most of the inclusions are the product of the deoxidation process we focus our attention to the modification of these inclusions following three stages:

1. **Nucleation:** In this stage nuclei of new phase is formed because of the supersaturation of the liquid steel with deoxidant additive and O and/or because of bath cooling. Nucleation of oxides can occur by homogeneous nucleation, particularly when the level of supersaturation of the dissolved additive and oxygen is high, or more often it can occur by heterogeneous nucleation on small inclusions formed earlier during the steel making process.

2. **Growth:** Growth of inclusions carries on (by mass transfer from liquid to solid) until the supersaturation cease to exist i.e. until the chemical equilibrium is reached. Because the inclusion growth is a relatively slow process a certain amount of non-equilibrium supersaturation might prevail. Dendritic morphology of alumina inclusion in a high oxygen environment is shown as an example in Figure 1.3(a).

3. **Agglomeration:** Collisions between solid or liquid primary inclusions can occur by Brownian motion (for particle size lower than 0.1 µm), turbulent motion or differential Stokes velocity. Because the wettability of the NMI is very weak in the liquid steel, most of the collision lead to aggregation and then to restructuring and agglomeration. Indeed Guthrie [10] have estimated contact angle for most of the solid inclusion (alumina, spinel, lime, silica ...) in liquid steel with values comprised between 110° and 145°. For solid primary inclusions the agglomeration process forms large aggregates. For liquid inclusions coalescence mechanism occurs leading to globular larger particles as seen in Figure 1.3(b) for the very classic calcium-aluminate inclusion. These successive mechanisms and events have been emphasized using confocal scanning laser microscope [11].

In typical low carbon aluminum-killed steel, 1 kg of metal contains 10^7 to 10^9 inclusions [5] with a log-normal particle size distribution as shown in Figure 1.4. Although this huge density number of inclusions the mass fraction remains very small around 10^{-5} i.e. 10 ppm of total NMI in the liquid steel. As we can notice in Figure 1.4 typical inclusion size in a ladle is between 1 to 20 µm and only very few inclusion have a size larger than 100 µm. Furthermore, Figure 1.4 outlines the efficiency of the ladle process to remove large size inclusions since the particle size distribution in the tundish (before casting) reveals a drop of the number of large inclusions. However the important increase of small size inclusions in tundish can be readily explained by precipitation of inclusions (in particular sulfide inclusions) due to the temperature decrease. As a consequence of this opposite trend the total mass content of NMI is roughly conserved (23 ppm in that example).

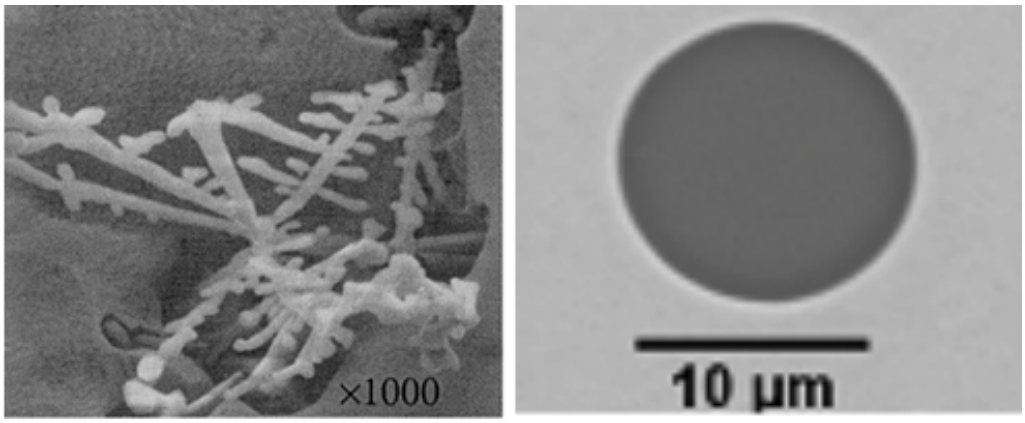

Figure 1.3 – (a) dendritic inclusion of alumina and (b) $Ca-Mg$ aluminate inclusions found in an Al-killed steel treated with Ca (adapted from [5] and [12])

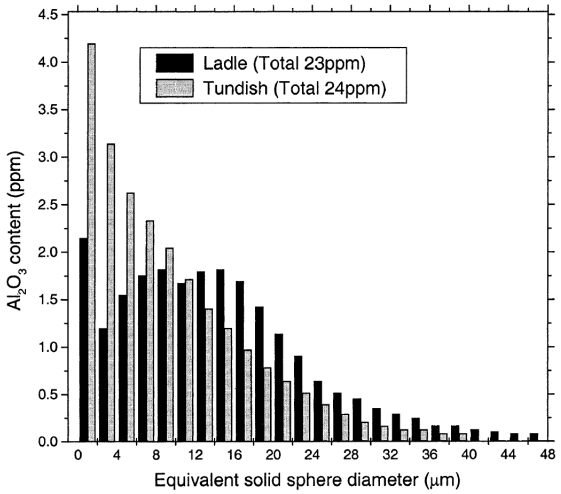

Figure 1.4 – Size distribution of alumina inclusions in ladle and tundish [5]

1.1.4 Inclusion removal in the ladle furnace

Removal of inclusions from molten steel is one of the major objectives in the secondary steel making, especially in the gas stirred ladle. As explained in section 1.1.2, the argon injection at the bottom of the ladle provides both turbulent mixing of the liquid bath and the entrapment of the inclusions by the bubbles known as the flotation mechanism. This turbulence flow is the driving force for particle collision and aggregation whereas physical separation mainly depends on the particle size. This is why aggregation has to be promoted at first, so that bigger aggregates become easier to separate.

The physical separation can be divided into three mechanisms as shown on the schematic of Figure 1.5:

- The collision and attachment of inclusion to the bubble surface. The attached inclusion is then transported by the bubble rising to the slag interface where the inclusion is finally released and trapped.

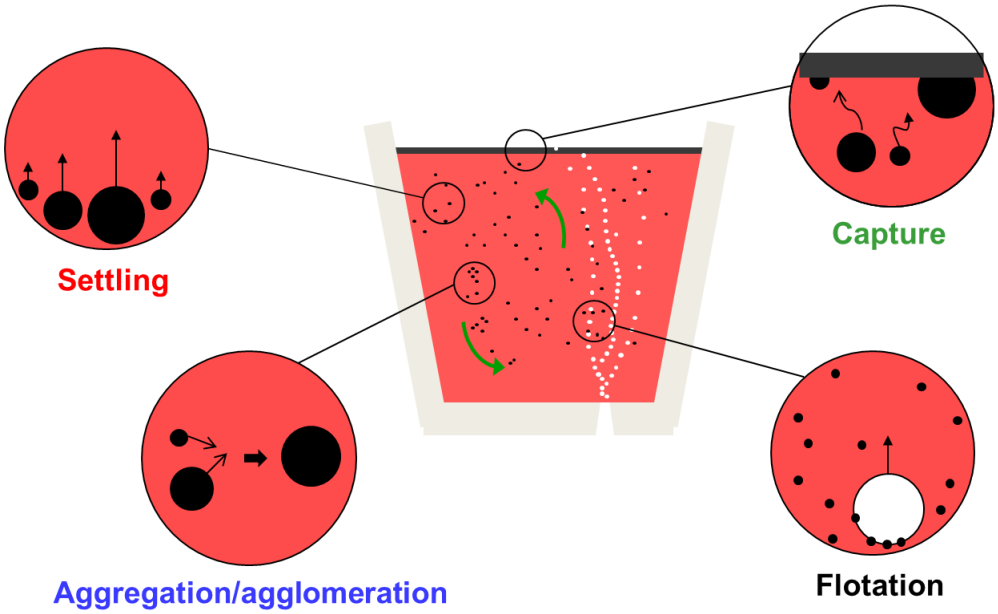

Figure 1.5 – Schematic of the inclusion behavior in the ladle furnace

- Because of the lower density of NMI compared to steel (roughly the half of the value) the inclusions tend to float to the surface of the steel bath.

- The turbulent flow promotes the entrapment of the inclusions at the surface of the refractory walls or of the slag layer. This thesis work addresses this issue.

CFD simulations of industrial gas stirred ladle allows for more insightful analysis of the turbulent flows as the example proposed by Bellot et al. [13] and reported in Figure 1.6. In these simulations, a RANS approach is applied within a standard $k-\epsilon$ turbulent model for the liquid steel phase. This simulation is applied to an industrial 60 t steel ladle with a relatively high stirring intensity corresponding to 63 Nl/min of argon for each of the two plugs. The liquid steel velocity and argon plume region on a plane passing through the porous plugs of the ladle are shown in Figure 1.6(a). We can observe the shapes of the two bubble plumes rising from the two porous plugs (the isosurface of gas volume fraction equal to 1% is drawn). The turbulence, mainly prevailing in these regions, is characterized by a turbulent shear rate in the range $30-500$ s^{-1} but can reach value around 1000 s^{-1} for very high stirring rate. The liquid metal flow is associated with two recirculation zones in each half of the plane of symmetry.

The molten steel is sucked by the bubbles rising from the porous plug to the slag layer which transports the inclusions toward the surface. In the bubble plume the aggregation and the attachment of inclusions to the bubbles are enhanced by the relatively high turbulence conditions.

Two examples of RMS of the fluctuating velocity are drawn in Figure 1.7. In this RANS simulation, in order to reduce the computing time, a wall function was applied as a boundary condition at the wall surface (y^+ is equal to 20 at the first cell node). Turbulence intensity

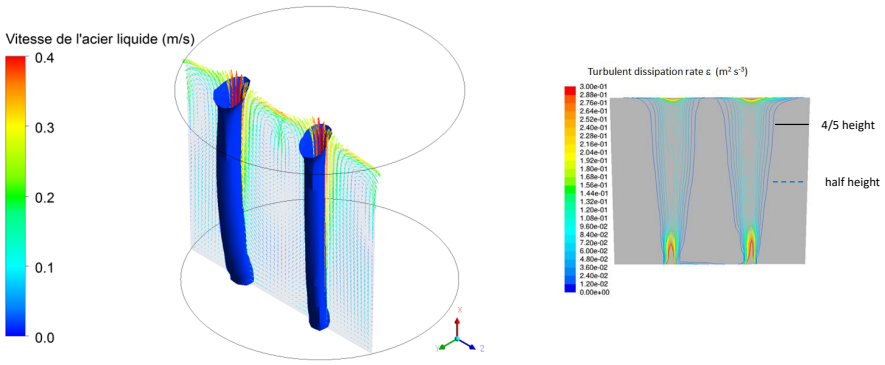

Figure 1.6 – Predicted turbulent flow by CFD (a): velocity of the liquid steel along with the argon plumes (isosurface of the 1% gas volume fraction) (b): Dissipation of the turbulent kinetic energy ϵ (m^2 s^{-3})

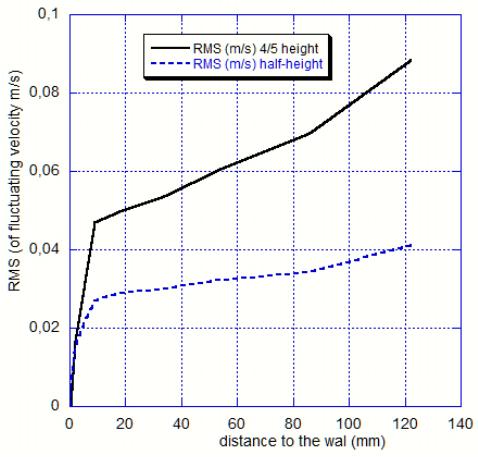

Figure 1.7 – Calculated RMS of the fluctuation velocity versus the distance to the wall [13].

increases strongly close to the wall in the boundary layer. The production of turbulence in the plume region leads to a continuous increase of the turbulence kinetic energy, which is more noticeable for the profile near the bath surface (in continuous black line) where the plume is widely developed rather than at half-height of the ladle (doted blue line). Otherwise the calculated shear stress $\mathbf{T}_w$ is respectively 0.5 and 0.4 Pa near the surface and at half-height.

Nearby the surface, as shown schematically in Figure 1.8, the inclusions are dragged along the surface of the slag layer and then along the ladle wall. During this transport in the turbulent boundary layer, deposition and capture of the non-metallic-inclusions may occur because of the low wetting of the particles by the liquid steel and of their high physico-chemical affinity with the slag and refractory walls.

Finally deoxidation of the steel bath is achieved thanks to the removal of NMI and is usually represented by a first order linear ODE, given in Equation 1.2:

$$\frac{dC_O}{dt} = -K_O C_O \tag{1.2}$$

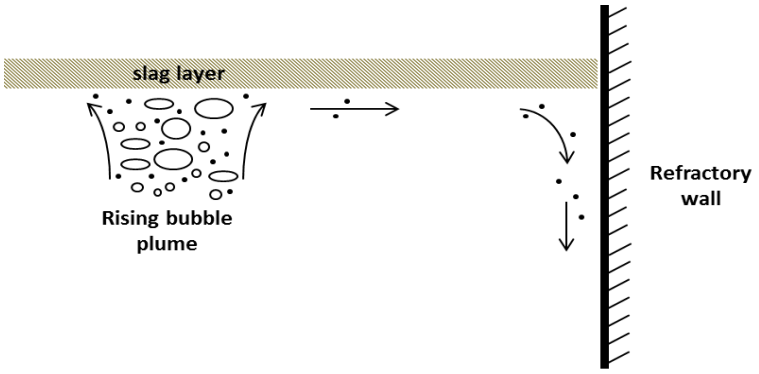

Figure 1.8 – Schematic of the inclusion behavior in the bubble plume and near the slag and wall surface.

where C_O represents the total oxygen content and K_O is a kinetic constant (min^{-1}).

Figure 1.9 compares this kinetic constant K_O obtained by the numerical coupling between CFD and population balance method (PBM) with industrial data reported by Zhang and Thomas [5].

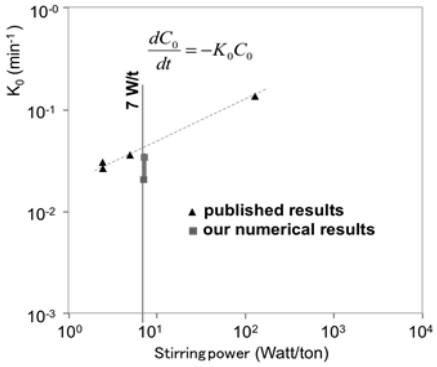

Figure 1.9 – Effect of stirring power on deoxidation rate according to Zhang and Thomas [5] and Bellot et al. [14]

1.2 Deposition of aerosols and hydrosols

Deposition of particles on solid walls have been largely studied for aerosols [15–18] but the literature for hydrosols is much poorer [19]. These two systems differentiate from each other based on the particle to fluid density ratio. Aerosols generally have large density ratio, about 10^3 while hydrosols has a ratio in the order of unity. Aerosols are tiny solid or liquid particles suspended in gas which are produced by volcanic eruptions, forest fires, fossil energy combustion etc. While hydrosol type particles can be observed, among other processes, in water treatment processes and in metallurgical processes such as solid inclusions in liquid metals.

1.2.1 Aerosol deposition

Following many authors [15, 20–22], we can identify different driving mechanisms leading to transport and collection of aerosol particles on solid wall which are mainly: (1) settling, (2) inertial impaction or inertial deposition, (3) direct interception, (4) diffusional deposition, (5) electrostatic deposition, (6) thermal deposition. Settling (1) usually indicates the prominent role played by the gravitational force. The concept of inertial impaction (2) lies on the fact that the heavier particles collide with the wall due to inertia whereas the smaller inertial particles follow the gas stream. In direct interception mechanism (3), the particle trajectory following the gas stream lines is closed to within the radius of the particle from the wall. In diffusional deposition (4), smaller sized particles ($d_p < 0.3$ µm) experience random molecular or Brownian motion thus leading to collection. All these four mechanisms apply to particle deposition in turbulent flow [17] as we will see later and are illustrated in Figure 1.10. Electrostatic deposition (5) deals with the mutual attraction between the particles possessing one kind of charge and the deposition wall with an opposite polarity. Thermophoresis (6) is a crossed diffusion mechanism i.e. a steep temperature gradient leads to mass diffusion so-called Soret effect. Since the thermophoretic diffusion coefficient is often very small, only a very steep temperature gradient near the wall gives rise to perceptible effect [23]. Mehel et al. [24] studied a combined effect of both thermophoresis and turbulent phenomena. They found that turbulent dispersion and thermophoresis mechanism prevail for particle size range, ($\tau_p{}^+ < 2$) and for a particular temperature gradient, these two mechanisms leading to wall deposition can be considered as correlated for nanoparticles.

As seen from most of experiments and numerical studies, deposition is quantified by the so-called deposition velocity expressed as a function of the particulate Stokes number. The deposition velocity u_d (m s^{-1}) is defined as the ratio between the flux density of particles $(\varphi_p)_{wall}$ (m^{-2}s^{-1}) that are deposited on the wall to the mean or bulk concentration of particles in the fluid flow $\bar{C_p}$ (m^{-3}).

$$u_d = \frac{(\varphi_p)_{wall}}{\bar{C_p}} \tag{1.3}$$

The particulate Stokes number (τ_p) denotes the inertia of the particle and gives the time

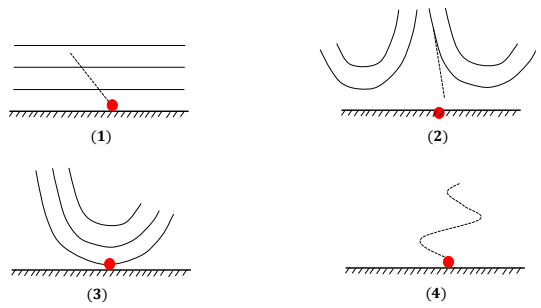

Figure 1.10 – Mechanisms involved in deposition of aerosols by (1) sedimentation, (2) inertial impaction, (3) interception and (4) Brownian diffusion

scale at which terminal slip velocity between the fluid and particles is reached. This Stokes number depends on the square of the radius of the particle. For aerosols the relaxation is given by :

$$\tau_p \;=\; \frac{d_p^2 \rho_p}{18 \rho_f \nu_f} \tag{1.4}$$

where ρ_p and ρ_f are the particle and fluid density and ν_f denotes the fluid kinematic viscosity.

Deposition velocity and particulate Stokes number are made dimensionless by using the friction velocity ($u_{\mathbf{T}}$) (also known as the shear-stress velocity) and obtained as :

$$u_{\mathbf{T}} \;=\; \sqrt{\frac{\mathbf{T}_w}{\rho_f}} \tag{1.5}$$

where $\mathbf{T}_w$ is the wall shear stress. Then, we have : ${u_d}^+ \;=\; u_d/u_{\mathbf{T}}$ and ${\tau_p}^+ \;=\; \tau_p u_{\mathbf{T}}^2/\nu_f$. Hence correlations and deposition curves are built with these two dimensionless variables.

Experimental investigation

Many authors (Friedlander and Johnstone [25], Liu and Agarwal [26], Wells and Chamberlain [20]) had performed experimental studies and measured the deposition velocity for aerosols where three deposition regimes were identified with respect to dimensionless particulate Stokes number (τ_p^+). When the particles are small mainly in the sub micrometer range where $\tau_p^+ < 0.2$ the deposition velocity (u_d^+) decreases as (τ_p^+) increases as shown in the Figure 1.11.This regime corresponds to the Brownian regime where particles are transported by Brownian diffusion. The expression for deposition velocity is given by Wells and Chamberlain [20]:

$$\frac{u_d}{u_{\mathbf{T}}} = 0.2\, \mathbf{Sc}^{-2/3} \mathbf{Re}^{-1/8} \tag{1.6}$$

where $\mathbf{Sc}$ is the Schmidt number defined as a ratio between kinematic viscosity of the fluid phase to the Brownian diffusion of particles.

Wood [27] carried out analytical studies for aerosol which have been considered as a reference work in this field. Three deposition regimes were identified with respect to dimensionless particulate Stokes number (τ_p^+) as shown in Figure 1.11.

Hence moving on to larger particle sizes ($d_p > 1$ µm) where $0.2 \leq \tau_p^+ \leq 20$, inertial effects arise and there is a significant increase of deposition velocity. This regime is called the turbulent dispersion regime where a correlation is proposed by Wood [27]:

$$\frac{u_d}{u_{\mathbf{T}}} = 4.5\; 10^{-4}\; {\tau_p}^{+2} \tag{1.7}$$

For $\tau_p^+ \geq 20$ the deposition velocity remains nearly constant. The regime is called the inertia moderated regime where the value of the deposition velocity obtained by Wood [27] is :

$$\frac{u_d}{u_{\mathbf{T}}} \;=\; 0.13 \tag{1.8}$$

Based on the earliest experiments, a deposition model was proposed by Friedlander and Johnstone [25] which was called free-flight theory where particles are transported by

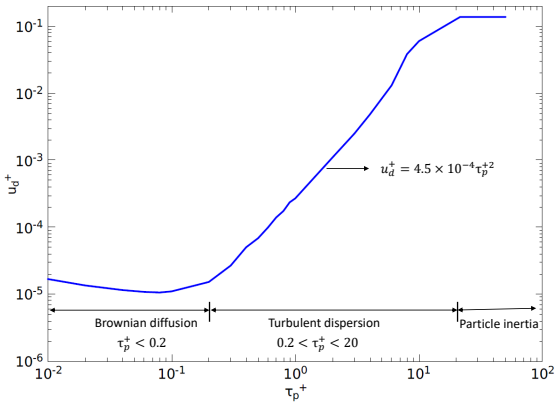

Figure 1.11 – Plot showing different deposition regimes when compared to dimensionless particulate Stokes number (τ_p^+)[27].

the turbulent eddies. These particles come close to the wall within one stop distance and have enough inertia to travel through the viscous sublayer and finally deposit. Rashidi et al. [28] performed experiments where particles were introduced in an open turbulent channel flow and the significance of sweep and ejection phenomena in the deposition and re entrainment of particles was observed. They highlighted the accumulation of particles close to the wall and also noticed that particles with radii less than 0.5 wall units, when arriving close to the wall without depositing, are barely lifted up by near wall ejection. Rashidi et al. [28] explained these phenomena with the schematic Figure 1.12(a), drawing low speed streaks created between pairs of longitudinal counter rotating vortices. Since the particles are introduced in the flow, these low-speed streaks lead to the accumulation of particles. Depending on the particle inertia, few are lifted up with the help of the inclined vortex-loops present in the near wall region and are finally ejected out in the bulk flow. If the particle density is much greater than the fluid, they come back to the near wall region. This process of bursting gets repeated thus leading to the transport of particles in the flow direction. Cleaver and Yates [29] introduced the principle of down-sweep flow as shown in Figure 1.12(b). When a particle is entrapped in the down-sweep it will continue following the down-sweep with small interruption. The particles present between the turbulent bursts as shown in Figure 1.12(b) will have the chance to be captured by the wall and others in the influence of the bursts will be swept away from the wall in the outer regions.

Numerical simulation

Basically two numerical methods are involved in simulation of particle deposition (i) Eulerian and (ii) Lagrangian. The Eulerian simulation is usually devoted to the calculation of the continuous turbulent gas flow applying either Large Eddy Simulation (LES) or more often Direct Numerical Simulation (DNS) techniques, whereas Lagrangian Particle Tracking (LPT) is used to calculate trajectories of a large number of particles with a one way coupling. Statistical analysis is then performed to produce RMS of fluctuating velocities (gas and particles) and mean deposition rate. The one way coupling assumes that the discrete phase do not modify locally or globally the turbulent flow. In the DNS simulation,

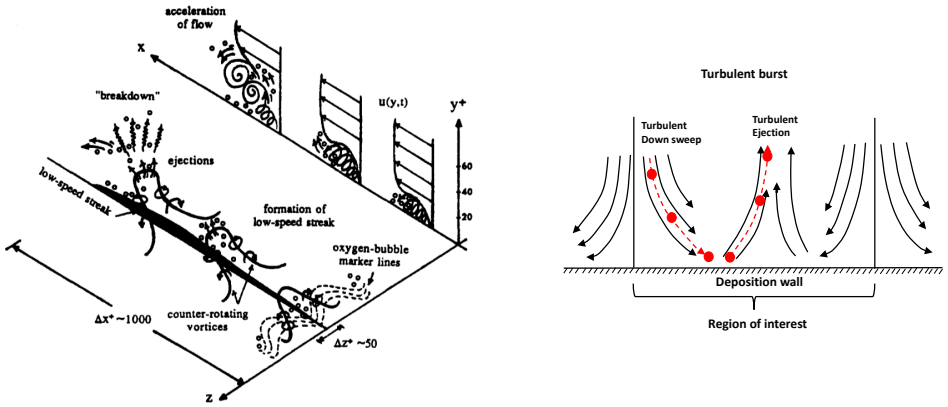

Figure 1.12 – Plot of (a) Particle transport phenomenon close to the wall (Rashidi et al. [28]) and (b) Idealised flow including the sublayer (main flow is normal to the figure) (in accordance with Cleaver and Yates [29])

particle size is supposed to be smaller than the Kolmogorov length scale ($d_p < \eta$) and dilute condition is considered as well.

In the literature for particle deposition in a fully developed wall turbulent flow, authors [30–32] used Direct Numerical Simulation (DNS) where pseudo spectral technique is used to solve the Navier-Stokes equation. Yao et al. [33] used Large Eddy Simulation (LES) with dynamic Smagorinsky model while Soldati and Marchioli [34] used both DNS and complementary LES method to solve the Navier-Stokes equation.

McLaughlin [30] performed a DNS simulation of a fully developed channel flow with Lagrangian particle tracking where he illustrated that the particles tend to collect in the viscous sublayer region. However the simulation cost in the $80s$ were so high that the simulation time interval was too short to guarantee reliable results. Brooke et al. [31] worked with the idea of free flight mechanism of Friedlander and Johnstone [25] where DNS was performed in a channel flow to study the deposition. They evaluated the probability density function of the wall normal particle velocities near to the wall and found that only a small fraction of particles experience free flight mechanism and finally deposit, thus resulting in significant accumulation of particles close to the wall. Later on in a next work, Brooke et al. [22] divided the particle flux into three contributions : (a) flux by free-flight, (b) diffusive flux and (c) turbophoretic flux. Reeks [21] defined diffusive flux as the particle flux because of the gradients in particle concentration and turbophoretic flux as the particle flux due to the turbulent intensity gradients. Guha [17] had observed that in the turbulent boundary layer, flux of very small particles can be evaluated by integrating Fick's law of diffusion,

$$J = -(D_B + D_T)\, dC_p/dz \tag{1.9}$$

Here D_B is the Brownian diffusivity, D_T is the turbulent diffusivity and this parameter varies with position, dC_p/dz is the particle density gradient.

Turbophoresis is the process in which particles move from regions of higher turbulence to lower ones. If there is a sudden decrease in turbulence intensity, the particles are unembedded from the turbulent eddies and execute free flight transport. Particles can later on

abandon free flight and again become entrained in the turbulent eddies. Brooke et al. [22] with the computing performance available in the $90s$, try to analyze the respective contribution of free flight and diffusion mechanisms on the deposition. They noted that when particles appear very near the wall the deposition distance becomes very small along with the chance of having large enough momentum to carry the particles to deposit. Thus the final conclusion made by Brooke et al. [22] was that these trapped particles, which, eventually manage to deposit, need to move away from the wall into a region with high enough velocity fluctuations to bring the particles back to the wall.

Since the early $2000's$, Soldati and co-workers provided a significant work on DNS simulation of point particle deposition. They investigated the strong coherent sweep and ejection events responsible for particle transport (see Figure 1.13). They also reveal the effect of the small streamwise vortices thus leading to particle accumulation close to the wall where low-speed streaks are formed. Hence Figure 1.14 gives the variation of particle concentration along the wall normal direction when the statistically stationary state is reached and for two different inertial aerosols (${\tau_p}^+ = 5\ and\ 15$). The authors [35] clearly emphasized the high accumulation of particles very close to the wall. They also highlighted the preferential locations where particles tend to deposit. Particle deposition patterns calculated by Narayanan et al. [35] (see Figure 1.15) reflect the particle accumulation in the streamwise oriented streaks.

Complementary to this work, Soldati and Marchioli [34] provided in 2009 a deep numerical investigation of particle deposition in a wall turbulence channel flow. A pictorial view of particle behavior is given in Figure 1.16 where a snapshot of particle locations and flow field are represented in a cross-sectional window ($y - z$ plane, x is the streamwise direction).

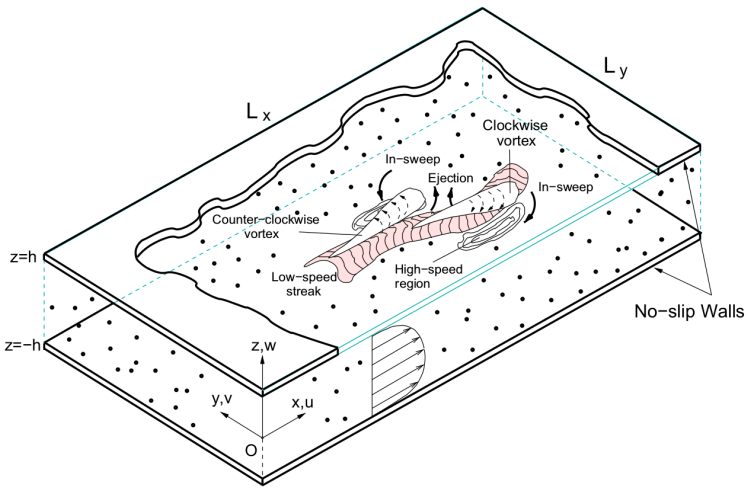

Figure 1.13 – Particle-laden turbulent gas flow in a channel: schematics of the simulation domain and near-wall turbulent coherent structures. Strong causal relationship links low-speed streaks to ejections generated by quasi-streamwise vortices, which also generate in-sweeps of high streamwise momentum fluid to the wall in the high velocity regions. (Soldati and Marchioli [34])

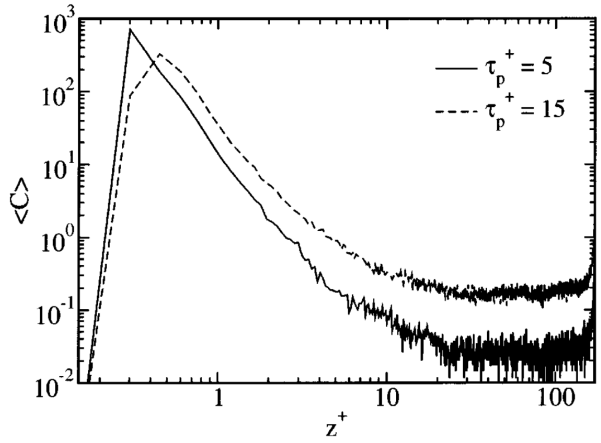

Figure 1.14 – Average concentration profile along the wall normal direction. (Narayanan et al. [35])

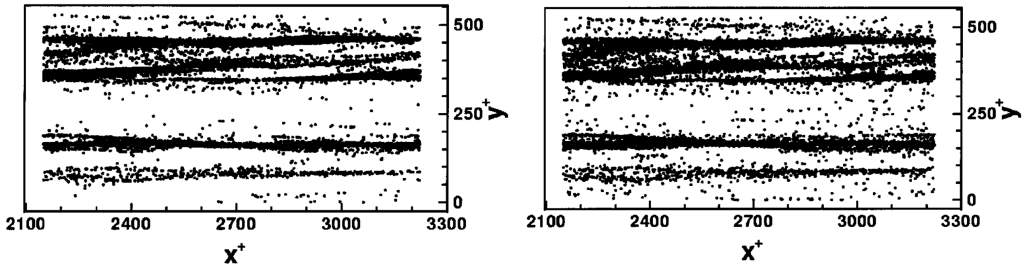

Figure 1.15 – Accumulation of particles pattern for (a) $\tau_p{}^+ = 5$ and (b) $\tau_p{}^+ = 15$ (Narayanan et al. [35]), x is the streamwise direction.

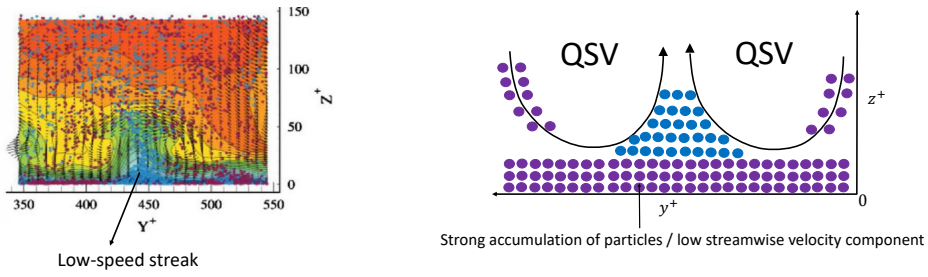

Figure 1.16 – Cross section and front view of particle location and streamwise velocity (a) color isocontour of the streamwise velocity component (Soldati and Marchioli [34]), (b) schematic interpretation of figure (a)

Blue particles have wall-normal velocity directed away from the wall while purple particles move towards the wall. We clearly observe from the simulation that maximum accumulation of particles occurs between the two counter-clockwise and clockwise Quasi Streamwise Vortices (QSV) at low z^+ ($z^+ < 5$), corresponding to a low-speed streak.

Soldati and Marchioli [34] proposed then a detailed view of the particle transfer mechanism (Figure 1.17). Segregation of packages of particles is the first stage of deposition where the in-sweep flow bring particles towards the wall. This causes an increase in con-

centration and accumulation of particles close to the wall especially between QSV. Turbophoresis is the main reason behind the drift of particles towards the accumulation region, which is located into the viscous sublayer. Particles in this accumulation region may either deposit at the wall or ejected by out-sweep flow.

Yao et al. [33] combined Large Eddy Simulation with Lagrangian Particle Tracking using one way coupling in a square duct and found that preferential deposition of particles occurs by the secondary flow pattern which typically exists in the square ducts. Particle deposition along the streamwise direction was mostly dominated by the drag force. However the lift force has an effect nearby the wall only when the particles are larger i.e. $d_p > 500$ µm. Pirozzoli et al. [36] stated that at high friction Reynolds numbers ($Re_{\mathbf{T}} \geq 500$), there is a strong accumulation of particles close to the wall, when the range of particulate Stokes number is ${\tau_p}^+ = 10 - 100$. The deposition rate for a given Stokes number increases with friction Reynolds number ($Re_{\mathbf{T}}$). The authors here show that the streaks are responsible for particle segregation in the near wall region, significantly affected by turbophoresis, as already described by Soldati and Marchioli [34]. Very recently Lu and Zhang [37] studied particle deposition behavior in an air flow duct using Reynolds stress model with discrete particle model. They found that the deposition velocity increases with the increase in particle diameters and bulk air flow.

Otherwise Fan and Ahmadi [38] in the 90s built a much simpler analytical sublayer model to study aerosol turbulent deposition based on the approach of Cleaver and Yates [29]. They studied the motion and deposition of aerosol particles in the near-wall stationary coherent structures which means the authors assumed that the streamwise vortex has a longer duration time than the characteristic turnaround and particle transport times. Figure 1.18(a) represents the fluid velocity vectors in the cross stream plane where the arrangement of flow includes two streamwise vortices rotating in opposite directions. At the centerline i.e. $y^+ = 0$, the sweep structures are located while at the two ends i.e. $y^+ = -50, 50$, ejection events exist. Figure 1.18(b) represents the schematic model of the deposition model along with the rough wall surface proposed by Fan and Ahmadi [38]. The symbol h here de-

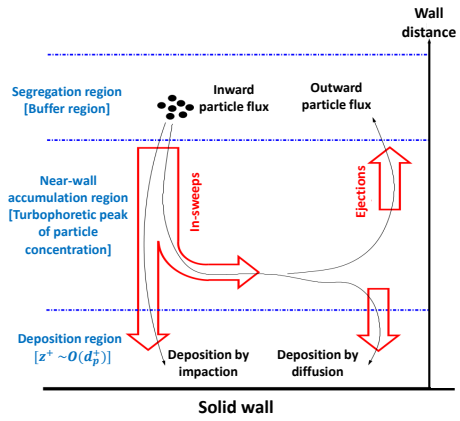

Figure 1.17 – Near-wall driving mechanisms, responsible for particle concentration buildup in the near-wall accumulation region(Soldati and Marchioli [34]).

notes the height of roughness and σ_h denotes the standard deviation of roughness. In their work, they assumed that when the particle reaches a distance of one standard deviation of roughness, the particle is assumed to be captured, i.e.:

$$z_c = h + \sigma_h - e + d_p/2 \tag{1.10}$$

Here z_c is the distance of capture. σ_h is estimated based on the roughness height h as given by Browne [39] $\sigma_h = 0.17k$. e represents the displacement in origin of velocity profile which according to Browne [39] for small roughness is given by $e = 0.53h$. The model of Fan and Ahmadi [38] is describe in the last part of aerosol deposition because of its use by Dupuy et al. [19] for hydrosol deposition in the next section 1.2.2.

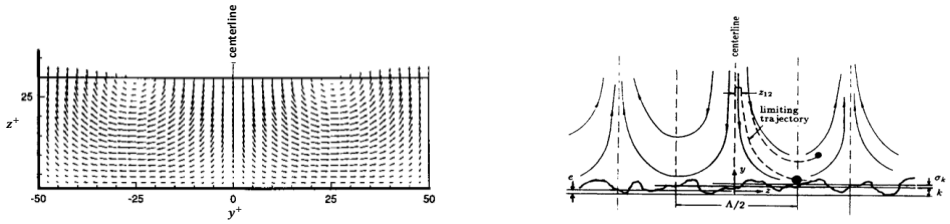

Figure 1.18 – (a)Plot of Velocity vector field describe by the sublayer model (Fan and Ahmadi [15]) and (b) Schematics of deposition model (Fan and Ahmadi [38])

1.2.2 Hydrosol deposition

Recently Dupuy et al. [19] used the approach of Fan and Ahmadi [15, 38] and used it to study the turbulent deposition of hydrosols. Hydrosol differentiate from aerosol based on the particle-fluid density ratio and also additional forces like added mass, pressure gradient and lift forces plays an important role. These forces henceforth cannot be considered as negligible compared to the particle inertia and the pseudo-steady drag. The true relaxation time of a hydrosol particle including added mass is given by the expression [40] :

$$\tau_p = \frac{d_p^2(\rho_p + 0.5\rho_f)}{18\mu_f} \tag{1.11}$$

When the particles travel close to the wall and the distance of separation between particles and wall is less than the order of particle diameter, the drag force applied on the particles diverges from Stokes law and due to the hydrodynamic interactions, also known as lubrication effects [19]. This effect may seriously alter the hydrosol deposition since the dynamic viscosity of gases are several magnitude lower than that of liquids. The final contact between such hydrosol particle and wall occurs due to physico-chemical interactions which consists of attractive Van der Waals and repulsive electrostatic double layer interactions respectively [19]. Dupuy et al. [19] proposed different deposition regimes to exist as a function of particulate Stokes number for a channel and pipe flows. For sub-micrometer range particles ($\tau_p{}^+ < 10^{-3}$), particles deposit by Brownian diffusion where inertial and

gravitational forces are negligible. The final conclusions emphasized by Dupuy et al. [19] are as follows (a) the effect of inertial forces on the deposition is negligible, (b) lift force can have a significant effect for $d_p{}^+ > 1$, (c) For non-buoyant particles, direct interception results in deposition and the deposition velocity relates to the particle diameter by the power of 1.7, (d) For buoyant particles sedimentation is the major criteria for deposition and the hydrodynamic interactions have a major effect on the deposition velocity.

1.3 Methodology followed in this study

The main goal of this thesis is to investigate turbulent deposition of inclusions on the wall and free slag surface of the ladle furnace. The study on deposition can be achieved by determining the capture mechanism of particles and model it through deposition velocity. The objectives can be fulfilled by following the procedures described below in the schematic Figure 1.19.

Figure 1.19 – Schematic showing the numerical methodology followed in the thesis

1st step: Since the deposition flux occurs in a wall bounded turbulence flow, the first aim is to set up Direct Numerical Simulation (DNS) of a turbulent liquid metal flow. The concept of linear isotropic forcing method is used which provides artificial homogeneous energy to the calculated flow. This forcing can be achieved by reaching statistically stationary turbulence.

2nd step: After accomplishing DNS of isotropic homogeneous turbulence, it is applied for flow simulation near the wall. Two regions are selected in which the top region is

used to generate turbulence while in the bottom region wall boundary layer or law of wall is studied. Vortices generated in the top region diffuse and are transported to the wall boundary region. Mean fluid flow is modeled thanks to a mean shear stress applied at the interface between the two regions.

3rd step: After attaining fully developed wall bounded turbulence, passive tracers acting as fluid parcels are introduced into the computational domain. This step is performed to check whether the tracers flow along the streamlines of the fluid flow and also to study the mean tracer concentration throughout the domain.

4th step: Finally inertial point particles are introduced to depict the deposition velocity at the wall. Our study is focused on aerosol particle deposition with the aim of comparing numerical results with literature data. Finally a parametric study is done to observe the deposition velocity changes with the particle inertia. Transport and accumulation of aerosols are investigated using the concentration, velocity and force profiles.

1.3.1 Manuscript organization

This section is the final part of the Introduction where a descriptive outline is provided of the three main chapters of the thesis manuscript.

The second chapter deals with the creation of artificial isotropic homogeneous turbulence. This production of turbulence will be used to generate wall bounded turbulence in a limited computational time. First section provides a background on turbulent fluid flow where there are subsections characterizing turbulence, energy cascade, turbulence energy spectrum, isotropic homogeneous turbulence and ergodicity. These subsections describe about such topics more vividly before carrying on with other sections later in this chapter, thus giving a proper understanding on the aspects of turbulence phenomenon. In the following section of this second chapter Direct Numerical Simulation (DNS) by using the lattice Boltzmann Method (LBM) is described into details. The FLUA code recently developed at Institute Jean Lamour is the principal numerical tool adapted to perform the numerical simulation in this thesis. In the same section we investigate the linear isotropic forcing method which provides an extra force or energy to the Navier-Stokes equation thus generating artificial turbulence. Then we reveal the operating parameters for the simulations along with the scaling concept between the LBM units and physical units. Last section illustrates the final results obtained and thus validating the generation of isotropic artificial turbulence.

The third chapter uses the concept of generation of this turbulence and is applied to the wall boundary layer where wall bounded turbulence is studied. A particular attention is paid to the law of wall profile along with turbulent structures close to the wall. Comparison with literature data obtained by DNS of turbulence in a channel flow is also presented and discussed. This chapter is important to provide the required turbulent flow scenario to study particle deposition flux.

The aim of last chapter is to evaluate the turbulent deposition rate in case of aerosols. In this chapter, validation is provided thanks to the simulation of deposition of aerosols where the literature is particularly rich compared to hydrosols. A thorough investigation of

transport and accumulation of aerosol particles for different Stokes number near the wall is then presented. Finally as a question of time availability, the simulation of hydrosols in fluid conditions prevailing in liquid steel ladle is only initiated. Preliminary results have been reported for hydrosols.

Chapter 2 : Implementation of linear forcing in lattice-Boltzmann equation for generating isotropic homogeneous turbulence

Contents

After a description of turbulence and its underlying physics, the objective of this chapter is to show how lattice Boltzmann method (LBM) has been used to solve direct numerical simulation (DNS) of forced linear isotropic turbulence. It provides a description of the linear forcing method that has been used to generate homogeneous isotropic turbulence and its implementation in the LBM. After that, it presents the simulation parameters used to initiate the simulation and the conversion between LBM units to physical space. Finally, it shows the results that have been obtained along with proper validation and comparison with results from the literature.

2.1 Introduction to turbulence

The section starts with an historical overview of how turbulence was visualized and studied across several centuries. A proper definition of turbulence is given in section 2.1.2 based on Reynolds decomposition. Section 2.1.3 describes the cascade of energy and breaking of larger eddies into smaller ones and shows energy transfer from larger scales to smaller ones at which energy is dissipated. Then, the three hypothesis stated by Kolmogorov are presented in section 2.1.4. Section 2.1.5 details the linear forcing technique to generate artificial turbulence and how it was developed in the last few decades in physical and Fourier space. Then, the linear forcing method, that we use in physical space, is described in section 2.1.6.

2.1.1 Historical overview

Leonardo da Vinci, in the 14th century, is often considered to be the first one who observed turbulence as a physical phenomenon, but no quantitative or theoretical advances could be found until a mathematical formulation was given. The Navier-Stokes equations are a set of partial differential equations that describe the flow of incompressible fluids. They are a generalization of the equation devised by Swiss mathematician Leonhard Euler in the 18th century to describe the flow of incompressible and frictionless fluids. In 1821, French engineer Claude-Louis Navier introduced a term called viscosity (friction), which dealt with the more realistic and vastly more difficult problem of viscous fluids. Throughout the middle of the 19th century, British physicist and mathematician Sir George Gabriel Stokes improved on this work, though complete solutions were obtained only for the case of simple two-dimensional flows. The complex vortices and turbulence that occur in three-dimensional fluid flows as velocity increases, have proven intractable to any but approximate numerical analysis methods.

After that, it is not before the late 19th century that substantial progress was made on this matter, starting with Boussinesq [41]. He proposed a first modeling of turbulence in the form of an apparent viscosity, based on the assumption that the mean strain rates and the turbulent stresses can be related through a linear relation. This hypothesis still constitutes a basic foundation for many turbulent models. In 1894, Reynolds [42] experimentally studied turbulence and identified a single dimensionless parameter, known as the Reynolds number, to be the sole physical parameter to turbulence transition of an incompressible flow in a pipe. Reynolds also introduced the decomposition of a turbulent flow into a mean and a

fluctuating component (hence known as Reynolds decomposition). At the same period, Poincaré [43] was working on nonlinear dynamic systems from a mathematical perspective and demonstrated that chaotic behavior can arise from complex deterministic systems, due to their sensitive dependence on initial conditions.

In the 20th century, Lorenz [44], an American mathematician and meteorologist characterized turbulence as a nonlinear system exhibiting chaotic behavior. In the year 1925, Prandtl [45] introduced the "mixing length theory" that completes Boussinesq approach by giving an estimation of the apparent turbulent viscosity of momentum transfer by turbulence in a Newtonian incompressible flow, thus allowing a statistical approach to turbulence. Although this approach was not rich enough to provide turbulent flow predictions, it proved to apply quite well to some simple flow configurations. Then Taylor [46] developed mathematical statistical correlations to analyse turbulence, particularly through Fourier transforms and power spectra. He proposed statistical means to describe isotropic homogeneous turbulence [46] and to account for its chaotic nature. Performing experiments inside a wind tunnel, he showed that turbulent flows can be viewed as locally isotropic and homogeneous. Kolmogorov [47], a Russian statistician derived important results for the theory of turbulence. In 1941, he developed a theory (sometimes referred to as "K41"), which was based on the theory given by Richardson [48] that in a turbulent flow, there are vortices of all possible scales and energy is transferred from the larger vortices to smaller ones. The hypotheses proposed by Kolmogorov were widely used and accepted.

In the early 1960's, experimental procedures had greatly improved but the ultimate breakthrough that would drastically change the study of turbulence was the introduction of computing. Lorenz [44] was the first to publish research results using computers, which changed how turbulence was investigated. He developed a highly simplified weather model on the basis of the Rayleigh-Benard experiment. This model demonstrated that even only three ordinary nonlinear differential equations can cause aperiodic chaotic behavior and that thus, long-term weather forecasts are impossible on principle. At the same time, new experimental studies focused on more specific configurations such as isotropic homogeneous turbulence, wall boundary layers, turbulence transition in channel and pipe flows etc, while mathematical knowledge on Navier-Stokes equations improved. Ruelle and Takens [49] revealed that these equations have chaotic solutions due to sensitivity to initial conditions due to strange attractors. Their paper provided the transition chain that a flow will experience when it starts from a steady state and evolves towards a turbulent chaotic state through a periodic and a quasi-periodic link. This transition chain was later observed in many experiments during the 1970's and 1980's [50–53].

The 1970's and the 1980's see significant progress in computational capabilities and simulations start to be run on large supercomputers. Deardorff [54] was the first to perform Large Eddy Simulation (LES) which was later followed by the Direct Numerical Simulations (DNS) by Orszag and Patterson Jr [55]. Also Reynolds-averaged Navier-Stokes modeling approach was used firstly by Launder and Spalding [56]. Out of this numerical techniques, DNS was often not possible because of its requirement of high computational power which was lacking at that time. But in the 1990's and 2000's, computational efficiency improvements made DNS and LES suitable to simulate more and more turbulent

flows.

2.1.2 Generalities about turbulence

Turbulent flows are common in many engineering problems as well as in our day to day life. For example, small particles and droplets transported by smoke from chimneys or in clouds reveal structures in their carrying flow. Similarly, the interfaces in mutliphase flows such as water flowing out of a faucet and surfaces of rivers show many small scale patterns (see Figure 2.1) that illustrate the complexity of such turbulent flows.

Turbulence can be interpreted as a population of numerous eddies of different length and time scales. Such eddies can thus be defined by their characteristic diameter and their velocity. The combination of eddies of multiple scales is the cause of the apparently random velocity fluctuations arising from the chaotic nature of turbulence. Following Reynolds decomposition, the mean and fluctuating components of the instantaneous velocity (u_i) in a turbulent flow are usually considered separately. In terms of statistics, the mean velocity $(\bar{u})$ is defined as an ensemble average velocity, that is the velocity average over various realizations of the same experiment. However, it is usually calculated as a volume (for homogeneous turbulence) or time average (for statistically steady flows) by assuming ergodicity of turbulence. Consequently, the fluctuation velocity (u') is defined as the difference between instantaneous velocity and mean velocity, as shown in Figure 2.2, so that Reynolds

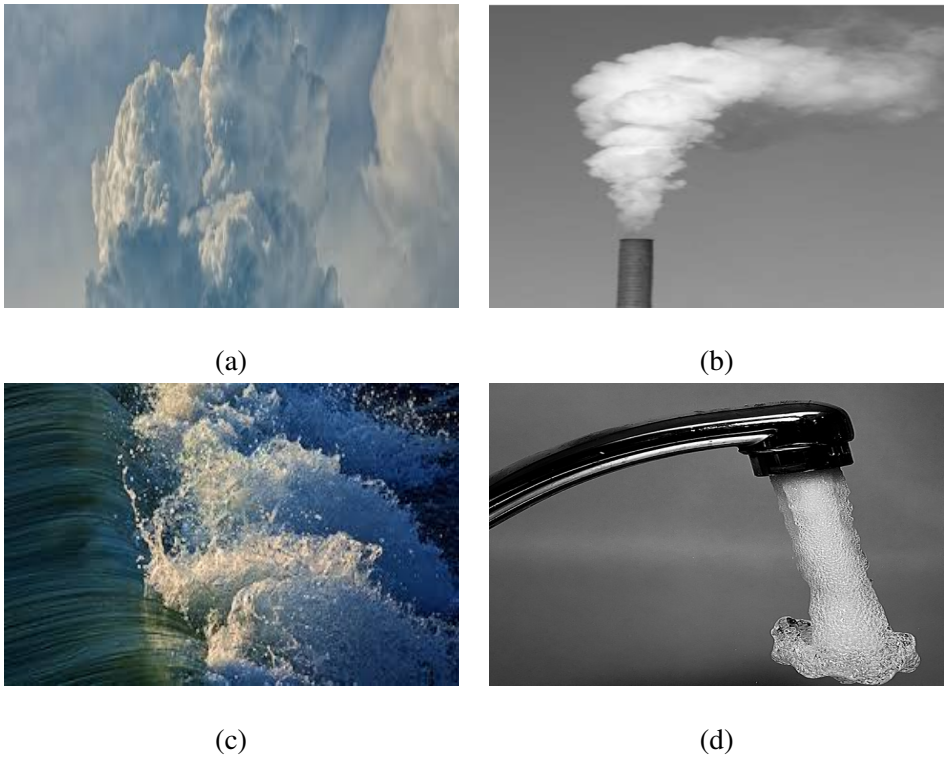

(a) (b)

(c) (d)

Figure 2.1 – Turbulence phenomenon observed in (a) river flow, (b) smoke from chimney, (c) clouds and (d) water flow from tap.

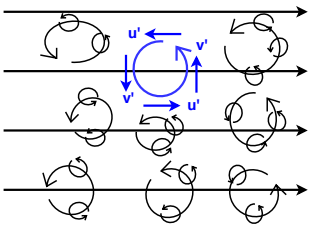

Figure 2.2 – Decomposition in mean and fluctuation velocity components of a turbulent flow, thick blacked arrowed line: mean velocity; blue thick curly line: fluctuation velocity.

decomposition can be expressed as:

$$u_i = \bar{u} + u' \tag{2.1}$$

When the turbulence time scales are much shorter than the transient evolution of a given physical problem (or in a statistically steady flow), scale separation makes it possible to estimate the mean velocity from an average over a finite period of time ($t-\tau/2$ to $t+\tau/2$), with a duration (τ) that is larger than the longest time scale over all eddies.

$$\bar{u}(\vec{x}) = \int_{t-\tau/2}^{t+\tau/2} u_i(\vec{x}, t)\,\mathrm{d}t \tag{2.2}$$

$$u'(\vec{x}, t) = u_i(\vec{x}, t) - \bar{u}(\vec{x}) \tag{2.3}$$

2.1.3 Energy cascade

Richardson [48] was the one to describe turbulence as a superposition of eddies of various sizes. He wrote "*Big whirls have little whirls which feed on their velocity, and little whirls have lesser whirls, and so on to viscosity in the molecular sense*". The largest eddy size is called the integral length scale (L) which, following Kolmogorov's theory [47], can be expressed as a function of turbulence properties (per unit of mass) such as the kinetic energy (k) and the energy dissipation rate (ϵ). Eddies of this size have a characteristic velocity (u) and an associated time scale (τ) that can also be evaluated from analytical relations:

$$\begin{aligned} L &= \frac{k^{\frac{3}{2}}}{\epsilon} \\ u &= \sqrt{\frac{2}{3}\,k} \\ \tau &= L/u = \sqrt{\frac{3}{2}}\,\frac{k}{\epsilon} \end{aligned} \tag{2.4}$$

Consequently, the integral velocity can be calculated from the root-mean-square (RMS) of the fluctuation velocity:

$$u = \left(\overline{u'^2}\right)^{1/2} \text{ where the overline } \bar{\cdot} \text{ means averaging.} \tag{2.5}$$

In isotropic turbulence, it does not matter which component of the fluctuation velocity is

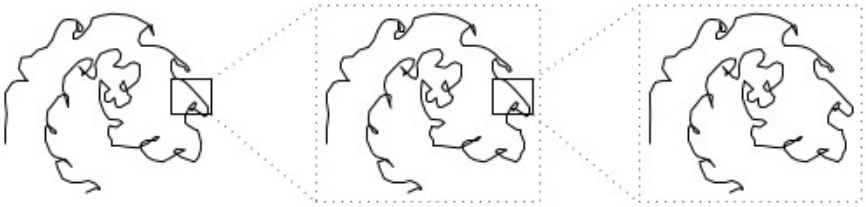

Figure 2.3 – A self similar cascade of eddies in a turbulent flow [57]

used in the calculation of u which is why kinetic energy is simple defined as $k = \frac{1}{2}3u^2$ to account for contribution of the three dimensions. The magnitude of the fluctuation velocity can be estimated from the kinetic energy that is carried by the larger eddies. The Reynolds number associated with these larger eddies is called turbulent Reynolds number, it is given by:

$$Re_L = (k^{1/2}L)/\nu = k^2\epsilon/\nu \tag{2.6}$$

Due to the unstable nature of the larger eddies, they stretch and finally break into smaller eddies, which in turn can stretch and break into smaller eddies, and this process is repeated over all eddy scales, transporting energy from larger scales to smaller structures as pictured in Figure 2.3. This transfer of energy to smaller eddies continues until eddies reach a size small enough for viscous dissipation to be able to dissipate their energy. Basically the rate of dissipation (per unit of mass) can be evaluated from the energy transferred from the largest eddies to all smaller scales. Since these eddies carry a kinetic energy (per unit of mass) of u^2 and their associated time scale is L/u, henceforth transfer rate of energy scales as $\epsilon = u^2/\tau = u^3/L$. On the other hand, smallest eddies are governed by the turbulent dissipation rate (ϵ), that is the rate of energy that is transferred from larger scales, and fluid ability to dissipate energy (per unit of mass), that is its kinematic viscosity (ν). Hence their characteristic length, velocity and time scales can be constructed as combinations of ϵ and ν:

$$\begin{aligned} \eta &= \left(\nu^3/\epsilon\right)^{1/4} \\ u_\eta &= \left(\epsilon\,\nu\right)^{1/4} \\ \tau_\eta &= \left(\nu/\epsilon\right)^{1/2} \end{aligned} \tag{2.7}$$

The ratio between the small and large scales can be evaluated from the expression of the integral scales (2.4) and equations (2.7), and expressed as functions of the turbulent Reynolds number:

$$\begin{aligned} \eta/L &\sim {Re_L}^{-3/4} \\ u_\eta/u &\sim {Re_L}^{-1/4} \\ \tau_\eta/\tau &\sim {Re_L}^{-1/2} \end{aligned} \tag{2.8}$$

2.1.4 Kolmogorov hypotheses

Kolmogorov [47], in 1941, stated three hypotheses based on the observation that velocity,

time and length scales decrease all together. The first hypothesis deals with local isotropy of small scale motions:

1. For homogeneous isotropic turbulence the kinetic energy of eddies is the same everywhere;
2. Directional biases of large scales are lost as energy is transferred to smaller eddies;
3. At sufficiently high Reynolds number, small scale motions are thus statistically isotropic;
4. Local isotropy means isotropy of small scales regardless of the anisotropy of large scales.

Komogorov's first similarity hypothesis states that during energy cascade the information about geometry of eddies also gets lost along with the directional information. At sufficiently high Reynolds number, (L/η large enough), see (2.8), statistics of small scale motions are similar and independent on the mean flow and boundary conditions. Small scales only depend on energy received from larger scales (approximately equal to dissipation rate) and viscous dissipation.

Komogorov's second similarity hypothesis states that at sufficiently high Reynolds number, the statistics of intermediate scales, have a universal form that is determined by the dissipation rate. Smaller eddies have shorter time scales, hence they instantly adapt to fluctuations dictated by larger scales and maintain dynamic equilibrium in the energy transfer rate from larger to smaller eddies. It means that all eddies that are smaller than a given critical eddy size (L_E) and larger than the dissipation micro-scale form a so-called universal equilibrium range. Within this range, intermediate scales still have a relatively large Reynolds number, hence viscous dissipation remains negligible over a wide range of scales. This introduces a new length scale (L_D) that divides the universal equilibrium range into two regions:

inertial subrange in which viscous dissipation is negligible and

dissipation range where energy transfer towards smaller scales decreases while viscous dissipation becomes more and more significant, until no smaller eddies are formed.

As shown in Figure 2.4, scales ranging between L_E and L_D constitute the inertial subrange, while scales smaller than L_D down to the Kolmogorov micro-scale (η) from equation (2.7) constitute the dissipation range.

2.1.5 Developments of linear forcing schemes

The earliest numerical methods for forcing turbulence was the band-limited methods [58], where kinetic energy in the flow was maintained constant by freezing the amplitude of the velocity in all Fourier modes comprised in a given range of wave numbers (i.e. "wave number band"). This method requires some knowledge in advance about the desired kinetic

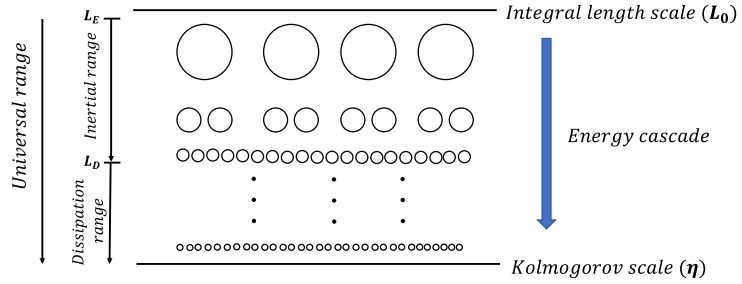

Figure 2.4 – Energy cascading in turbulent flows

energy in such modes, and furthermore excludes any effects of small length scales motion on the dynamics of the large length scales. In 2003, Lundgren [59] proposed an alternative to the band-limited methods of forcing turbulence, using a source term in the Navier-Stokes equation in the form of a volume force that is proportional to the local instantaneous velocity. Apart from its simplicity, the profound advantage of linear forcing is the possibility to apply this method in both physical and Fourier space. Problems that do not admit fully periodic boundary conditions, for instance simulating interactions of turbulence with combustion in which conditions upstream and downstream of the flame are inherently different, are often simulated using numerical codes formulated in physical space, such as with a finite volume method. Rosales and Meneveau [60] have shown that the application of linear forcing in both physical and spectral space yields practically equivalent results, reflecting the profound equivalence of the method in both spaces. Thus, the linear-forcing method opens wide opportunities for application in both physical and spectral space. In this direction, Lundgren [59] showed that linear forcing produces statistics at scales between the integral scale and the inertial range that share the same features as experimental data.

In Fourier space, this linear forcing takes the form of an external force added to the Navier-Stokes equation distributed over of wave numbers (κ) in the three-dimensions covering the shell $|\kappa| = \kappa_f$ or the sphere $0 < |\kappa| \leq \kappa_f$ (excluding the origin) to force isotropic homogeneous turbulence. Theses forces provide energy to the smallest wave numbers (that is the larger scales of the fluid flow) that cascades to smaller scales, until it reaches viscous dissipation. Numerous methods have been proposed to determine the forcing scheme. The most commonly used method [61–64] is given by the expression $\hat{f}(\kappa, t) = A\hat{u}(\kappa, t)$, where u is the velocity field, $\hat{\cdot}$ is the Fourier transform, and the coefficient A is kept constant. Ghosal et al. [65] calculated the source term as $\hat{f}(\kappa, t) = \hat{u}(\kappa, t)\,\epsilon/(N|\hat{u}(\kappa, t)|^2)$ (where N defines the wave number shell) which enforces that the injected energy is constant and controlled by the imposed dissipation rate (ϵ). Carati et al. [66] used this expression but only forced a small subset of wave numbers chosen inside the shell. Another way to control energy injection is by maintaining constant kinetic energy in the smallest wave numbers. This is the approach proposed by Sullivan et al. [67] who multiplied $\hat{u}(\kappa, t)$ by a coefficient that was determined from the change in energy at each time step of the numerical simulation. Seror et al. [68] maintained a constant kinetic energy in the forcing method by injecting again the lost energy during each time step in the range of wave numbers $1 \leq \kappa \leq 5$. The objective was to insert the dissipated energy back to the larger scales. Wang et al. [69] kept

the energy constant in each of the first two shells with wave numbers $0.5 < \kappa \leq 1.5$ and $1.5 < \kappa \leq 2.5$ while ensuring that the energy ratio between these two shells was consistent with the Kolmogorov scaling law ($\kappa^{-5/3}$).

The above mentioned methods undoubtedly solve the Navier-Stokes equations in Fourier space. Doing so, they require knowledge of Fourier-transformed velocities, quantities that are not readily available in codes formulated in physical space. Thus, there is interest in developing forcing schemes that do not depend upon Fourier space representations.

This section will basically deal with the numerical approach used to generate homogeneous isotropic turbulence. Section 2.1.6 will detail how to generate turbulence by using the approach mentioned in the literature [59]. Mainly in this case turbulence is produced in physical space rather than Fourier space because of its easier application. In section 2.2, the lattice-Boltzmann method used for simulating fluid flow is described, in which the mathematical expression of the linear forcing is given.

2.1.6 Linear forcing scheme in physical space

Lundgren [59] showed that a forcing function that is directly proportional to velocity makes sense from a physical perspective and provided results accurately producing homogeneous turbulence. He stated that the fluctuation part of the velocity (u') in shear flow turbulence satisfies the following expression:

$$\frac{\partial u'}{\partial t} + \overline{u} \cdot \nabla u' + u' \cdot \nabla \overline{u} + u' \cdot \nabla u' - \nabla \cdot \overline{u'u'} = \nabla p'/\rho + \nu \nabla^2 u' \tag{2.9}$$

where the prime symbols denote turbulent fluctuations as defined in equation (2.1). The vector symbol ($\vec{.}$) is omitted in this equation to avoid cluttered notations (with $.'$ and $\bar{.}$), but velocities $\bar{u}$, u' and u_i all have three components. The third term on the left hand side in equation (2.9), $u' \cdot \nabla \overline{u}$ is the energy production term. As in isotropic homogeneous turbulence there exists no mean flow gradient, this equation can be simplified as:

$$\frac{\partial u'}{\partial t} + u'.\nabla u' = -\frac{1}{\rho}\nabla p + \nu \nabla^2 u' + g \tag{2.10}$$

where the driving force parameter per unit mass can be given the form a linear forcing:

$$g = A\, u' \tag{2.11}$$

Projecting equation (2.10) on u' and averaging it yields the turbulent energy equation given by Lundgren [59]:

$$\frac{1}{2}\frac{\partial \langle u' \cdot u' \rangle}{\partial t} = -\epsilon + A\langle u' \cdot u' \rangle \tag{2.12}$$

in which the dissipation rate (ϵ) is expressed as:

$$\epsilon = -\nu \langle u' \cdot \nabla^2 u' \rangle \tag{2.13}$$

In statistically stationary state, the time derivative of average quantities is zero, in which

case equation (2.12) gives a value for parameter A in established turbulence:

$$A = \frac{\epsilon}{3u_{rms}^2} \tag{2.14}$$

where ϵ represents the dissipation rate and u_{rms} stands for the root-mean-square (RMS) of the fluctuation velocity (the prime is omitted since only the RMS of the fluctuating component is ever used in this work). Parameter A can thus be prescribed a value, and keeping it constant is equivalent to prescribing the eddy turn over time scale, that is $\tau \approx 0.612\, A^{-1}$ from the relations in equation (2.4). An alternate process can also be used where the parameter A is recalculated at each time step by calculating the values of u_{rms}^2 from the simulation, which means imposing a constant energy injection rate (ϵ_0).

In homogeneous turbulence, u_{rms}^2 can be calculated at each instant from a volume average:

$$\langle u_{rms}^2 \rangle^V = \frac{1}{V} \iiint_V \frac{u' \cdot u'}{3} \, \mathrm{d}^3V \tag{2.15}$$

where u' still denotes the fluctuation velocity that can be calculated as the difference between instantaneous velocity (u_i) and the mean velocity ($\bar{u}$). The division by 3 is due to the summation over the three components in the dot product, while by convention the characteristic fluctuation velocity (u') is considered per component since it makes it easier to characterize non-isotropic turbulence, even though this is not needed here and it leads to the non-intuitive convention that the scalar value u'^2 is one third of $u' \cdot u'$. Instantaneous velocity (u_i) is evaluated directly from the simulation while, in homogeneous turbulence, mean velocity ($\bar{u}$) can also be calculated with a volume average:

$$\langle \bar{u} \rangle^V = \frac{1}{V} \iiint_V u_i \, \mathrm{d}^3V \tag{2.16}$$

Eventually, the Navier-Stokes derived equation to be numerically solved is summarized in Lundgren [59]:

$$\frac{\partial u_i}{\partial t} + u_i \cdot \nabla u_i = -\frac{1}{\rho}\nabla p + \nu \nabla^2 u_i + \left(\frac{\epsilon_0}{3u_{rms}^2} \right) u' \tag{2.17}$$

In his work, Lundgren [59] does not distinguish between u_i and u' in expression (2.17) since his flow has a zero mean velocity. In this chapter, simulations similar to his are conducted. However, later in our research, linear forcing will be applied to flows with non-zero mean velocity profiles which is why the different velocity components must be clearly identified.

2.2 Lattice Boltzmann method

Fluid dynamics are ruled by the Navier-Stokes equations for mass and momentum. These equations are most commonly numerically resolved using finite volume methods, in which they are discretized and integrated over elementary volumes. However, lattice Boltzmann

methods (LBM) do not directly discretize the Navier-Stokes equations, but instead resolve them indirectly by solving a Boltzmann like problem in each node of a lattice, leveraging the fact that the global behavior of particles ruled by Boltzmann equation can yield Navier-Stokes solutions when they are seen as a continuum, provided that proper collision dynamics is used in the Boltzmann equation. The mathematical proof of this, called Chapman-Enskog expansion, was independently published by the two eponymous researchers Chapman [70], Enskog [71].

In the late 1980's, lattice gas automata started being developed to simulate gas behavior at molecular scale (for small scale dynamics or rarefied conditions). In such methods, gas particles were moving between the nodes of a lattice and collision between particles was calculated at node positions [72]. However, due to limitations mainly in their noisy nature and their introduction of spurious terms in the Navier-Stokes equations, such methods do not apply well to general fluid flow simulations. Therefore discrete gas particles were replaced by density distribution functions that make smoother representations of particle populations in each lattice node. These were introduced to nullify the noise and to capture better collision statistics, which gave birth to the lattice Boltzmann methods. Since the fluid dynamics in the macroscopic world are the outcome of the average microscopic particle behaviors, then details in physics of individual particles have no impact on the macroscopic physics [73].

From this approach, lattice Boltzmann methods have been developed that combine the main advantages of being second order accurate schemes while having nice properties for numerical resolution: their numerical scopes are local with minimal interactions of the neighbor cells and they are explicit in time, which makes them particularly suited for parallel computing platforms. In multiphase and complex flows, due to the presence of moving and/or deformable interfaces, conventional CFD faces challenges relative to its needs of a good mesh on which to discretized and solve Navier-Stokes equations. However, the interfaces that separate phases can also be seen as specific interactions among the constitutive elements of the phases at microscopic scale, which are often more easily expressed in a Boltzmann form. Therefore, in LBM, the kinetics of particles sometimes provide an easier and consistent way to account for interfaces by adjusting the collision operator accordingly.

The LBM that has been used in this work is the one described in Eggels and Somers [1]. It has been implemented in an in-house code to numerically resolve fluid flows. As for any LBM, this method relies on the discretization of Boltzmann's equation (2.18) over a finite set of velocities ($\vec{c_i}$) corresponding to the links between the nodes of a lattice (with $i \in [1, 18]$ in Eggels and Somers [1]), as illustrated in Figure 2.5. Distribution $N_i(\vec{x}, t)$ corresponds to the density of mass at position $\vec{x}$ and at time t that is moving at velocity $\vec{c_i}$.

$$\frac{\partial N_i}{\partial t} + \vec{c_i} \cdot \vec{\nabla} N_i = \Omega_i(N_1, \ldots, N_{18}) + F_i(\vec{f}) \tag{2.18}$$

The variables describing the fluid flow are obtained by calculating the moments of the distributions (N_i) from the discretized Boltzmann's equation.

$$\rho = \sum_i N_i, \quad \rho\vec{u} = \sum_i \vec{c_i} N_i \tag{2.19}$$

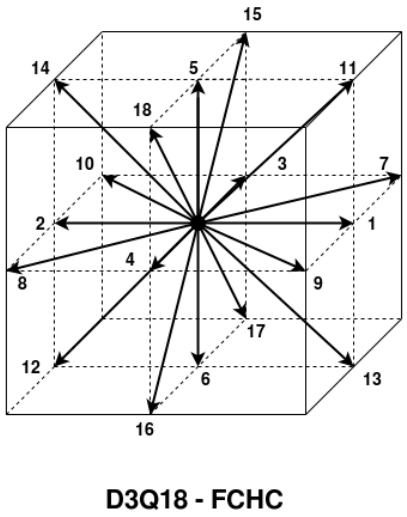

Figure 2.5 – D3Q18 velocity model in LBM

The Boltzmann equation being discretized over a lattice defining a finite set of positions in space ($\vec{x}$) and a finite set of velocities ($\vec{c}_i$), the lattice definition yields a time step so that distributions (N_i) move by one node in their associated direction during such a time step. This step is called "streaming" and results from time integration of equation (2.18), it accounts for the convective term in Boltzmann's equation. The diffusive and source terms can, for their part, be applied locally in each node before the streaming step, in a so-called "collision" step.

$$\begin{aligned} \text{collision:} \quad & \tilde{N}_i(\vec{x},t) = N_i(\vec{x},t) + \Big(\Omega_i(\vec{x},t) + F_i(\vec{x},t)\Big)\Delta t \\ \text{streaming:} \quad & N_i(\vec{x} + \vec{c}_i\,\Delta t, t + \Delta t) = \tilde{N}_i(\vec{x},t) \end{aligned} \tag{2.20}$$

Equation (2.20) shows that Boltzmann's equation is thus solved with an explicit scheme. Starting from the initial time, the flow dynamics at each time step are solved in two sub steps : (a) streaming step that streams the density distribution functions from each node to its neighbors, following the lattice discrete set of velocities, illustrated in Figure 2.6, and (b) collision step that redistributes the mass densities among the velocity directions in each lattice node.

External volume forces ($\vec{f}$) can be added through the source term denoted F_i in equation (2.18). In Eggels and Somers [1], the source term (F) and the collision operator (Ω) are merged and calculated together during the collision step. From equation (2.19), mass and momentum can be calculated through the zeroth and first moments of the density distributions, which yields constraints on the collision operator to satisfy conservation laws of mass and momentum.

$$\begin{aligned} \Omega_i^{\text{E\&S}}(N_1,\ldots,N_{18},\vec{f}) &= \Omega_i(N_1,\ldots,N_18) + F_i(\vec{f}) \\ \sum_i \Omega_i^{\text{E\&S}} = 0, \quad \sum_i \vec{c}_i\,\Omega_i^{\text{E\&S}} &= \vec{f} \end{aligned} \tag{2.21}$$

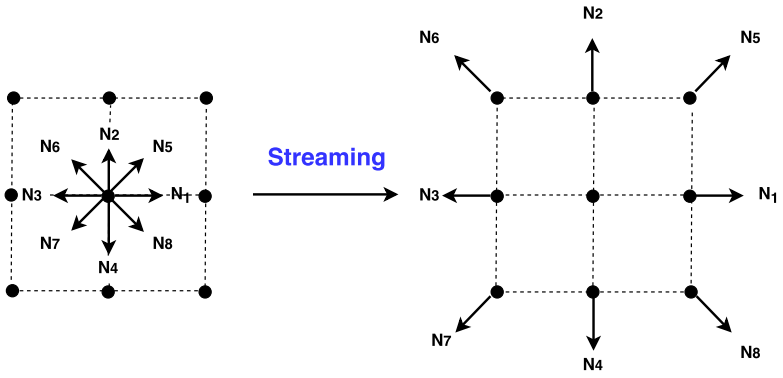

Figure 2.6 – Illustration of the streaming process between LB nodes

Eggels and Somers [1]'s collision operator ($\Omega^{\mathrm{E\&S}}$) depends in a nonlinear way on all components of the density distributions (N_i). In the case of forced isotropic turbulence, the source term $\vec{f}(\vec{x},t)$ is computed via the linear forcing method.

Here, a D3Q18 lattice-Boltzmann method is implemented. The lattice comes with its unit for space and for time. The unit for space is given by the distance between nodes along primary directions (Δx), so that the cube in Figure 2.5 has a side of $2\,\Delta x$. The time unit is given by the velocity discretization so that distributions move by one node during one time step during streaming, that is $\Delta t = \|\vec{c}_1\|/\Delta x$ (since $\vec{c}_1$ corresponds to the x direction). In the following, LBM quantities will then be non-dimensionalized using these two scales (Δx and Δt), so that, for example Δt from equation (2.20) will be equal to unity ($\Delta t = 1$). Velocities will be scaled by $\Delta x/\Delta t$.

In lattice units, the discrete sets of velocities used in the D3Q18 lattice shown in Figure 2.5, can be expressed as:

$$\vec{c}_i = \begin{cases} (\pm 1,0,0),(0,\pm 1,0),(0,0,\pm 1), & \text{for } i = 1,\ldots,6 \quad \text{Group I} \\ (\pm 1,\pm 1,0),(0,\pm 1,\pm 1),(\pm 1,0,\pm 1), & \text{for } i = 7,\ldots,18 \quad \text{Group II} \end{cases} \tag{2.22}$$

Eggels and Somers [1]'s method is based on the premise that equation (2.18) is equivalent to Navier-Stokes equations if the collision operator relaxes towards the following equilibrium distribution (N_i^{eq}):

$$N_i^{\mathrm{eq}} = \frac{m_i\,\rho}{24}\Bigg\{1 + 2\,\vec{c}_i\cdot\vec{u} + 3\,\left[\vec{c}_i\vec{c}_i : \vec{u}\vec{u} - \frac{1}{2}\mathrm{tr}(\vec{u}\vec{u})\right] - 6\nu\left[(\vec{c}_i\cdot\vec{\nabla})(\vec{c}_i\cdot\vec{u}) - \frac{1}{2}\vec{\nabla}\cdot\vec{u}\right] + O(u^3,\ u\nabla u)\Bigg\} \tag{2.23}$$

where $O(u^3,\ u\nabla u)$ denotes higher order terms that do not exist in Navier-Stokes equation and that must thus be kept small. This is achieved by ensuring that the velocity ($\vec{u}$) is small

compared to the speed of sound in the given lattice which is here $c_s = \sqrt{\frac{1}{2}}$.

$$\|\vec{u}\| \ll c_s \tag{2.24}$$

Equation (2.24) adds a criterion in the form of a numerical Mach number to ensure that propagation of information in the lattice does not limit the convection and diffusion terms in equation (2.18). This is the counterpart of using a fully explicit solver as detailed in equation (2.20) that imposes limitations on the simulation time step.

Equation (2.23) can be obtained as a discrete form of the Maxwellian equilibrium distribution from the kinetic theory of gases. The weight factors (m_i) derive from the definition of the D3Q18 lattice and the projection of the Maxwell distribution over the discrete set of velocities in the LBM:

$$m_i = \begin{cases} 1/12, & i = 1, \ldots, 6 \quad \text{Group I} \\ 1/24, & i = 7, \ldots, 18 \quad \text{Group II} \end{cases} \tag{2.25}$$

The foundations of LBM were laid by Bhatnagar et al. [2], who defined their collision operator (Ω^{BGK}) as a relaxation towards the equilibrium distribution using a single relaxation time (τ^{BGK}) that is related to the kinematic viscosity of the fluid (ν):

$$\Omega_i^{\text{BGK}} = \frac{1}{\tau^{\text{BGK}}}(N_i^{\text{eq}} - N_i) \quad \text{with} \quad \nu = c_s^2(\tau - \Delta t/2) \tag{2.26}$$

Later developments of the LBM, such as the Multiple-Relaxation-Time (MRT) scheme [74] do a projection of the distributions in a different basis of eigenvectors than the lattice velocities ($\vec{c_i}$), so that various projections can be relaxed with different relaxation times, hence the name of such methods. Relaxing different moments of the distributions with different times makes it possible to significantly damp the high order terms from equation (2.23) and improves the quality of the resolution of the NS equations by the LBM. More specifically, it makes such methods more robust over a wider range of numerical Mach numbers and of viscosity values. Although prior to D'Humières et al. [74], Eggels and Somers [1]'s operator is a kind of MRT, in which physical moments from the Boltzmann distributions (mass, momentum and energy) and unphysical moments (high order terms) are relaxed separately. The collision operator ($\Omega^{\text{E\&S}}$) applies to a so-called solution vector (Λ) defined with moments of multiple orders of the distributions (N_i).

$$N_i(\vec{x} + \vec{c}_i, t+1) = [P]_i^{-1} \underbrace{(1 + [\Omega^{\text{E\&S}}])}_{\Lambda^+} \overbrace{[P]\, N_i(\vec{x}, t)}^{\Lambda^-} \tag{2.27}$$

Reusing the notations from equation (2.20), pre- and post-collision solution vectors (respectively Λ^- and Λ^+) can be expressed as:

$$\begin{aligned} \Lambda^-(\vec{x}, t) &= [P] N_i(\vec{x}, t) \\ \Lambda^+(\vec{x}, t) &= [P] \tilde{N}_i(\vec{x}, t) \end{aligned} \tag{2.28}$$

where matrix $[P]$ is the projection matrix from the velocity basis ($\vec{c}_i$) to a new basis of eigenvectors (ϕ_i) defined as:

$$\phi_i = \left\{ \begin{array}{c} 1 \\ c_{ix} \\ c_{iy} \\ c_{iz} \\ 2c_{ix}^2 + c_{iy}^2 + c_{iz}^2 - 2 \\ c_{ix}c_{iy} \\ 2c_{iy}^2 + c_{ix}^2 + c_{iz}^2 - 2 \\ c_{ix}c_{iz} \\ c_{iy}c_{iz} \\ 2c_{iz}^2 + c_{ix}^2 + c_{iy}^2 - 2 \\ c_{ix}(3c_{iy}^2 - 1) \\ c_{iy}(3c_{ix}^2 - 1) \\ 3c_{ix}(2c_{iz}^2 + c_{iy}^2 - 1) \\ 3c_{iy}(2c_{iz}^2 + c_{ix}^2 - 1) \\ c_{iz}(3c_{ix}^2 + 3c_{iy}^2 - 2) \\ 3c_{iz}(c_{iy}^2 - c_{ix}^2) \\ 3(c_{ix}^2 - c_{iy}^2)^2 - 2 \\ (c_{ix}^2 - c_{iy}^2)(1 - 2c_{iz}^2) \end{array} \right\} \tag{2.29}$$

so that the solution vectors ($\Lambda^{\pm}$) have the following 18 components:

$$\Lambda^{\pm} = \left| \begin{array}{l} \rho \\ \rho\vec{u} \pm \dfrac{1}{2}\vec{f} \\ \rho\vec{u}\vec{u} + \rho\dfrac{\pm 1 - 6\nu}{6\nu}\left(\overline{\overline{\nabla}}\vec{u} + \left(\overline{\overline{\nabla}}\vec{u}\right)^{\mathrm{T}}\right) \\ O(u^3, u\nabla u) \\ O(u^4, u^2\nabla u) \end{array} \right. \tag{2.30}$$

Consistently with equation (2.21), external volume forces ($\vec{f}$) are directly implemented during the collision step as an additional term in moments of order 1, corresponding to momentum components.

2.3 Simulation conditions and setup

Direct numerical simulations of homogeneous isotropic turbulence were performed with the LBM solver described in section 2.2 in which the linear forcing described in section 2.1.5 was used as local volume force. The computational domain is a three dimensional cubic box with periodic boundary conditions along all three directions. In the simulations, the LBM code is used to compute incompressible flow solutions. Similarly to the previous section, all values in this section are expressed in lattice units ($1\,[\mathrm{lu}] = 1\,\Delta x$ and $1\,[\mathrm{tu}] = 1\,\Delta t$), unless explicitly stated otherwise.

The largest eddies, referred to as integral length scale, carry most of the energy. The smallest eddies, referred to as Kolmogorov length scale, are scaled by the energy dissipation rate and fluid viscosity. In a statistically steady turbulent flow, the energy dissipated at smaller scales equals the energy supplied by larger scales. The eddies are also constrained by the size of the simulation box.

Consistently with equation (2.17), the control parameter implemented in the simulation code is the energy injection rate ϵ_0 which is kept constant throughout the simulation. The simulation conditions are characterized by three parameters:

integral length scale L, assumed to be 20% of the domain size [60], that gives a length scale to the simulations;

fluctuation velocity u', which, when combined with L_0, gives a time scale for the simulations;

Kolmogorov length scale η, which determines the smallest scales in the simulation and consequently determines the turbulent Reynolds number.

Rosales and Meneveau [60] determined that the implementation of linear forcing scheme leads to the production of turbulent velocity field that asymptotically reaches a unique statistically steady solution. The integral length scale (L_0) when this state is reached is approximately 20% of the domain size (that is the length of an edge of the cube). When statistically steady turbulent flow is achieved, the fluctuation velocity u_0', the mean turbulent kinetic energy k_0 and the mean rate of dissipation ϵ_0 are expressed as:

$$u_0' = 3\,A\,L_0, \quad k_0 = \frac{27}{2}\,A^2\,L_0^2, \quad \epsilon_0 = 27\,L_0^2\,A^3 \tag{2.31}$$

where A is the forcing coefficient defined in (2.14).

The value of ϵ_0 has been calculated as $\epsilon_0 = {u_0'}^3/L_0$ [75] where u_0' represents the target fluctuation velocity (see Table 2.1), chosen small enough so that the simulations obey the incompressibility restriction from (2.24).

The forcing parameter A is calculated from its relation to ϵ_0 and L_0 in equation (2.31). The resulting forcing Reynolds number (Re_{force}) was varied in several simulation cases summarized in Table 2.1 to investigate the influence of the Kolmogorov length scale. Moin and Mahesh [76] established that for a well resolved direct numerical simulation, the Kolmogorov length scale should obey the criterion:

$$\eta > 0.318\,[\text{lu}] \tag{2.32}$$

Given η, the value of kinematic viscosity ν is set by Kolmogorv's theory from equation (2.7) which is used as an input value in the simulations. Knowing the parameters u_0', L_0 and ν, a forcing Reynolds number is obtained that characterizes the conditions of a simulation.

$$Re_{force} = \frac{u_0'\,L_0}{\nu} \tag{2.33}$$

2.3.0.0.1 Scaling parameters

Simulations parameters are given in lattice units but, in order to have a proper understanding of what is happening in the physical world, it is possible to convert from lattice

Table 2.1 – Simulation parameters of forced isotropic turbulence (in lattice units)

Case	N^3	ν	ϵ_0	u_0'	Re_{force}	L_0	η
a	128^3	7.4×10^{-4}	4×10^{-6}	0.05	8513	25.2	0.1
b	128^3	6.3×10^{-3}	4×10^{-6}	0.05	1000	25.2	0.5
c	128^3	1.6×10^{-2}	4×10^{-6}	0.05	394	25.2	1
d	128^3	4×10^{-2}	4×10^{-6}	0.05	158	25.2	2

units to physical ones. The following relations provide conversions for length and time.

$$\Delta x_{\text{phys}} = \frac{H_{\text{phys}}}{N}, \quad \Delta t_{\text{phys}} = \frac{\Delta x_{\text{phys}}^2}{\nu_{\text{phys}}}\,\nu_{\text{LBM}} \tag{2.34}$$

where H_{phys} is the corresponding length of an edge of simulation box in physical units, N is the number of lattice nodes along that direction. ν_{phys} and ν_{LBM} are the value of the kinematic viscosity of the fluid respectively in physical units and in lattice units. Then Δx_{phys} is the distance in physical units between two lattice nodes, Δt_{phys} is the duration of simulation time step (streaming plus collision) in physical units.

Knowing these values it is possible to convert velocity, kinetic energy, dissipation rate etc. in physical space, for example:

$$u_{\text{phys}} = u\Delta x_{\text{phys}}/\Delta t_{\text{phys}} \tag{2.35}$$

In later physical interpretations, the value for the physical kinematic viscosity will be that of steel $\nu_{\text{phys}} = 7.86 \times 10^{-6}\text{m}^2\text{s}^{-1}$ and the simulation domain size (H_{phys}) will be $0.01\,\text{m}$. Also, as long as only kinematics are studied, all LB quantities are proportional to ρ so there is no lattice scale for mass. By conventions, the simulations will use $\rho_{\text{LBM}} = 8$ and steel is $\rho_{\text{phys}} = 7000\,\text{kg}\cdot\text{m}^{-3}$. This yields a mass unit, that will be necessary for conversions:

$$\Delta m_{\text{phys}} = \frac{\rho_{\text{phys}}}{\rho_{\text{LBM}}}\left(\Delta x_{\text{phys}}\right)^3 \tag{2.36}$$

2.4 Analysis of the turbulence produced by linear forcing

In this chapter discussions and conclusions are drawn from the results of isotropic turbulence generated by linear forcing. Section 2.4.1 depicts the confirmation of the statistically steady state of the turbulence by viewing the evolution over time of different parameters. Turbulence energy spectrum is analyzed in section 2.4.2 which gives a valid conclusion of the cascading of different scales with the energy dissipation. Eventually, in section 2.4.3, a validation is presented by comparing our results to those of Valiño et al. [77].

2.4.1 Evolution over time of characteristic parameters

2.4.1.1 Kinetic energy and dissipation rate in the forced turbulent flow

In the figures presented in this section, time has been non-dimensionalized relative to the characteristic time $\tau_0 = u_0'^2/\epsilon_0$. This characteristic time is about half of the eddy turnover time (τ) defined in equation (2.4):

$$\tau_0 = \left(\frac{2}{3}\right)^{\frac{3}{2}}\tau \approx 0.54\,\tau \tag{2.37}$$

All simulations were initialized with no turbulence, but with a sum of sinusoidal profiles for each velocity component. The magnitude of the initial velocity is the same as the

expected fluctuation velocity (u_0'). Linear forcing and flow solver would then compute the evolution from this initial state to a statistically steady turbulent state.

The mean velocity remains almost zero in all cases as shown in Figure 2.7:

$$\|\langle \vec{u}_i \rangle^V\| < 2\%\ u_0' \tag{2.38}$$

Figure 2.8 shows the contour map of the velocity magnitude and the streamlines of the velocity fields in the x-z plane. From these figures a clear representation of the isotropic vortices can be observed which is the main objective of performing the simulations.

What all curves from Figures 2.9 and 2.10 show is that steady state is reached in about $t = 20\,\tau_0$. The plotted dissipation rate (ϵ) and kinetic energy (k) have been calculated from the simulated velocity fields:

$$\langle \epsilon \rangle^V = 2\,\nu\,\langle S_{ij} S_{ij} \rangle^V \tag{2.39}$$

$$\langle \epsilon_{\text{cd}} \rangle^V = -\nu\,\langle \vec{u'} \cdot \Delta^2 \vec{u'} \rangle^V \tag{2.40}$$

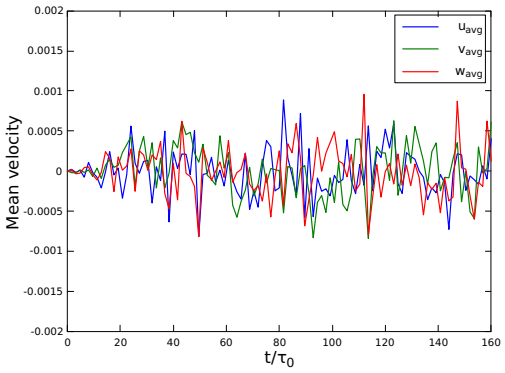

Figure 2.7 – Time evolution of Mean velocity along three directions for LBM simulation where $\eta = 0.1$ [lu], here $t = t_{LBM}/\tau_0$

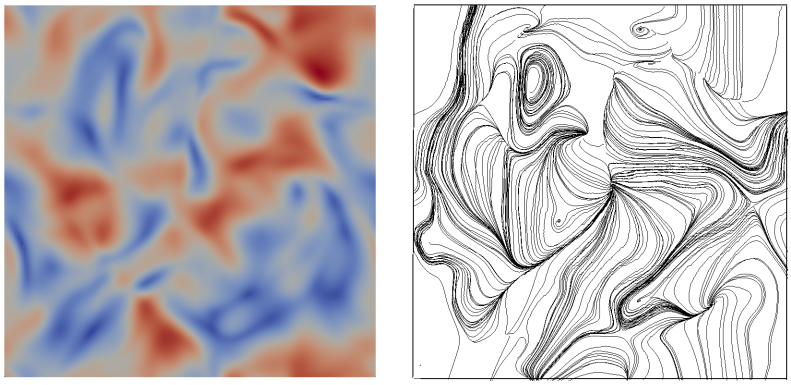

(a) (b)

Figure 2.8 – (a) Velocity magnitude map and (b) streamlines of velocity fields in x-z direction for $\eta = 1$ [lu]

$$\langle k \rangle^V = \left\langle \frac{1}{2} \vec{u'} \cdot \vec{u'} \right\rangle^V \tag{2.41}$$

where $\langle . \rangle^V$ denotes spatial volume average over the whole simulation domain and $\vec{u'}$ is calculated as the difference between the instantaneous velocity and the mean velocity, also calculated as a volume average.

$$\vec{u'} = \vec{u}_i - \langle \vec{u}_i \rangle^V \tag{2.42}$$

Since dissipation rate and turbulence kinetic energy are calculated as volume averages, their instantaneous values can be evaluated at any time in the simulation.

Figure 2.9 shows the evolution of energy dissipation rate over time. The horizontal red line represents the controlled dissipation rate ($\epsilon_0 = 4 \cdot 10^{-6}$) in the linear forcing, and the other lines are calculated dissipation rates from the simulations. The two sub-graphs show the results of the two different ways to calculate the energy dissipation rate. Numerical evaluation of dissipation rate according to equation (2.39) makes use of the strain rate tensor (S_{ij}) that is calculated from the Boltzmann distributions during the collision step in the LBM [75]. The second expression, equation (2.40), represents the dissipation rate calculated based on the formulation given by Rosales and Meneveau [60] where the second order space derivatives of the velocity field are evaluated using centered finite-difference scheme. Figure 2.9 shows that both calculations yield different values, but both values (for $\eta \geq 0.5$ [lu]) are in good agreement with the control value, meaning that the linear forcing accurately imposes the dissipation rate with which it is parameterized. Moreover, one calculation method seems to overestimate and the other to underestimate the dissipation rate, which is consistent with the expectation that the effective dissipation rate lays in between and is very close to the control value from the linear forcing. However, the blue curve for $\eta = 0.1$ [lu], that is a Kolmogorov length scale ten times smaller than a lattice spacing, gives inaccurate results. It is an illustration of the criterion from equation (2.32) meaning that in such simulations space discretization is not fine enough to represent the smallest eddies.

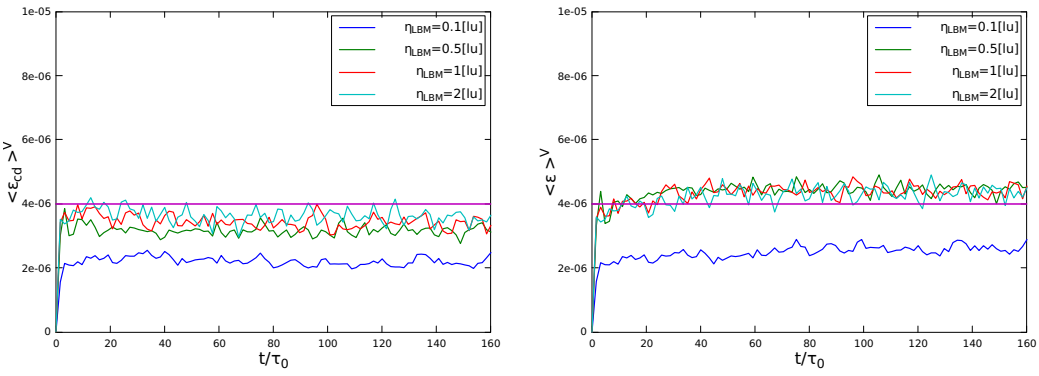

(a) (b)

Figure 2.9 – Time evolution of the dissipation rates calculated as (a) $\langle \epsilon_{\text{cd}} \rangle^V = -\nu \langle u' \Delta^2 u' \rangle^V$ and (b) $\langle \epsilon \rangle^V = 2\nu \langle S_{ij} S_{ij} \rangle^V$ for different Kolmogorov length scales: (a) $\eta = 0.1$[lu], (b) $\eta = 0.5$[lu] , (c) $\eta = 1$[lu] and (d) $\eta = 2$[lu], here $t = t_{LBM}/\tau_0$

To extract more quantitative information from the simulations, Table 2.2 shows the mean values of the fluctuation velocity (u') and the integral length scale (L), time averaged over a period of $80\,\tau$ after $t \geq 20\,\tau$, that is their mean values in statistically steady state.

The energy dissipation which is evaluated based on finite-difference scheme is inherently prone to numerical errors due to discretization. The dissipation rate calculated from the strain rate tensor in the LBM, in equation (2.39), is in relatively good agreement with the control value, judging by the relative errors which is about $10\,\%$ or less when $\eta \geq 0.5$ [lu]. The decrease of the percentage of error when the Kolmogorov length scale increases may solely be due to a better estimation of ϵ from equations (2.39) and (2.40) that does not correspond to an actual relation between the effectively imposed dissipation rate and the fineness of the mesh.

Figure 2.10 shows the evolution over time of the volume averaged calculated turbulent kinetic energy, from equation (2.41), and integral length scale. The integral length scale is evaluated at each instant based on the expression $L = u'^3/\epsilon$. Among these curves, the blue lines $\eta = 0.1$ [lu] reflect inaccurate results, for the same reasons discussed before and in equation (2.32). All other curves match the control values for turbulence kinetic energy $(k_0 = 3.4 \times 10^{-3})$ and integral length scale $(L_0 = 25.2)$ very well. The integral length scale (L) occupies approximately 20% of the domain size, when statistically stationary turbulence is reached. Evaluating the various turbulence parameters from the simulation (Table 2.2) it can be seen that the fluctuating velocity (u') also reaches the desired control value, i.e. $u'_0 = 0.05$, as mentioned in Table 2.1 for all Kolmogorov length scales but $\eta = 0.1$ [lu]. This depicts that the flow field generated, matches physically sound turbulent behavior.

Also to validate homogeneity and isotropy, RMS fluctuation velocities calculated with time averages have been performed. To this end, first the mean velocity is calculated from an average over time, and then the "mean" step in the RMS also averages with time. Such calculations yield average values independently calculated in every position. Due to ergod-

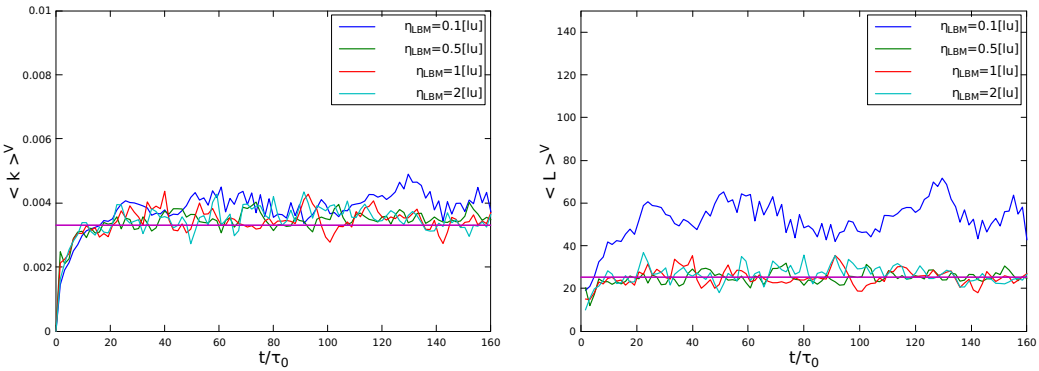

(a) (b)

Figure 2.10 – Time evolution of (a) turbulence kinetic energy k and (b) integral length scale L for different Kolmogorov length scales: (a) $\eta = 0.1$[lu], (b) $\eta = 0.5$[lu] , (c) $\eta = 1$[lu] and (d) $\eta = 2$[lu], here $t = t_{LBM}/\tau_0$

Table 2.2 – Simulation results of turbulence parameters(in lattice units)

Case	u'	u'_0	Re_λ	L	L_0
a	0.053	0.05	193.03	48.35	25.2
b	0.0479	0.05	56.41	25.35	25.2
c	0.0476	0.05	34.95	25.07	25.2
d	0.0482	0.05	22.76	26.86	25.2

icity of turbulence, time and volume average are supposed to give the same results. So the time averaged values can be used to validate that the forced turbulence is homogeneous and isotropic as is is supposed to be.

Time averages are calculated in the following way:

$$\langle . \rangle^t = \frac{1}{n} \sum_{i=0}^{n-1} . (t_0 + i\Delta t) \tag{2.43}$$

where t_0 has been chosen large enough so that steady state is reached. 200 snapshots are evaluated every 1000 time steps, ($\Delta t_{TS} = 1000$) time steps, covering a total range of 200×1000 time steps, corresponding to $150\tau_0$.

Profiles of the time based RMS of the three components of the fluctuation velocity are plotted in in Figure 2.11. Their profiles are fairly flat and the magnitude of all components are similar, which confirms that the forced turbulence does not vary with position (homogeneity) and has no preferential direction (isotropy).

Also, plotting profiles of time averaged turbulent kinetic energy along several lines in the domain, as observed in Figure 2.12, shows that the calculated value achieves the desired controlled value (k_0) in every location.

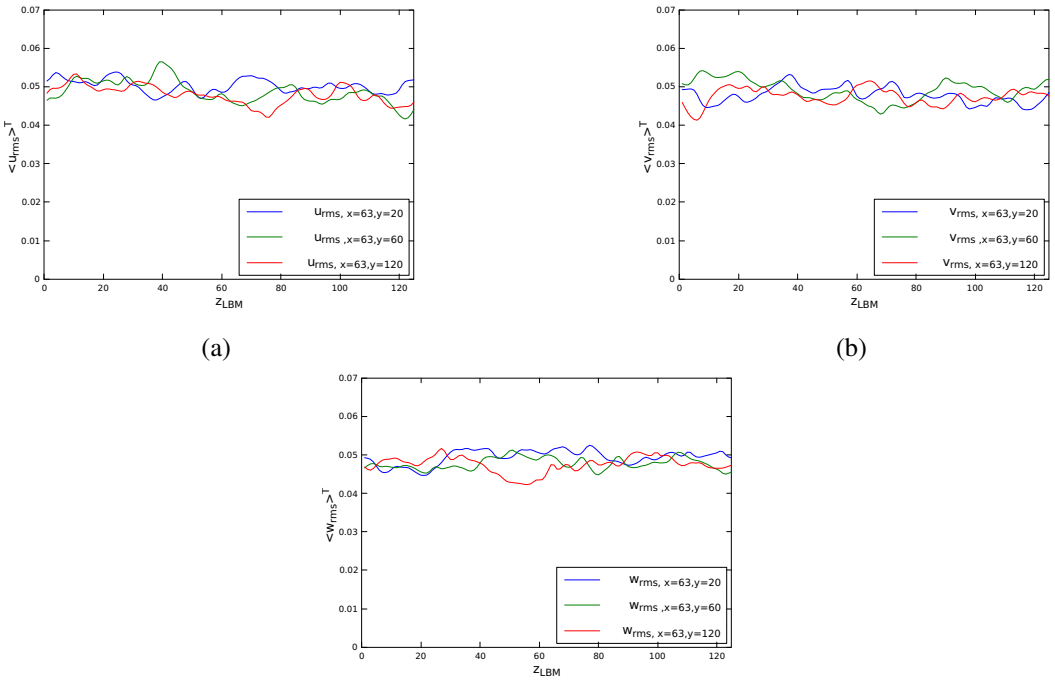

(a) (b)

(c)

Figure 2.11 – Plot of (a) u_{rms}, (b) v_{rms} and (c) w_{rms} along the z-direction (z_{LBM}) for $\eta = 0.5$[lu] at x-location, $x_{LBM} = 63$ and y-locations $y_{LBM} = 20, 60, 120$.

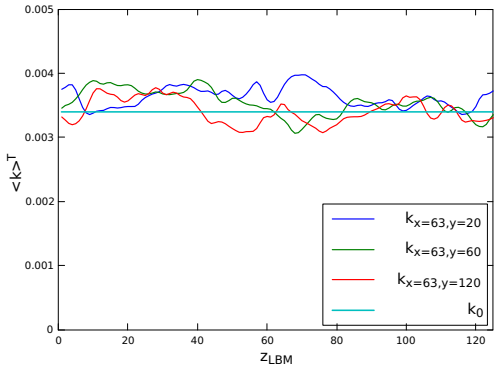

Figure 2.12 – Plot of turbulence kinetic energy along the z-direction (z_{LBM}) for $\eta = 0.5$[lu] at x-location, $x_{LBM} = 63$ and y-locations $y_{LBM} = 20, 60, 120$, and controlled value $k_0 = 0.0034$.

2.4.1.2 Characterisation of fluctuations: velocity derivative skewness

After the properties of the forced flow regarding energy have been validated, another property of the flow regarding local hydrodynamics is studied to get better validation on the properties of the forced velocity field. Velocity derivative skewness gives a definite representation of the velocity gradients thus providing information on the local structures in the flow.

Velocity derivative skewness is used to characterize velocity derivatives: $\partial u'_x/\partial x$, where

u'_x is the x component of velocity fluctuations. There is a general link between the skewness, cascade of energy between scales and vortex stretching [78]. Skewness is defined as the third moment of fluctuation velocity gradient normalized by variance [79]. The expression for velocity derivative skewness along the x direction is given by:

$$S_{u\,x} = \frac{\left\langle \left(\frac{\partial u'_x}{\partial x}\right)^3 \right\rangle^V}{\left\langle \left(\frac{\partial u'_x}{\partial x}\right)^2 \right\rangle^{V\,3/2}} \tag{2.44}$$

The expected value of this skewness in homogeneous turbulence lies between -0.4 and -0.5 [80]. Figure 2.13 illustrates the time evolution of velocity derivative skewness for different Kolmogorov length scales. Again, this parameter reaches values in very good agreement with known turbulence properties except for $\eta = 0.1$ [lu].

The time averaged values once statistically steady regime is achieved are included in Table 2.3. These confirm that the local hydrodynamics of the turbulence produced by linear forcing match the expected turbulent behavior when the criterion in equation (2.32) is satisfied.

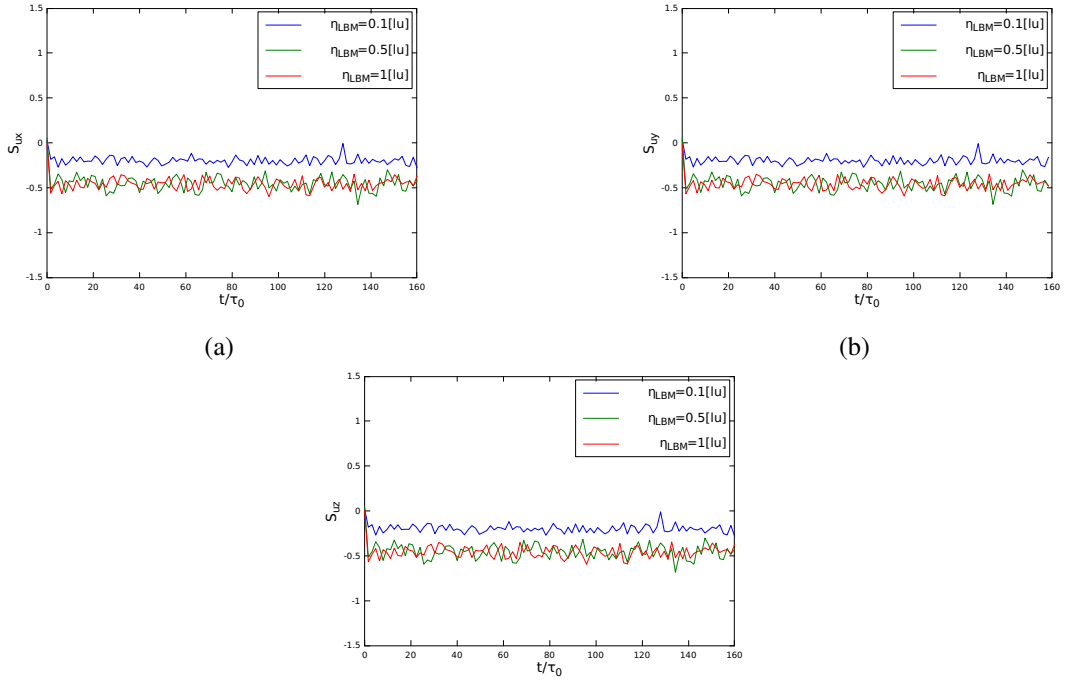

(a) (b)

(c)

Figure 2.13 – Time evolution of velocity derivative skewness for different Kolmogorov length scales: (a) $\eta = 0.1$[lu], (b) $\eta = 0.5$[lu] and (c) $\eta = 1$[lu], along three directions, here $t = t_{LBM}/\tau_0$.

Table 2.3 – Extracted global parameters from simulation results and relative errors.

Case	η	ϵ/ϵ_0	Error $(\%)$	$\epsilon_{\mathrm{cd}}/\epsilon_0$	Error $(\%)$	S_u
a	0.1	0.73	26.7	0.37	62.6	-0.14
b	0.5	1.1	10.7	0.79	21.3	-0.44
c	1	1.09	9.4	0.85	14.7	-0.48
d	2	1.07	6.7	0.9	9.9	-0.49

2.4.2 Distribution of energy in the flow

As turbulence spreads over a range of eddy sizes, it is frequently studied through the Fourier transform of the velocity fields. In Fourier space, the components of velocity for wave vector $\vec{\kappa}$ is given by:

$$\vec{u'}(\vec{\kappa}) = \frac{1}{(2\pi)^3} \iiint \vec{u'}(\vec{r})\, e^{-i\ \vec{\kappa}\cdot\vec{r}}\, \mathrm{d}^3 r \tag{2.45}$$

The kinetic energy (per unit mass) associated to the turbulent motions with this wave vector is denoted by E and is given by:

$$E(\vec{\kappa}) = \frac{1}{2}\vec{u'}(\vec{\kappa}) \cdot \vec{u'}(\vec{\kappa}) \tag{2.46}$$

In isotropic turbulence, there is no need to distinguish the contributions of each direction separately, so the contributions of all wave vectors of the same norm are considered all together, and another energy distribution is extracted as function of a scalar wave number, which is much easier to plot.

$$E(\kappa) = \iint\limits_{\|\vec{\kappa}\|=\kappa} E(\vec{\kappa})\, \mathrm{d}^2\kappa \tag{2.47}$$

Thus by plotting $E(\kappa)$ against κ, we can present an energy spectrum of the turbulent fluctuations, as shown in Figure 2.14.

The energy spectra confirm that increasing the Kolmogorov length scale makes the viscous dissipation occur at smaller wave numbers, that correspond to bigger eddy sizes. The spectra reveal that as turbulent Reynolds number increases the slope of the spectrum curves at low wave number tends to the $-5/3$ slope predicted by Kolmogorov's theory in the inertial subrange. Also as Reynolds number decreases, the viscous dissipation range tends to spread over all the simulated scales.

When the Kolmogorov length scale is smaller than the minimal value 0.318 [lu], the fluid motion at the smallest scales are not accurately resolved, as can be observed from the spurious behavior of the vorticity maps in the turbulent flow field as shown in Figure 2.15(a). Although the simulation reaches a stable solution, the flow field as observed in Figure 2.15(a) illustrates that the smallest eddies formed are physically unrealistic because the smallest Kolmogorov length scale formed during the simulation is 0.1 [lu], which is much smaller than 0.318 [lu].

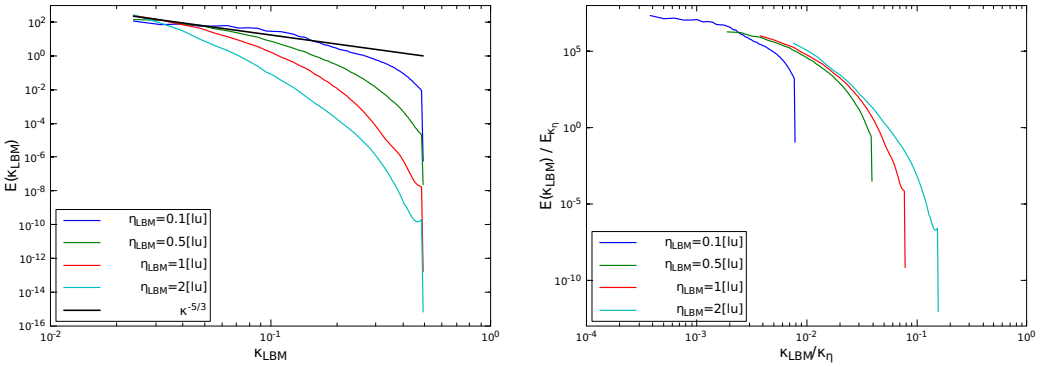

(a) (b)

Figure 2.14 – (a) Turbulent Energy spectrum, (b) Scaled Turbulent spectrum for $\eta = 0.1$[lu], $\eta = 0.5$[lu] ,$\eta = 1$[lu] and $\eta = 2$[lu] , where $E_{\kappa_\eta} = \epsilon_0^{2/3}\eta^{5/3}$, $\kappa_\eta = 2\pi/\eta$

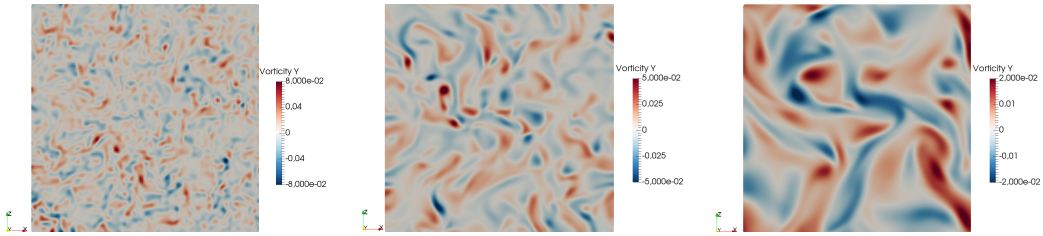

(a) (b) (c)

Figure 2.15 – Cross-sections of simulated flow field for different Kolmogorov length scales: (a) $\eta = 0.1$[lu], (b) $\eta = 0.5$[lu] and (c) $\eta = 1$[lu]. The color scales indicate the vorticity component (ω_y) normal to the plotted section.

As confirmed in the scaled turbulent spectrum (Figure 2.14(b)), simulations parameters must be chosen properly to develop an inertial energy subrange. The generation of inertial subrange improves with the increase of the ratio between the domain size to the Kolmogorov length scale.

2.4.3 Comparison with literature on linear forcing

As another validation step, a full comparison has been done between the simulations performed by using our implementation of linear forcing in our in-house code, and published results from the code developed by Valiño et al. [77] in pseudo-spectral (PS) space. Spectral forcing has proved a very useful tool to perform DNS in periodic domains, as previously discussed in section 2.1.5, where the direct application of the forcing in Fourier space yields very good computational performance. The conversion form simulations done in LBM units to values comparable with pseudo-spectral (PS) data with respect to space (ℓ), time (t) and

Table 2.4 – Simulation parameters

$\epsilon_{0\text{PS}}$	$\epsilon_{0\text{LBM}}$	ν_{PS}	ν_{LBM}	$L_{0\text{PS}}$	$L_{0\text{LBM}}$	η_{PS}	η_{LBM}
2.18	1.25×10^{-5}	0.025	0.025	1.26	25.6	0.05	1.05

mass (m) are done in the following way:

$$\ell_{\text{LBM}} = \ell_{\text{PS}} \frac{N}{2\pi} \tag{2.48}$$

$$t_{\text{LBM}} = t_{\text{PS}} \frac{N}{2\pi} \tag{2.49}$$

$$m_{\text{LBM}} = m_{\text{PS}} \left(\frac{N}{2\pi} \right)^3 \tag{2.50}$$

Here N denotes the size of the simulation domain as mentioned in section 2.3. As previously described, a constant dissipation rate is imposed in our linear forcing through the control parameter ϵ_0 from equation (2.17). The calculated value of dissipation rate at each simulation time step evolves towards this imposed value when reaching statistically steady state. The dissipation rate given by Valiño et al. [77] has been converted to LBM units using equation (2.34) and the kinematic viscosity has been taken the same for both LBM and PS units. Since the simulation is performed in pseudo-spectral space, the computational domain chosen in the simulation is cubical, with side 2π, and periodic boundary conditions are applied in all directions.

In the LBM, the first and last nodes serve as ghost nodes for the periodic conditions, so in order to simulate 128^3 nodes cubic box, the simulated domain size is $N_x \times N_y \times N_z = 130 \times 130 \times 130$. Comparisons have thus been made with PS simulations on similar 128^3 grids and the N value used in conversions is 128. The simulations conditions for our LBM and the PS simulation from Valiño et al. [77] are summarized in Table 2.4. The conversions between energy dissipation rates comes from the relation:

$$\epsilon_{\text{LBM}} = \epsilon_{\text{PS}} \left(\frac{\eta_{\text{PS}}}{\eta_{\text{LBM}}} \right)^4 \tag{2.51}$$

Comparisons between the parameters like dissipation rate, kinetic energy, integral length scale and Reynolds number have been conducted between the LBM and PS simulations. Time has been non-dimensionalized by the same characteristic time as before ($\tau_0 = u_0'^2/\epsilon_0$), and the initial condition in LBM simulations contain non-zero initial velocities so that linear forcing develops turbulence. Contrary to the initial condition, the flow thus evolves into a fully three dimensional flow that covers all length scales above Kolmogorov length and below the higher bound imposed by the size of the domain.

The values of the dissipation rate from LBM simulations (ϵ_{LBM}) are shown in Figure 2.16 and compared to the result from PS simulations (ϵ_{PS}). The same relative error is observed as in Figure 2.9 and is most probably explained by imprecisions in the calcula-

tion of dissipation rate from simulated data. The relative error between PS solution and the dissipation rate calculated using deformation rate from the LBM is 8%, while calculation using finite differences gives 15% error.

Since Reynolds number is dimensionless, its values remain the same in both PS and LBM units. The expression of Taylor's Reynolds number is given by Valiño et al. [77]:

$$Re_\lambda = \frac{u' \lambda}{\nu} \tag{2.52}$$

$$\lambda = \left(\frac{15\,\nu}{\epsilon_0}\right)^{1/2} u' \tag{2.53}$$

Here ϵ and u' (fluctuation velocity) are evaluated at each instant from the simulations. These parameters are calculated based on volume average.

Re_λ is evaluated using the control dissipation rate and the instantaneous value of fluctuation velocity (u') from which Taylor midscale (λ) is inferred. Taylor microscale is a characteristic length of turbulence that reflects the scale up to which viscosity significantly influences turbulent eddies and their dynamics. The Reynolds number calculated in this way fluctuates in the simulations due to the stochastic nature of turbulence. From Figure 2.17, it can be observed that Taylor's Reynolds numbers from LBM varies around a constant value that is in very good agreement with PS simulations. For the evolution of integral length scale (L), it is observed that it oscillates around a stationary value that is approximately 20% of the domain size. Here, the integral length scale (L) is calculated from fluctuation velocity (u') and dissipation rate (ϵ) at each time step as such:

$$L = \frac{u'^3}{\epsilon} \tag{2.54}$$

Figure 2.17 shows that L also reaches a constant mean value since the dissipation rate and the fluctuation velocity reach constant mean values. These oscillations around central

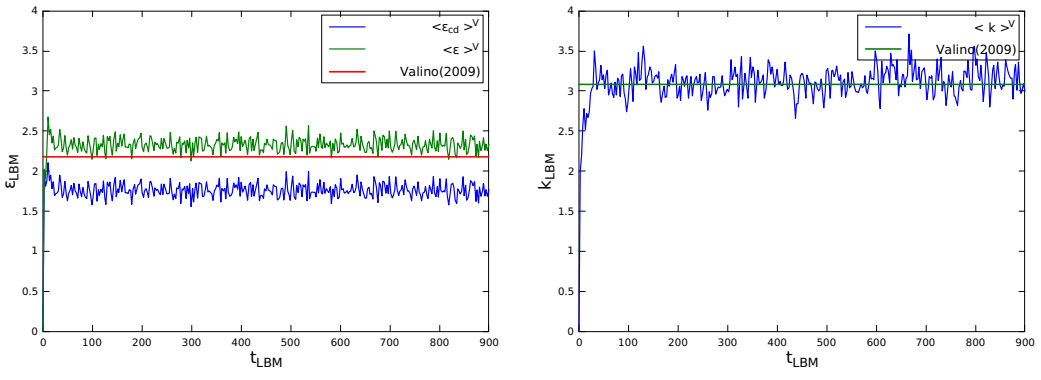

(a) (b)

Figure 2.16 – Evolution with respect to time of (a) turbulent dissipation rate ($\langle\epsilon_{\text{cd}}\rangle^V$ and $\langle\epsilon\rangle^V$) and (b) turbulent kinetic energy (k).

values have also been observed by Rosales and Meneveau [60]. The trends in the plots depict that, as initial conditions are not turbulent, characteristic turbulence parameters start with a zero value and increase until they attain the statistically steady state as turbulence develops due to linear forcing. It can thus be concluded that, regardless of the numerical procedure and type of forcing, the results obtained from our LBM are consistent with the literature.

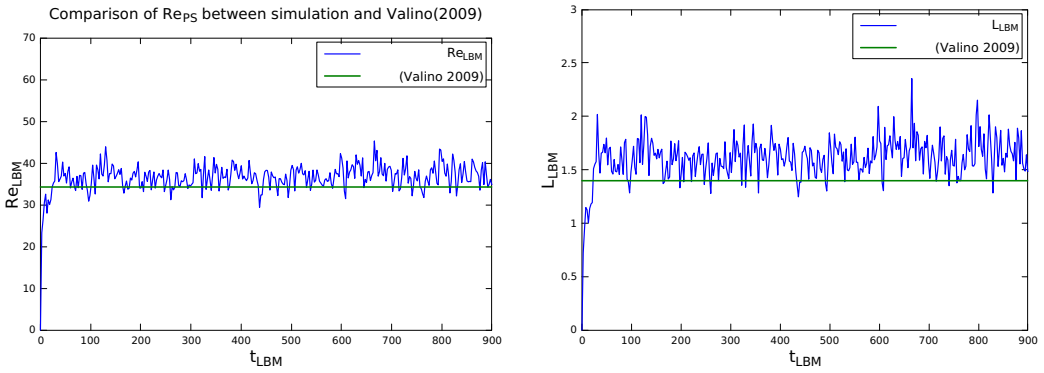

(a) (b)

Figure 2.17 – Evolution with time of (a) Taylor's Reynolds number (Re) and (b) integral length scale (L).

2.5 Conclusion on the method to create forced turbulence

This chapter clearly illustrated that the physical linear forcing scheme used for the production of homogeneous turbulence conditions could be combined with the lattice-Boltzmann scheme. The evaluated turbulent properties like the turbulent dissipation rate and the kinetic energy, achieve statistically stationary state, thus a proper turbulence flow field is obtained. Also the integral length scale reaches 20% of the domain size thus allowing a ratio between large and small scales that is large enough to represent the inertial subrange of the turbulence energy spectrum. Such spectra showed an accurate cascade of energy from larger scales to smaller scales that matches Kolmogorov's $-5/3$ slope. Unrealistic physical behavior were observed only when the flow was knowingly under-resolved (Kolmogorov length scale $\eta < 0.318\,[\text{lu}]$).

Also the section concerning validating our method by comparing our results with the ones from Valiño et al. [77] proved satisfactory and the turbulent properties seem to be in very good agreement with the literature results. It can thus be concluded that the linear forcing method used was satisfactory and that it can be further applied in the next chapter when fully developed DNS wall-bounded turbulence is simulated.

Chapter 3 : Simulation of the turbulent flow in a wall boundary layer

Contents

Wall bounded turbulence has been a major challenge for a long period of time. Large amount of energy is dissipated very close to the wall due to high values of local shears. Kim et al. [81] performed direct numerical simulations (DNS) of wall bounded turbulence and provided significant knowledge about the flow dynamics in such conditions and their mutliple scales. In parallel, many other studies in the past few decades have dealt with wall bounded turbulence with an experimental approach. Initially, authors like Robinson [82] or Nakagawa et al. [83] analysed only the viscous sub-layer in the vicinity of the wall, at relatively low Reynolds numbers. Österlund [84] was the first to perform experiments with much higher Reynolds number in the range of $2500 < Re_\theta < 27000$.

With the drastic improvements in computational power over the years, DNS of wall bounded turbulence has become more and more common, and numerical studies have investigated the dynamics in the turbulent region outside of the viscous sub-layer their interactions with the region close to the wall. Smits et al. [85] contributed statistical information on turbulence at higher Reynolds number. Hoyas and Jiménez [86] performed DNS in channel flow at $Re_h = 90000$ ($Re_\mathbf{T} = 2003$) and compared the results with those of Kim et al. [81] for $Re_\mathbf{T} = 180$. Schlatter and Örlü [87] performed DNS of a turbulent boundary layer covering an extended range of Reynolds numbers ($Re_\theta = 500$–4300). Their simulations all comprised the same physical flow conditions, but differed on the applied numerical method, resolution of grid, inflow generation method, boundary conditions and dimensions of simulation domain. Their results clearly showed that DNS is more accurate and reliable than corresponding experiments. The DNS helps in cases, when the boundary conditions can be denoted unambigiously as for instance in turbulent channel flow. They also showed that simulation with a longer domain in the streamwise direction provide more reliable results and predict different turbulent parameters more accurately.

- Re_h defines the Reynolds number of a channel flow, based on channel half width (h) and mean flow velocity along the center line (U_c), that is $Re_h = (U_c\, h)/\nu$;
- $Re_\mathbf{T}$ represents the Reynolds number based on friction velocity ($u_\mathbf{T}$) and channel half width (h), that is $Re_\mathbf{T} = (u_\mathbf{T}\, h)/\nu$, where friction velocity is derived from the mean wall shear stress ($\mathbf{T}_w$) and the fluid density (ρ) so that $\mathbf{T}_w = \rho\, u_\mathbf{T}^2$;
- Re_θ is the Reynolds number based on the momentum thickness[88], defined as $Re_\theta = (U_c\, \theta)/\nu$.

The multiple definitions for Reynolds numbers reflect the presence of multiple length and time scales that coexist in a wall bounded turbulent flow.

3.1 Mean flow and length scales

The inhomogeneous and anisotropic nature of turbulence is one of the most important characteristic features of wall-bounded turbulent flows. The wall shear stress and the molecular viscosity define a characteristic length scale that is usually considered to express distances to the wall in universal dimensionless way. This characteristic length, known as the “viscous

length", sometimes also called wall unit, is given by the expression:

$$\delta_\nu = \frac{\nu}{u_{\mathbf{T}}} \tag{3.1}$$

where ν and $u_{\mathbf{T}}$ are the kinematic viscosity and the friction velocity respectively. The friction velocity $(u_{\mathbf{T}})$ is expressed as $u_{\mathbf{T}} = \sqrt{\mathbf{T}_w/\rho}$. The dimensionless distance from the wall, scaled with viscous length is given by:

$$z^+ = \frac{z}{\delta_\nu} = \frac{u_{\mathbf{T}} z}{\nu} \tag{3.2}$$

The idea behind modelling boundary layers is to look for self-similar solutions along the streamwise direction (x) for the statistically steady flow properties, such as mean velocity. Such a self-similar solution could then be written in the following form, scaled by the friction velocity and the viscous length:

$$\frac{\mathrm{d}\bar{u}}{\mathrm{d}z} = \frac{u_{\mathbf{T}}}{z}\, \phi\left(\frac{z}{\delta_\nu}, \ \ldots\right) \tag{3.3}$$

where ϕ is a non-dimensional function, and the ellipsis is scaled with characteristic length scales of the flow far from the wall (such half channel width in a channel flow). Prandtl [45] in the year 1925 stated that, at high Reynolds number, the mean velocity profile close to the wall is completely determined by local viscous scales, thus:

$$\frac{\mathrm{d}\bar{u}}{\mathrm{d}z} = \frac{u_{\mathbf{T}}}{z}\, \phi\left(\frac{z}{\delta_\nu}\right) \tag{3.4}$$

Taking z^+ from equation (3.2) and defining u^+ as the dimensionless mean velocity, this yields:

$$u^+ = \frac{\bar{u}}{u_{\mathbf{T}}} \tag{3.5}$$

Equation (3.4) can then be written as:

$$\frac{\mathrm{d}u^+}{\mathrm{d}z^+} = \frac{1}{z^+}\, \phi(z^+) \tag{3.6}$$

Away from the wall, turbulence becomes prevalent compared to viscous dissipation which results in the disappearing of the dependency of equation (3.4) on viscosity, so that ϕ attains a constant value in the region of the flow close enough to the wall (in a thin sublayer dominated by viscous dissipation) to be scaled by its distance to the wall. This constant is noted as $1/\varkappa$ so that equation (3.6) becomes:

$$\frac{\mathrm{d}u^+}{\mathrm{d}z^+} = \frac{1}{\varkappa\, z^+} \tag{3.7}$$

So, very close to the wall, there is a thin sublayer where dissipation occurs through viscous shear, in which, since the shear stress does not vary much with distance to the wall, velocity increases linearly with distance from the wall. Outside of this sublayer, but remaining in a region still scaled by the distance to the wall, the velocity profile can be

obtained by integrating equation (3.7):

$$u^+ = \frac{1}{\varkappa} \ln z^+ + B \tag{3.8}$$

$\varkappa$ is called the Von-Karman constant [88] and its value is about 0.4. For a given flow, B is a constant value that is approximately 5.5 but it has been observed to vary depending on the flow geometry, pressure gradient, etc [89].

Figure 3.1 plots the mean velocity profile in wall bounded turbulence in a dimensionless form. Equation $u^+ = z^+$, depicts the viscous sublayer that holds for $z^+ \leq 5$. Above the viscous sublayer lies the buffer layer between $5 \leq z^+ \leq 30$. This is the region where wall induced turbulence reaches its maximum intensity. Further away from the wall, the flow evolves from wall bounded turbulence to free stream conditions where the influence of the wall condition becomes negligible. This is where equation (3.8) is applicable. This layer starts around $z^+ \approx 30$ and ends when the outer flow scales become prevalent, which varies with the flow geometry. In a channel flow at higher Reynolds number, the upper limit is usually reached around $150 < z^+ < 200$, as illustrated in Figure 3.1 [86]. The characteristic length scales are quite larger in the outer layers, where scaling is done based on the flow geometry. Townsend [90] provided a hypothesis that scales far away from the wall are independent on viscosity and wall roughness for high Reynolds number.

3.2 Elementary coherent structures

Although turbulent flows have complex and chaotic dynamics, they can be qualitatively described as combinations of elementary components, known as coherent structures, shaping the distribution of eddies and vortices. Coherent structures exist at all scales, so that very

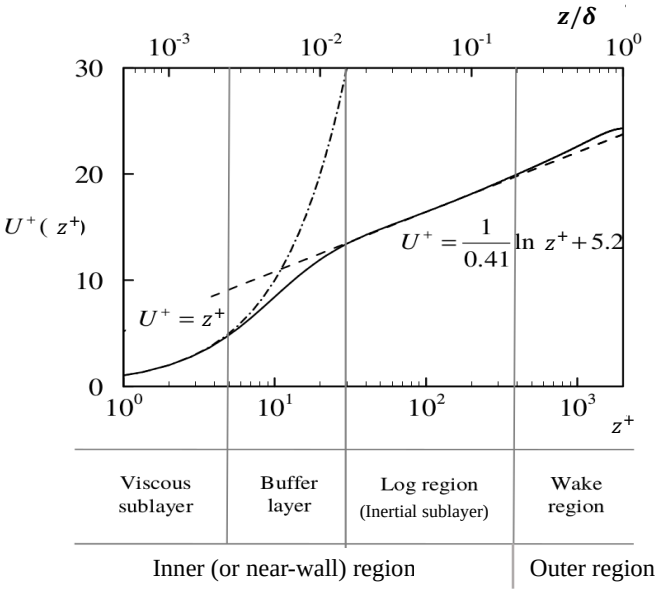

Figure 3.1 – Dimensionless mean velocity profile in a turbulent channel at $Re_{\mathbf{T}} = 20000$ [86]

large swirling structures characterize larger scales of the flow and break down into numerous elementary structures with coherent properties of their own.

Numerous observations have been published about the motion of coherent structures in wall bounded turbulent flows and such researches have proved helpful to represent complex turbulence as superimpositions of coordinated fundamental motions [91–95]. Early correlation data was found by measuring jets and turbulent wakes, particularly by Roshko [92]. The hydrogen bubble technique by Hama [96] to observe flow structures received wide spread attention and many researchers followed up including Kline et al. [91] who provided tentative explanations for the formation of low speed streaks due to vortex stretching and to large scale fluctuations acting on the flow close to a smooth wall because of stronger mean strain.

Previously, flow visualization methods using dyes had been used to study coherent structures in turbulent flows, but they could hardly be used to observe regions inside boundary layers. Moreover, fast smudging of colored regions hindered distinguishing complex dynamics in the flow. Concentration and fronts sharpness decreased with time due to dye diffusion. For this reason smoke type visualization techniques and hydrogen bubbles yielded clearer observations. In earlier days, experimental measurements approach were not sufficient to deal with complex turbulent flows, but recently, breakthrough has been made to observe coherent structures and their organization through simulation [97–99].

With improved understanding of coherent structures, it is now possible to discover and recognize many coherent structures in previous flow-visualization pictures collected of various turbulent flows taken decades ago. Computer simulations are now being the dominant tool for understanding and visualizing coherent flow structures. The ability to compute the necessary time-dependent Navier-Stokes equations produces graphic presentations with a greater level of details, allows visualization in several planes at once, and pushes the limits on sizes and speeds that could be measured in laboratory experiments [100].

3.2.1 Streaks, bursts, sweeps and ejections

Streaks are flow structures elongated along a streamwise direction. The are materialized by parallel bands stacked in the spanwise direction alternating higher and lower velocity. They are formed by eddies rotating around the streamwise direction, that carry low mean velocity fluid from the vicinity of the wall to the boundary layer and conversely, higher mean velocity fluid towards the wall. Because of the prevalent velocity component in the streamwise direction, shear induced swirling structures at the wall tend to elongate along that directions and form counterrotating eddies. Between two counterrotating eddies, at a given distance from the wall, the flow is thus slower when wall normal velocity moves away from the wall, and faster when wall normal velocity is towards the wall. Motion driving fluid away from the wall is called “ejection”, while its counterpart driving fluid towards the wall is called “sweep”.

Figure 3.2 shows streaks in a water flow which are displayed by air bubbles created by electrolysis at a distance from the wall $z^+ = 5$[101]. The scaling of such a distance was already detailed in equation (3.2). It corresponds to the location between the viscous sublayer and the buffer region.

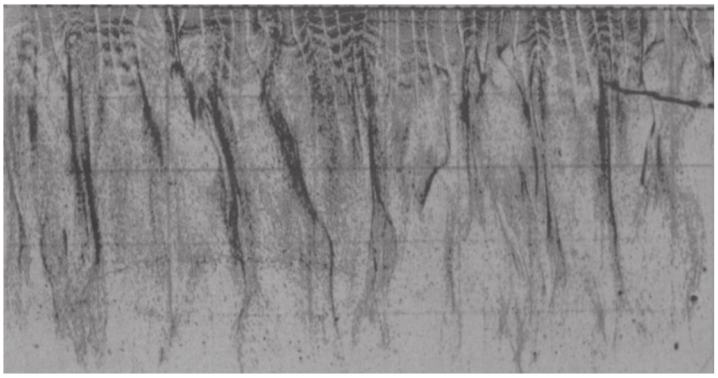

Figure 3.2 – Streaks at low speed where the flow is from top to bottom [101]

The streaky flow motion in wall bounded turbulence has been studied extensively during the last few decades [81, 101, 102]. These streaky structures have a characteristic spanwise spacing of ${\lambda_z}^+ \simeq 100$ and mean streamwise length of ${\lambda_x}^+ \simeq 1000$, as illustrated in Figure 3.3. The low velocity streaks flow with a phase speed of ${c_s}^+ \simeq 10$. Since they correspond to regions with a wall normal velocity oriented away from the wall, they are lifted from the wall. By getting further away from the wall, they become less stable and start oscillating, until their oscillations becomes too large and breaks the coherent structures, resulting in violent ejection of the fluid in the outward direction. The turbulence energy regeneration cycle includes formation of streaks, transient growth of streaks and eventually, breakdown of streaks when the perturbations become large [103].

Oscillations start to occur in part of the buffer region closer to the wall ($8 \leq z^+ \leq 12$) and grow stronger until breakage of these structures by the end of the buffer region ($10 \leq z^+ \leq 30$). During ejection, when they break, the fluid velocity in the stream wise direction is slower than average ($u' < 0$) but the wall normal velocity is relatively high ($w' > 0$), thus leading to positive Reynolds shear stress near the wall ($\sigma_{Re} = -\rho u' w' > 0$). The opposite phenomenon happens for the high velocity streaks that experience higher

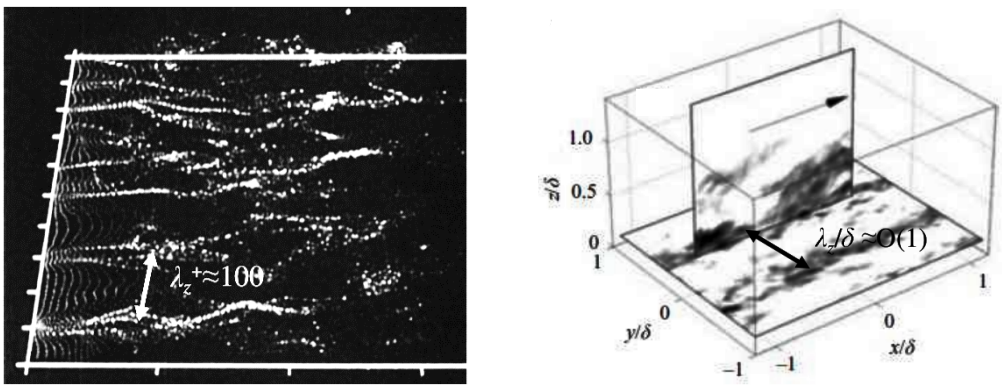

(a) (b)

Figure 3.3 – Structures of streaks in wall-bounded turbulence (a) tracing of particle near the wall [81]; (b) measurement by PIV in outer region [104]

streamwise velocity that average ($u' > 0$) and wall normal velocity oriented towards the wall ($w' < 0$), so that finally they also result in positive Reynolds shear stress ($u'w' < 0$). The order of magnitude of Reynolds stresses of both high and low velocity streaks is similar but their prevalence changes as distance increases from the wall which drives sweeping motion in the turbulent boundary layer.

3.2.2 Horseshoe and hairpin vortices

Horseshoe vortices are flow structures that arise from two mechanism. The first is transition from laminar to turbulent boundary layer that takes the form of a succession of instabilities, called Tollmien-Schlichting instabilities, that develop as waves in the boundary layer. The second mechanism is induced by turbulence that destabilizes the viscous flow in the boundary layer. Regardless of origin, horseshoe vortices appear when the linear flow profile destabilizes and starts rolling in the shear plane. Strong viscous diffusion is necessary to balance the rotational component of the shear at the wall, and the linear velocity profile is only stable very close to the wall. Many researchers during the 1950s and 1960s had performed analytical studies on this type of vortices. Theodorsen [105] gave descriptions of these vortical structures formed in the turbulent boundary layer. Their model described typical horseshoe vortices developing in the direction outward from the wall with heads inclined downstream at an angle of $45°$. Also the dimensions in spanwise direction were proportional to the distance of the vortices from the wall.

As shown in Figure 3.4, while growing away from the wall, these eddies destabilize and their vorticity center line bends giving the structure its horseshoe shape. It also results in different parts of the eddies being located in different places and thus being transported by the flow at different speeds, structures away from the wall moving faster. This elongates the horseshoe structures along the streamwise direction until they form the so-called streaks that were discussed in the previous section. This is why, while playing a prevalent role in shaping turbulence, horseshoes have a very short lifetime and are hardly visible in a fully developed boundary layer, where the wall is covered by their elongated results that are the streaks.

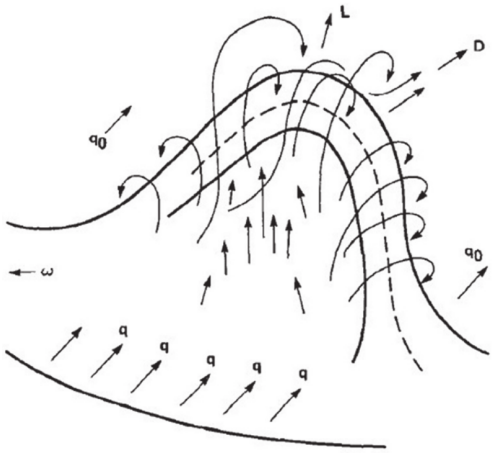

Figure 3.4 – Formation of a horseshoe vortical structure [106]

Figure 3.5 shows an elongated horseshoe vortical structure and its corresponding low velocity streak. The vorticity center line of the eddy is represented in orange and the streak is represented by the blue isosurface of low velocity. The bent blue arrows show the vorticity orientation, and the small red arrows the resulting wall normal motion (ejection at the streak and sweep outside of the horseshoe).

This momentum loss induced by the streak produces an elongated shear layer between the wall and the above part of the boundary layer. This shear destabilizes in a similar way as horseshoe structures at the wall and evolves into spanwise rings of vorticity, formed one by one thus producing several so-called hairpins close to the inviscid region. Helmholtz vorticity conservation keeps satisfied during this process so counterrotating eddies are also formed, but not shown in Figure 3.5. At the sides of the vortex legs, high speed zones are formed by sweeps bringing momentum from the inviscid region to the near wall region. This transfer of momentum and energy towards the wall produces high velocities in thin layers, that mean also an increase of the shear in such layers close to the wall. This is how energy is transferred from the large size vortices to small size vortices through multiple level sweeps, and dissipated at the wall.

Flow visualization by injecting smoke in the boundary layer [108] makes it possible to observe eddy structures such as hairpins. Figure 3.6 shows smoke visualization of a turbulent boundary layer in which the smoke fills the thin streaks in the lower part of buffer region close to the wall. Further away from the wall, the outer region is filled with intermittent smoke that is carried there by the ejection mechanism. Such intermittent smoke draws the outline of eddies, such as hairpins, formed between the buffer region and the inviscid region. The acronym “LSM” on the figure stands for “large scale motions” also called bulges, and corresponds to structures with a streamwise length of 2 to $3\,\delta$ and spanwise width of 1 to $1.5\,\delta$ [109, 110]. Here δ represents the boundary layer thickness. Smaller scales present in the large scale motion were depicted as “typical eddies” by Falco [111], and appear as “hairpins” on the figure by Adrian [112].

The highly coherent nature of these smaller eddies and their motion with regard to the fluid motion reveal the significant momentum transfer by Reynolds stress. It was also ob-

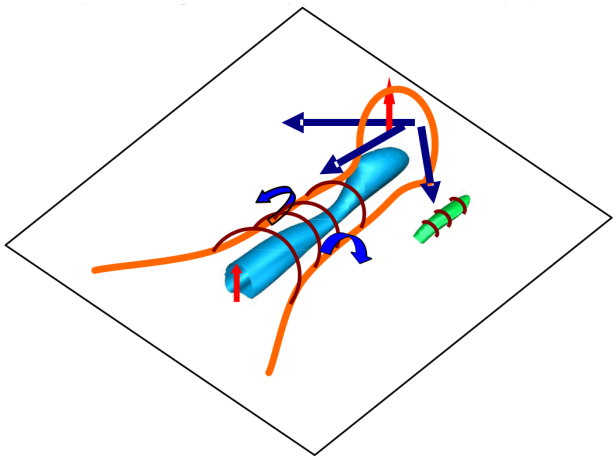

Figure 3.5 – Transfers of momentum in a horseshoe/streak turbulent structure [107].

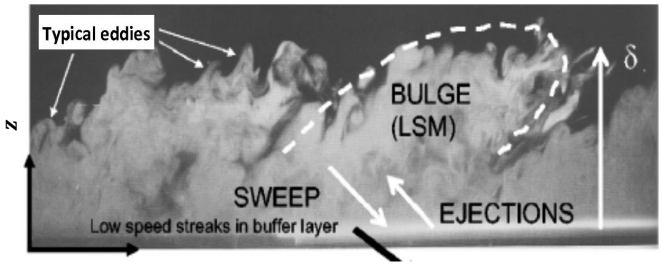

Figure 3.6 – Turbulence boundary layer visualization using smoke [112]

served that it is strongly dependent on Reynolds number. On the other hand, large scale motions are much less coherent. There is a big difference in size between the bulges and burst in sublayer and this difference increases with Reynolds number. There is also a difference in frequency: there are approximately twice as many bulges compared to sublayer bursts [111]. Lu and Willmarth [113] discussed the measurements of spatial scale and convection of the bursting structures. They demonstrated that nearly 40% of the Reynolds shear stress at distance $z/\delta = 0.823$ was carried by small scale motions of size approximately $\delta/10$ at $Re = 4230$ which generates huge intermittent contributions with a characteristic wavelength $\lambda_x^+ \simeq 10\delta$ in the streamwise direction [114].

The vorticity transport equation can be derived by calculating the rotational of the Navier-Stokes equation. Under the assumptions that the velocity gradient along wall normal direction ($\partial\bar{u}/\partial z$) is larger than other velocity derivatives, it yields a simple model for the vortex stretching with the following value:

$$\omega_x \omega_z \frac{\partial \bar{u}}{\partial z} \tag{3.9}$$

Equation (3.9) indicates that maximal vortex stretching will be obtained when the vorticity vector is oriented with an angle of $45°$ in the x-z plane, maximizing the product $\omega_x\omega_z$. Head and Bandyopadhyay [115] deducted that the orientation of the horseshoe vortices should be at that angle. Their research revealed the presence of the horseshoe vortices and quantified the extension of these in the boundary layer thickness, inclined at a constant angle with the wall. Figure 3.7 comes from their experiments that coupled hot wire measurements to evaluate the statistical nature of turbulence and smoke visualization performed by filling the entire boundary layer with smoke and then brightening it by a powerful plane of light.

Figure 3.7 shows a picture with a plane of light oriented longitudinally. It clearly reveals that at the aforementioned angle, large amount of smoke is present at relatively large Reynolds number at the edge of the layer. This further led the way to not only utilize the transverse light plane but to move this plane to an angle of $45°$ downstream and also $135°$ upstream to the wall surface. As represented in Figure 3.8, when the light plane is placed at $45°$ upstream, the vortex structure approaches the wall and similarly when the light plane is

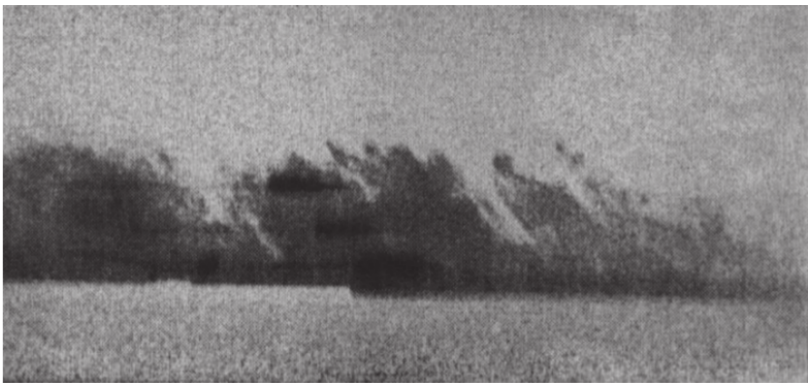

Figure 3.7 – Structure of boundary layer at $Re_\theta = 7500$ when flow is moving from left to right [115].

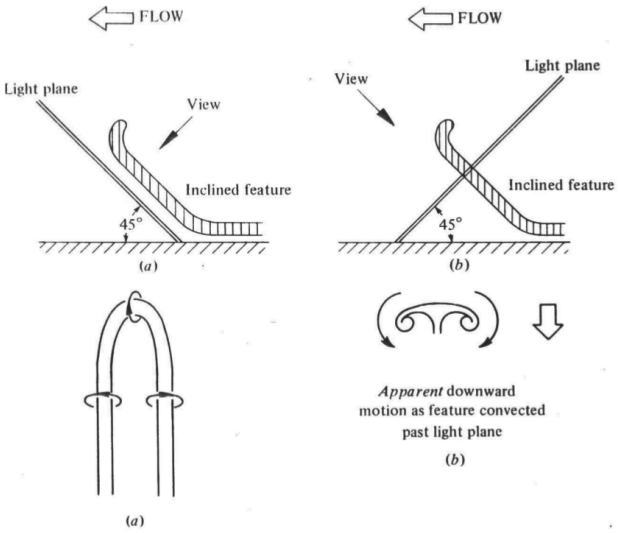

Figure 3.8 – Features of vortex structure when passed through light plane at angle (a) 45° upstream and (b) 45° downstream [115].

fixed at 45° downstream, hairpin or horseshoe type vortices appears for a short time. From this study it was concluded that hairpin vortices are the major constituents in a turbulent boundary layer at all Reynolds numbers.

The main objective of this chapter is to create fully developed 3D DNS wall bounded turbulence. From this literature review, several flow structures in a turbulent boundary layers have been identified and their characteristic scales estimated, which give information on how to setup simulations in order to capture them numerically.

3.3 Simulation setup

In the last few decades, lattice Boltzmann methods have emerged as an effective numerical technique of CFD. Although they introduce numerical compressibility due to their explicit scheme, they were first proposed to solve incompressible Navier-Stokes equations, imposing constrains on the time step (through a numerical Mach number, see section 2.2 in

Chapter 2).

Incompressible Navier-Stokes equations can be derived from moments of the Boltzmann equation, through Chapman-Enskog expansion [70] if density fluctuations remain negligible compared to the mean density value. Unfortunately it can be hard to control since density fluctuations are the way by which pressure is solved in LBM so it is impossible to maintain constant density practically without disturbing the flow solver.

This is why, after describing the simulation setup and parameters for the DNS of wall bounded turbulence, specific details are given on how spurious compressibility effects have been handled in the simulations (in section 3.3.3).

3.3.1 Flow geometry and simulation parameters

After having generated artificial turbulence in a fully periodic domain in Chapter 2, we now want to use the same method to generate turbulence as a boundary condition in a wall bounded flow.

3.3.1.1 Setup of a turbulent boundary layer

The simulation domain used for this work is divided into two regions. The top region is used for generating the artificial turbulence while the bottom region is used to study the wall bounded turbulent flow as described in Figure 3.9. The flow is periodic in the streamwise (x-direction) and the spanwise (y-direction) directions. The simulation domain which is used should be large enough to capture the larger scales of turbulence and also the coherent structures formed near the wall. Here, the driving of the flow is due to the constant shear stress imposed at the interface between the two regions. The artificial turbulence generates turbulent fluctuations produced in the top box which are then transported to the bottom box in the wall boundary layer. It is done to mimic the physical phenomenon occurring in the liquid metal ladle where turbulence is produced by the bubbles resulting from the injection of inert gas at the bottom of the ladle. Along the wall normal direction (z-direction) the bottommost z-plane is considered as no slip boundary condition while, at the topmost z-plane, a specific, so called “pseudo-periodic”, boundary condition has been implemented.

Finally, the boundary conditions are as summarized in Figure 3.9:

- wall (bounce-back) at the bottommost plane;
- periodicity in streamwise and spanwise directions;
- pseudo-periodic at the other side of forcing region (detailed in section 3.3.1.2);
- imposed shear stress between the homogeneous forced turbulence region and the wall bounded region.

To initiate the turbulence, so as to let the flow develop towards wall-bounded turbulence, one eddy with random orientation and magnitude was initially introduced per subdomain in the turbulence generation region. The boundary layer region was initialised by generating a logarithmic-law profile for the streamwise component of the velocity, and other components set to zero. This corresponds to the targeted velocity profile but with no fluctuation. Those

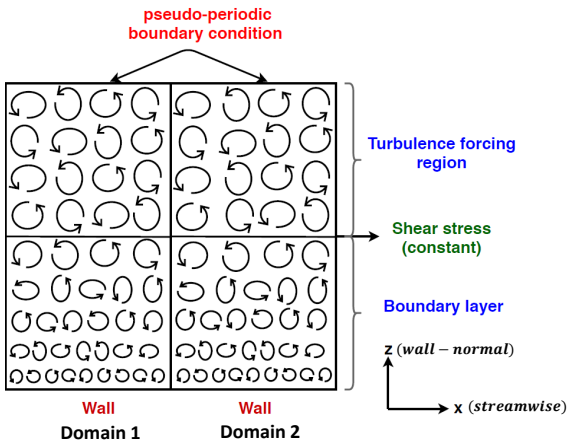

Figure 3.9 – Simulation setup with a turbulence forcing region and a wall bounded region, and application of constant stress at their interface.

log-law profile would be the result, when the simulation advances in time, from turbulence produced at the wall and in the forcing region.

Simulations were run long enough for turbulence to develop and reach statistically steady state. Also, to accelerate their evolution towards the targeted flow properties, when restarting simulations from no yet developed ones, the average ($\bar{u}$) and fluctuation (u') velocities were rescaled to their targeted values. This numerical trick was not used anymore once steady state was reached since once the logarithmic profile is achieved it remains the same as time goes on. Steady state was run long enough so that the result velocity profile would not be a reflection of the initially forced one.

Simulations at higher Reynolds numbers were run first, and used as initial conditions for lower Reynolds flows, so that lower Reynolds simulations start from developed turbulent conditions and reach steady state faster.

3.3.1.2 Periodic and pseudo-periodic boundary conditions

Periodic boundary condition and inter-subdomain communication are implemented in the same way. They correspond to an exact transfer of the properties of the flow (both in values and directions) from the last node of one subdomain to the first node of another subdomain. As shown in Figure 3.10(a), values and directions stored in A will be exactly the same in A'. Since the LBM is explicit, information just needs to be transferred between time steps.

On the other hand, a pseudo-periodic boundary condition is applied in the topmost boundary in the wall-normal direction, to help maintaining conservation of mass and momentum within the domain. Contrary to periodic conditions, the transfer of mass and momentum is done through surfaces that have the orientation in both subdomains, as shown in Figure 3.10(b) where communications are represented by the black arrows. The values stored in A will be similar as A' but their components along the normal direction are flipped.

When flow parameters like z-velocity, z-mean velocity and z-force are transferred between subdomains, the values are the same but with an opposite sign so that the fluid flow from one subdomain enters the other thus conserving mass and momentum. In terms of

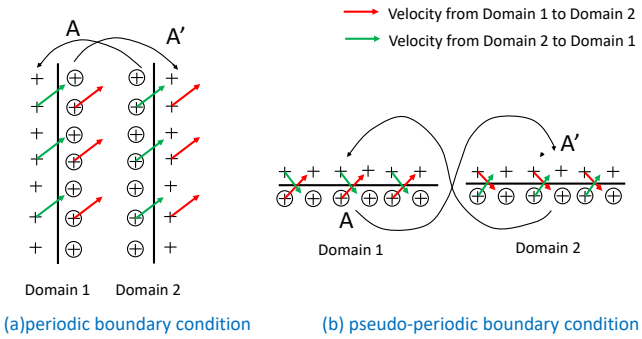

Figure 3.10 – Implementation of (a) periodic and (b) pseudo-periodic boundary conditions, red and green arrows represent velocity vectors in some nodes and how they are communicated to the image node.

LBM distributions (N_i), the value associated to a velocity (c_i) is transferred as the value associated to the symmetric vector in relation to the boundary plane:

$$N(\vec{c}_i, \vec{x}) \rightarrow N(\vec{c}_i', \vec{x}'), \qquad \vec{c}_i' = \vec{c}_i - 2(\vec{c}_i \cdot \vec{n})\,\vec{n} \tag{3.10}$$

where $\vec{n}$ is the unit normal vector to the boundary plane.

3.3.2 Domain decomposition and parallel resolution of the flow

In order to capture the broad spectrum of length scales in a wall boundary layer, from the smallest eddies that require a fine mesh to much larger scales that allow coherent structures to develop in a way that is not constrained by numerical issues, the number of necessary mesh cells (or lattice nodes) to resolve the whole problem can be very big, and thus require much more computation power than a single computation unit can provide. The computation load of wall bounded turbulence DNS must thus be distributed among many processors, each resolving a sub-part of the whole problem, sharing a common infrastructure that allows processors to communicate data between each others and to synchronize each others at given check-points in the resolution algorithms. Such an infrastructure is provided by a computation cluster, where many computation units are grouped in high bandwidth network. The simulations presented in this work were at first run on the Obelix cluster, owned by the Institut Jean Lamour, and later on Explor, the cluster of the Université de Lorraine [116].

To run over multiple processors, the simulation software that was used executes several parts of the algorithms in the different solvers at the same time, on different processors.

Parallelization of the code is done at two main levels. The first level is achieved between processors that have access to the same shared memory (RAM), using OpenMP directives [117]. After initialization of the problem to be simulated, the process forks into multiple execution threads and each execute only a part of the iterations in each loop. When calculations between the threads require results from calculations in another thread, all threads wait for each other and restart altogether when all the necessary calculations are finished.

Since all threads share the same memory, there is no need to make them communicate data explicitly (beside purging values cached by processors executing each thread).

However, the number of processors that share the same memory in the clusters where the simulations were run is still too low to run the DNS in a reasonable time. This is why a second level of parallelization is achieved using message passing, with the standardized so-called Message Passing Interface (MPI). The MPI implementation that was mostly used in this work is OpenMPI [118]. Such a parallelization is achieved by launching several processes at once, and providing communication channels between them — the latter part being the role of OpenMPI. Then all processes execute the same algorithms in parallel but work on different input data. The input data is set up so that each process resolves the physics of a smaller part of the whole problem. This was done by decomposing the total simulation domain in multiple subdomains and running a different process for each subdomain. Since all involved processes only see the data in their memory, the data they need to exchange is sent as messages (carried over the network by the MPI implementation) between them. An example of such data that must be exchanged are boundaries between subdomains, where the flow properties calculated in one process are boundary conditions for the flow computed in another process. The parallel performance of the parallelized code utilizing MPI can be evaluated by taking the ratio of the communication time to the computational time. The main criterion for maximizing the parallel performance lies in minimizing the time required for passing the messages between two processors.

In the end, simulations run in several processes that communicate through MPI, and each process forks into several execution threads that run on processors with shared memory access. Two types of simulation domain is used for performing wall bounded turbulence, smaller and larger domain as mentioned in Sections 3.4 and 3.5. For the smaller domain the total number of cores used is 32, where each subdomain is run on 16 cores. The computational time taken for the whole simulation to execute is nearly 72 hours. For the larger domain, the total number of cores is increases to 384 where each subdomain is launch on 32 cores and the total computational time is around 12 days.

3.3.3 Incompressibility of the flow and damping of pressure waves

Complex interactions between pressure waves produced by turbulence becomes a major factor in the production of spurious compressibility effects, especially in the case of linear forcing that tends to amplify such waves. He and Luo [119] provided a condition for compressibility effects to appear based on the comparison between the characteristic time of macroscopic changes in the flow and the time it takes the pressure waves to travel through the simulation domain ($\max(L_{\text{domain}})/c_s$, where $c_s = \sqrt{1/2}$, (see section 2.2 in Chapter 2). By ensuring that the macroscopic time is much greater than pressure wave propagation time, the propagation of pressure waves or density fluctuations can be considered as instantaneous in the flow field, hence making the temporal variation of pressure driven term negligible and reducing the magnitude of pressure and density variations. The criterion becomes all the more difficult to satisfy when the simulation domain gets bigger. Although developments to account for compressibility in a physical way with LBM have been discussed in the literature [120, 121], physical compressibility effects are non-existent in liquid metal flow in

a ladle. However, here, the macroscopic time is the integral time scale of turbulence, and, in order not to constrain the flow structures, a big simulation will be necessary, hence the criterion given by He and Luo [119] will not be satisfied. So, in our simulations, efforts were spent to reduce, even eliminate, the compressibility effects.

A pressure correction is applied on a layer that is 10 nodes thick along the wall-normal direction, situated in the middle of the turbulence production region in order to damp the pressure waves. It basically rescales the Boltzmann distributions (N) to relax density (defined as $\rho = \sum_j N_j$) towards a value that corresponds the reference pressure. In Eggels and Somers [1] LBM, pressure is governed by the following equation of state:

$$p = \frac{1}{2}\left(\rho\left(1 - \frac{u_i^2}{2}\right) - \rho_0\right) \tag{3.11}$$

So, to damp pressure waves, between two LBM time steps, the distributions are rescaled to:

$$N_j^{\text{corrected}} = (1 - A)\, N_j + A\, \frac{\rho_0}{\left(1 - \frac{u_i^2}{2}\right)}\, \frac{N_j}{\sum_j N_j} \tag{3.12}$$

where ρ_0 is the reference density (that is the one corresponding to $p = 0$ when $u = 0$, it is arbitrarily set to $\rho_0 = 8$ in simulations, following a recommendation by Eggels and Somers [1]), and A represents the relaxation coefficient, the value of which was chosen equal to or higher than the inverse eddy turnover time defined in Chapter 2.

3.3.4 Calculation of turbulence properties

Turbulence properties are not only useful for post-processing, they must also be evaluated from within the simulations, since they are used in the linear forcing calculation. In fully periodic simulations, turbulence was homogeneous, so statistics could be obtained from volume averages. Now, turbulence is not homogeneous, even in the forcing where it is close to homogeneous but not exactly because of its interaction with the boundary layer. Our tests with volume average calculations have shown that these tend to increase the unavoidable inhomogeneity of turbulence in the forcing region so, since they do not apply to non-homogeneous fields, volume averages are not suitable for the wall bounded configuration.

The fundamental averaging possibilities for the calculation of turbulence properties are the ensemble, volume and time average. In an isotropic homogeneous turbulence, due to the ergodic behavior, all these averages give the same result. Ensemble average is not doable in a single simulation, it would require running many instances of the same simulation with slightly different initial conditions. The computation requirements of such a solution make it impractical in DNS of turbulence. Unfortunately, random variables of interest in wall bounded flows are not statistically homogeneous, therefore time averaging is the only available solution:

$$\bar{C}(\vec{x}, t) = \frac{1}{T}\int_{t-\frac{T}{2}}^{t+\frac{T}{2}} C(\vec{x}, t')\, \mathrm{d}t' \tag{3.13}$$

where $C(x,t)$ denotes any parameter varying in space and time. Provided that T is longer than the integral time scale of turbulence ($T \gg \tau$), this should yield usable average values ($\bar{C}(\vec{x})$). However, such an expression cannot be implemented in the simulation, its evaluation at a given time (t) requires data from future times *i.e.* between t and $t+T/2$. Moreover, it requires storing all past calculated times between $t - T/2$ and t, which represents a huge amount of data. The time average in the simulations is defined in as a weighted average:

$$\bar{C}(\vec{x},t) = \frac{\displaystyle\int_0^t C(\vec{x},t') \, \exp\left(-\frac{t-t'}{T}\right) \, \mathrm{d}t'}{\displaystyle\int_0^t \exp\left(-\frac{t-t'}{T}\right) \, \mathrm{d}t'} \tag{3.14}$$

Such an expression is much easier to implement in discrete form between two LBM time steps:

$$\bar{C}^{(n)}(\vec{x}) = (1-A)\,\bar{C}^{(n-1)}(\vec{x}) + A\,C(\vec{x},t) \tag{3.15}$$

For wall-bounded turbulence simulation, in the calculation of velocity statistics, volume average from equations (2.39), (2.40), (2.41) in Chapter 2 is replaced by the time average operator from equation (3.15).

In equation (3.15), A is a coefficient that is scaled accordingly to the inverse eddy turnover time (τ). To get valid time averaged values for the turbulence, A should be taken lower than τ^{-1}, however since this time average is always late in time (it can only use the information from already calculated time steps), this would result in a pulsated flow due to the response time between the linear forcing imposed that way and the corresponding adjustment of average values. Values of A have thus been chosen larger than the value of inverse eddy turnover time, which yields statistically steady behaviour at the cost of slight variations of the calculated mean velocity with time, resulting in underestimating the magnitude of fluctuation velocities.

In the turbulence forcing region, the mean and fluctuation velocities are supposed to be statistically homogeneous. In order to improve the estimation of their values in spite of the too high value of A in equation (3.15), the calculation of mean velocity is smoothed in space and thus includes some kind of partial space average too. This partial volume averaging is introduced in the form of a diffusion equation. Henceforth the equation for mean velocity calculation becomes:

$$\bar{u}^{(n)} = \bar{u}_*^{(n)} + D\,\nabla^2\,\bar{u}_*^{(n)} \quad \text{with} \quad \bar{u}_*^{(n)} = (1-A)\,\bar{u}^{(n-1)} + A\,u_i \tag{3.16}$$

Here $\bar{u}_*^{(n)}$ is calculated based on the old mean velocity stored for the last time step. Diffusion coefficient D is only introduced in the forcing region, where the mean velocity is supposed to be constant. In the boundary layer, it is set to $D = 0$, but since there is no forcing there, a lower value for A can be used without destabilizing the statistically steady state. Second order centered finite-difference scheme is used to calculate the Laplacian operator (∇^2).

After evaluating the mean velocity, other parameters like fluctuation velocity, turbulent

dissipation rate and kinetic energy are evaluated using time averaging:

$$u' = u_i - \bar{u}^{(n)} \tag{3.17}$$

$$\bar{u'}^{(n)} = (1 - A)\,\bar{u'}^{(n-1)} + A\,u' \tag{3.18}$$

$$\bar{\epsilon}^{(n)} = (1 - A)\,\bar{\epsilon}^{(n-1)} + A\,(u'\,\nabla^2 u') \tag{3.19}$$

$$\bar{k}^{(n)} = (1 - A)\,\bar{k}^{(n-1)} + A\,\frac{u'^2}{2} \tag{3.20}$$

3.4 Simulations performed for smaller domain

The first set of simulations was performed with a smaller domain that was less prone developping spurious pressure waves (see section 3.3.3) in which everything but the pressure correction was implemented in order to simulate wall bounded turbulence. Another advantage of a smaller domain is that simulation can be run in a much shorter computation time, with the obvious counterpart that boundary conditions (especially imposed periodicities) may impact the physics of the simulated flow.

Noting δ the boundary layer thickness (that is the size of the non-forced bottom box), the simulation domain size was taken as $2\delta \times \delta \times 2\delta$ along the streamwise (x), spanwise (y) and wall normal (z) directions respectively. Using Message Passing Interface (MPI) domain decomposition (see section 3.3.2), the streamwise direction was divided equally into two $\delta \times \delta \times 2\delta$ subdomains. The total number of LBM fluid nodes was $N_x \times N_y \times N_z = 160 \times 80 \times 160$. LBM nodes were distributed equally among the two subdomains, so that each of these contained $N_x \times N_y \times N_z = 80 \times 80 \times 160$ nodes.

For this simulation, conversions between LBM parameters and physical parameters has been applied to air, as it will be the main application in Chapter 4 and the conversion is stated in Table 3.1. In the LBM simulation, a constant energy dissipation rate ($\epsilon_{0\,LBM}$) is imposed in the turbulence forcing region. Now, drive the flow, a constant shear stress ($\mathbf{T}_{0\,LBM}$) is applied in the form of local force along the streamwise direction at the plane interface between the two regions (forced and non-forced turbulence). The value for the time averaging coefficient (A) was taken as $10A_{0\,LBM}$ where A_0 is the inverse of the eddy turnover time from the turbulence forcing, that is $A_{0\,LBM} = (\epsilon_{0\,LBM}/27L_{0\,LBM}^2)^{1/3}$. The Kolmogorov length scale was set to $\eta_{LBM} \approx 0.32$.

Table 3.1 – LBM and physical parameters for wall bounded turbulence simulation in the smaller domain.

$\epsilon_{0\,LBM}$	$\epsilon_{0\,\text{phys}}$	$\nu_{0\,LBM}$	ν_f	$\mathbf{T}_{0\,LBM}$	$\mathbf{T}_w$
–	$\text{m}^2\ \text{s}^{-3}$	–	$\text{m}^2\ \text{s}^{-1}$	–	Pa
5×10^{-7}	280	1.75×10^{-3}	1.5×10^{-5}	3.3×10^{-3}	2.2

Figure 3.11 shows snapshots of the pressure and velocity fields after turbulence has fully developed. It presents the values of pressure and velocity magnitude in a plane normal to the spanwise direction, at the center of the domain. Since the streamwise component (x) of the velocity is the prevalent one, its magnitude also shows the boundary layer behaviour, with low velocities and lower turbulence at the wall, as opposed to higher velocity with stronger turbulence in the region away from the wall, where linear forcing is imposed and shear stress drives the flow.

Figure 3.12 depicts the evolution of the mean velocity along the wall normal direction, when fully developed turbulence is achieved. The calculated velocity profile (in blue) exhibits three expected features:

- in the vicinity of the wall, it matches a linear profile corresponding to the viscous sublayer (in red);
- in the forcing region (on the right hand side), it has a constant value, so that this region is not sheared and linear forcing can be applied to produce homogeneous isotropic turbulence;
- between the wall and the outer region, it matches the well-know logarithmic law of walls for a turbulent boundary layer (in green) [88].

The comparison between simulations and the law of wall, as seen in Figure 3.12, shows that the inertial sublayer is captured for distances from the wall $30 \leq z+ \leq 70$. Over 70, the increase in the mean velocity before attaining constant velocity profile in the turbulence production region can be explained by the fact that the forced turbulence is isotropic, and thus corresponds to turbulence far from the wall. By imposing its isotropy, it also imposes the transition from the inertial sublayer to the external region. The increase of velocity at the end of the inertial sublayer is a well observed trend from both experimental and numerical studies [122, 123]. Moreover, the turbulence intensity in the forcing region is greater that the one that would have developed in the flow due to the turbulence production

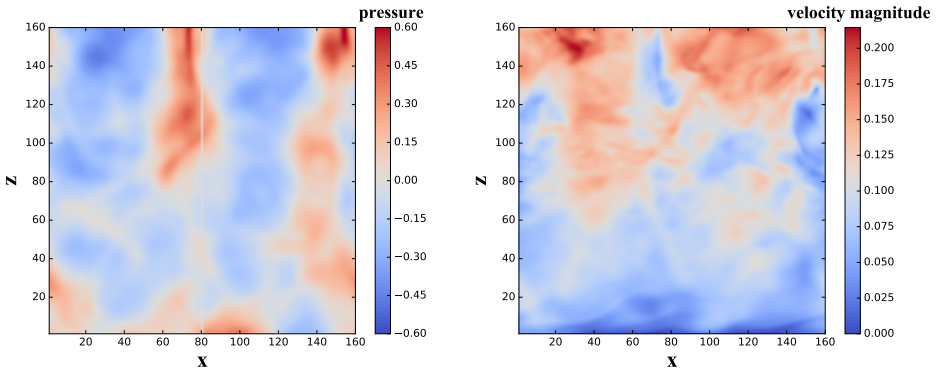

(a) (b)

Figure 3.11 – Color maps in spanwise normal plane of (a) pressure and (b) velocity magnitude for $\epsilon_{0\,\mathrm{phys}} = 280\,\mathrm{m^2 s^{-3}}$, $\mathbf{T}_\mathrm{w} = 2.2\,\mathrm{Pa}$ and $\nu_f = 1.5 \times 10^{-5}\,\mathrm{m^2 s^{-1}}$.

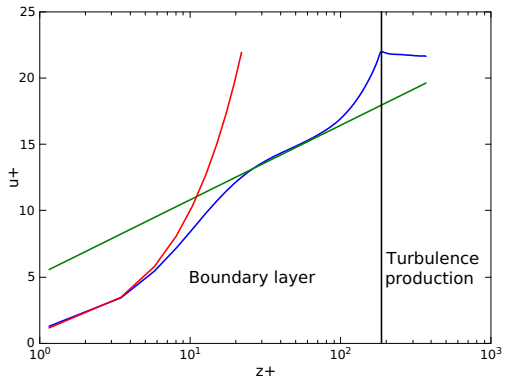

Figure 3.12 – Mean velocity profiles for the DNS simulation (blue) and comparison with traditional law of wall, $u^+ = z^+$ represents viscous sublayer(red line), $u^+ = 2.44\, ln\, y^+ + 5.5$ represents log-law turbulent profile.

at the wall. The simulated boundary layer presented here accounts for other sources of turbulence production. In a liquid metal ladle, that would be agitation provided by the bubbly flow far from the wall.

3.5 Simulations performed for larger domain

Although providing encouraging results, the DNS simulation performed previously in section 3.4 have run with a domain size that is too close to the expected size of the turbulent structures at the wall described in section 3.2.1. It means that periodicity imposed by the simulation boundary conditions probably constrains the turbulence properties at the wall. Even though the mean velocity profiles match fully developed turbulence at a wall, smaller structures may play a significant role in particle deposition, and must thus be captured properly. Average behaviour is not enough. This is why, simulations have been performed on a larger domain, in which pressure wave damping was applied according to the method described in section 3.3.3.

The larger simulation domain is sized as $6\delta \times 2\delta \times 2\delta$ along the streamwise (x), spanwise (y) and wall normal (z) directions respectively (δ is the boundary layer thickness, that is the height of the bottom box with no linear forcing). It corresponds to a total number of LBM nodes of $N_x \times N_y \times N_z = 720 \times 240 \times 240$ and in wall units ${N_x}^+ \times {N_y}^+ \times {N_z}^+ = 2520 \times 840 \times 840$ respectively. The simulation domain used is smaller in streamwise direction but larger in spanwise direction as compared to the simulation domain used by Bespalko et al. [124], who had a total number of LBM nodes of $N_x \times N_y \times N_z = 1080 \times 90 \times 182$. Moreover the domain we choose and the domain used by Bespalko et al. [124] is considerably smaller in the spanwise direction than the simulation of Moser et al. [125], who used dimensions of $4\pi\delta \times 4/3\pi\delta \times 2\delta$. A smaller simulation domain was applied in this work to reduce the computational cost of the simulation. This was chosen for our simulation because Jiménez and Moin [126] found the minimum dimensions for a channel flow are $\pi\delta \times 0.3\pi\delta \times 2\delta$ in streamwise, spanwise and wall normal directions, where he used $300 - 600$ and $80 - 160$ wall units along streamwise and spanwise directions. It can be concluded that the simulation

domain in our simulation is much larger than what was used by Jiménez and Moin [126].

The simulations ran in parallel with Message Passing Interface (MPI) by using domain decomposition: the streamwise (x) direction was divided equally into six parts of length $N_x = 120$ nodes, and the spanwise (y) direction was divided in two. Thus the entire simulation domain was divided into 12 subdomains as shown in Figure 3.13 and each subdomain is executed in one computational node consisting of 32 processors in EXPLOR supercomputer. Finally, each subdomain has the same number of fluid nodes $N_x \times N_y \times N_z = 120 \times 120 \times 240$. This corresponds to a grid resolution of $\Delta x^+ = \Delta y^+ = \Delta z^+ \approx 3.5$.

Each individual subdomain is also divided into two regions, where in the top region artificial turbulence is generated while in the bottom region, turbulent boundary layer is simulated. A constant shear stress value is imposed at the interface between the two regions which drives the flow. The pseudo-periodic boundary condition is applied in the topmost boundary condition in order to help keeping mass and momentum conserved within the domain. The transfer of mass and momentum is done between subdomains, as shown in Figure 3.14 where communications are represented by green arrows. As an example, mass and momentum that goes out through the top boundary condition in subdomain 2 is injected back in subdomain 5, and reciprocally from 5 to 2. Such a pseudo-periodic boundary condition preserves the periodicity over the 6 subdomains long period in the x-direction while ensuring that mass and momentum are not lost or gained through boundary conditions, but

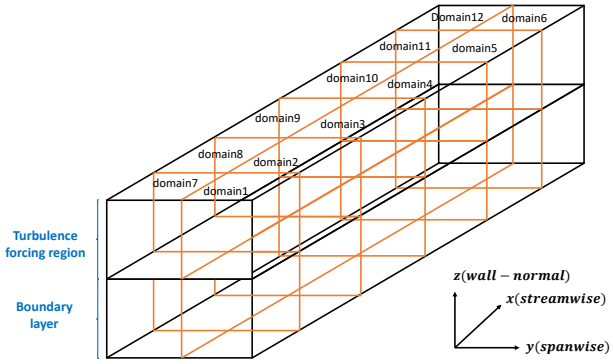

Figure 3.13 – Schematics of a simulation domain parallelized by domain decomposition.

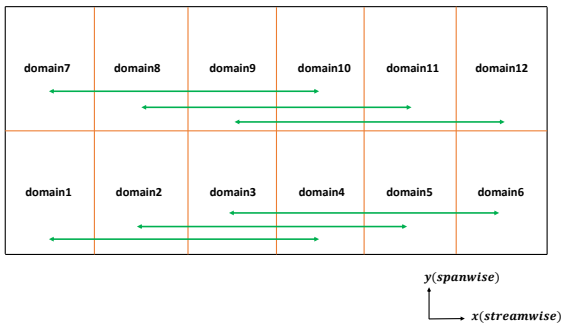

Figure 3.14 – Schematics showing how mass and momentum is transfer between states for pseudo-periodic boundary condition.

rather controlled by the imposed shear stress and linear forcing.

In this larger domain, simulations corresponding to various flow conditions have been run, to validate the simulations by comparing them to results from the literature. Also the friction Reynolds number (Re_T) used for the various flow conditions cases as mentioned in Sections 3.5.1,3.5.2,3.5.3 is taken to be around 180.

3.5.1 Simulations performed for larger domain without artificial turbulence

These simulations were performed for wall bounded turbulence without any forced turbulence away from the wall, in order to be comparable with channel flow simulations from the literature [125]. Turbulence develops only from wall shear, The simulation domain used in our simulations is the one described in section 3.5 and the flow is driven by a constant shear stress imposed in the plane centered in the wall-normal direction of the domain (that would be the interface with the forced region if there was forced turbulence) as mentioned in Table 3.2.

Such simulations take a rather long time to reach statistically stationary state since turbulence is slowly generated by the wall shear. Figure 3.15 shows the plot of dimensionless mean velocity and RMS of fluctuation velocity against time for the last $60\tau_0$ (or 32τ) of the DNS simulation, where τ is the eddy turnover time. From the plot it can be observed that when time starts from $120\tau_0$ till the end, both the properties tends to attain stationary value

Table 3.2 – LBM and physical parameters for wall bounded turbulence without artificial forcing simulation at constant density all over the domain.

$\nu_{0\,LBM}$	ν_f	$\mathbf{T}_{0\,LBM}$	$\mathbf{T}_w$
–	$\mathrm{m^2 s^{-1}}$	–	Pa
5×10^{-4}	1.5×10^{-5}	5×10^{-5}	3

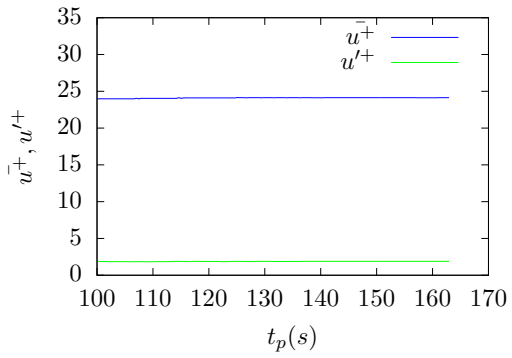

Figure 3.15 – Dimensionless Mean velocity and RMS of fluctuation velocity according to time (physical units).

thus achieving statistically stationary state.

The results are shown in Figure 3.16 which presents the plot of the mean velocity and fluctuation velocity profiles side by side. Both are compared with the DNS results of Moser et al. [125] and show very good agreement both in the viscous sublayer and in the log-law regions. This is an important observation since Moser et al. [125] simulated a channel flow that was driven by a pressure gradient, while our simulations are driven by shear stress. Our shear driven simulations have been modelled so in order to represent flow conditions at the wall of a ladle in which bubbles, far from the wall, promote turbulence and drive the flow due to their rise. It is noteworthy to observe that the wall bounded turbulence in shear driven and in pressure driven conditions have the same profile. It is not completely surprising though, since turbulence in both cases is generated by wall shear. The pressure gradient in a channel flow results in high shear stress at the wall. The shear stress in a pressure driven channel flow decreases linearly with the distance to the wall, but inside the boundary layer its variation is not significant enough to make a big difference with an imposed constant shear stress. It may explain the slight difference in the fluctuation velocity profiles though. Velocity fluctuations carry the shear stress in a turbulent flow (in the Reynolds stress tensor [88]), and the profile computed by Moser et al. [125] decreases a tiny bit steeper along the wall normal direction compared to ours. This may correspond to the decrease in shear stress along the wall direction in their simulations as opposed to our constant shear stress that yields a slightly flatter profile. The profiles are not different enough to support any strong conclusion about that.

Figure 3.17 shows the map and vectors of the dimensionless streamwise instantaneous velocity in the viscous sublayer region (in the plane $z^+ = 4$). The white lines between the squares show the domain decomposition used for parallelisation. From these figures, observation can be made that streamwise streaks of various sizes form close to the wall. The color map from blue to red represents the value of the streamwise component of velocity. Sub-figure (a) only shows the color map, and sub-figure (b) shows the velocity vectors. While such vectors are colored based on their x-component, their direction and magnitude

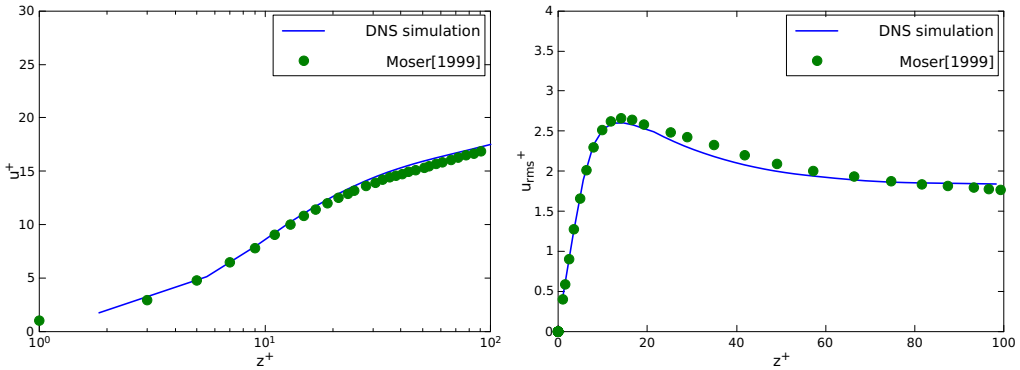

(a) (b)

Figure 3.16 – Profiles from this work's DNS (line) and comparison with Moser et al. [125] (points) for (a) mean velocity and (b) RMS of fluctuation velocity.

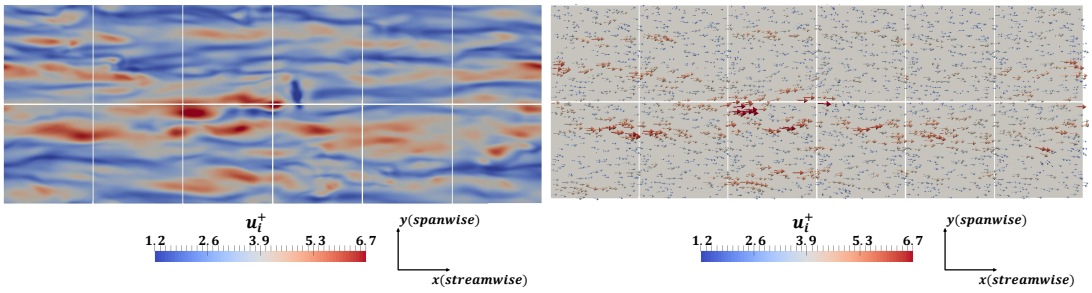

(a) (b)

Figure 3.17 – Instantaneous velocity field in the plane $z^+ = 4$ from DNS without turbulence forcing as (a) color map of its streamwise component and (b) vector field.

gives more information on the actual flow and streak structures. It is clear from Figure 3.17 that the streak sizes in both spanwise and streamwise directions are small enough compared to the domain size so that the imposed periodicity of the simulation will not impact their properties. Also, these streak patterns are consistent with the structures observed in previous DNS simulations of turbulent channel flow [127].

Figure 3.18 draws the isocontours of the second invariant of the symmetric part of the gradient of the strain rate (q), which makes visible the formation of low and high intensity streaks. The expression for strain of this scalar value is given by:

$$q = \frac{\partial^2 u}{\partial x^2}\frac{\partial^2 v}{\partial y^2} + \frac{\partial^2 u}{\partial x^2}\frac{\partial^2 w}{\partial z^2} + \frac{\partial^2 v}{\partial y^2}\frac{\partial^2 w}{\partial z^2} - \frac{1}{4}\left(\frac{\partial^2 u}{\partial x\,\partial y} + \frac{\partial^2 v}{\partial x\,\partial y}\right)^2 - \frac{1}{4}\left(\frac{\partial^2 u}{\partial x\,\partial z} + \frac{\partial^2 w}{\partial x\,\partial z}\right)^2 - \frac{1}{4}\left(\frac{\partial^2 v}{\partial y\,\partial z} + \frac{\partial^2 w}{\partial y\,\partial z}\right)^2 \quad (3.21)$$

The discontinuities in Figure 3.18 are due to nodes where space derivatives are not calculated during the post-processing in Paraview, that is across subdomains. Such blank lines thus illustrate the domain decomposition used for parallelizing the computation.

Figure 3.19 shows the second invariant of velocity gradient tensor, which illustrates the formation of streaks in the fully developed wall bounded turbulence when there is no forcing. The region where the isocontours are visualized consists of strong vorticity. Close to the wall, streamwise vortices and horseshoe patterns can be observed stretching in the streamwise direction in the way described in section 3.2.2. Second invariant of velocity gradient tensor (Q) is defined by the expression:

$$Q = -\frac{1}{2}\nabla\vec{u} : \nabla\vec{u} = \frac{1}{4}\left(\vec{\Omega}\cdot\vec{\Omega} - 2S : S\right) \quad (3.22)$$

where the velocity gradient is decomposed in its rotational (Ω) and symmetrical (S) parts: $\nabla\vec{u} = S + \Omega$. S and Ω respectively denote the strain rate and rotation rate tensors. In equation (3.22), $\vec{\Omega}$ is the dual vector the rotation tensor Ω. The strain rate and rotation rate

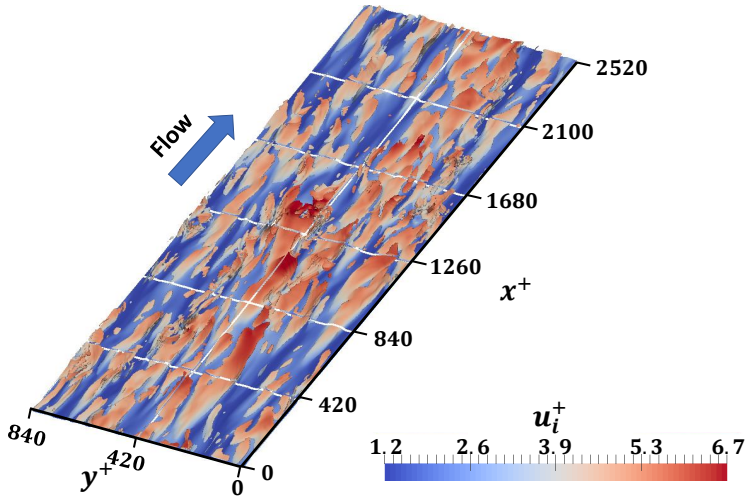

(a)

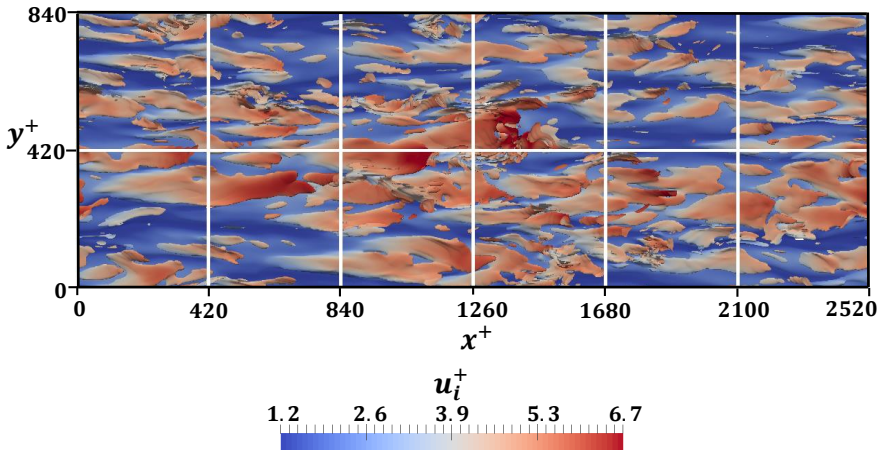

(b)

Figure 3.18 – Isocontour of q from equation (3.21) colored by instantaneous streamwise velocity component in the viscous sublayer region with no turbulence forcing: (a) 3D view and (b) top view, $q^+ = 0.00085$.

are defined as:

$$S_{ij} = -\frac{1}{2}\left(\frac{\partial u_i}{\partial x_j} + \frac{\partial u_j}{\partial x_i}\right), \quad \Omega_{ij} = -\frac{1}{2}\left(\frac{\partial u_i}{\partial x_j} - \frac{\partial u_j}{\partial x_i}\right) \tag{3.23}$$

Figure 3.20 was plotted using the *Line Integral Convolution* (LIC) plugin for *Paraview* visualization software[1]. The color scale (from blue to red) shows the streamwise velocity component, while the shading (light and dark streaks) represents streamlines of the projected velocity field in the plane normal to the streamwise direction (y-z). That is, the horizontal width of these figures is the spanwise direction (y) and their height is the wall normal direction (z), with the wall at bottom made visible by the blue low velocity region, and the end of the boundary layer at the top. The shading done by the LIC plugin draws lines

[1] https://www.paraview.org/Wiki/ParaView/Line_Integral_Convolution

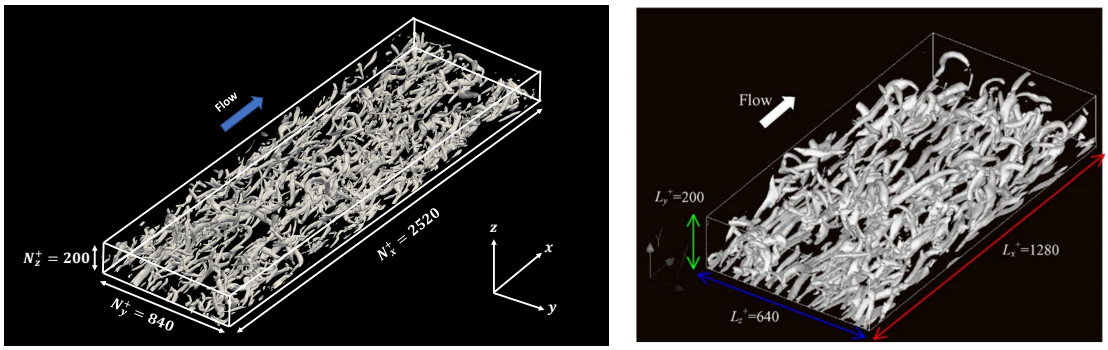

(a) (b)

Figure 3.19 – Isocontour of second invariant of velocity gradient tensor, $Q^+ = 0.028$ (a) with no turbulence forcing and (b) for open channel flow from Yamamoto et al. [128].

that are tangent to the 2D velocity field (y and z components) but the gray value does not hold any specific meaning. The LIC was calculated in each subdomain separately, which is why some appear darker than others, but there is no discontinuity at the interface between subdomains, contrary to what LIC lighting misleadingly suggests.

All in all Figure 3.20 gives information on both the streamwise velocity (through color) and the other velocity components (through streamlines) which gives an idea of the full 3D velocity profiles in different planes at various locations along the streamwise direction. Smaller eddies at the wall, swirling around the streamwise direction, due to geometrical constraints imposed by the wall can clearly be seen. They correspond to the streaks discussed in section 3.2.1. The eddies clearly scale with the distance to the wall. Both the smallest and the biggest eddies at a given wall distance increase in size when the distance increases. Also, many eddies are easy to distinguish because their swirling axis is normal to the y-z planes, so they appear as sets concentric closed curves. This is because of the wall impact on turbulent structures. At the wall, shear creates eddies swirling around a spanwise oriented axis that structure as streaks in the streamwise direction when they elongate. In the end, many rotating structures close to the wall have their axis either along the spanwise or the streamwise direction, and this anisotropy remains when they develop in regions farther from the wall. A quite different behaviour can be expected when isotropic turbulence is forced from the outer region of the boundary layer.

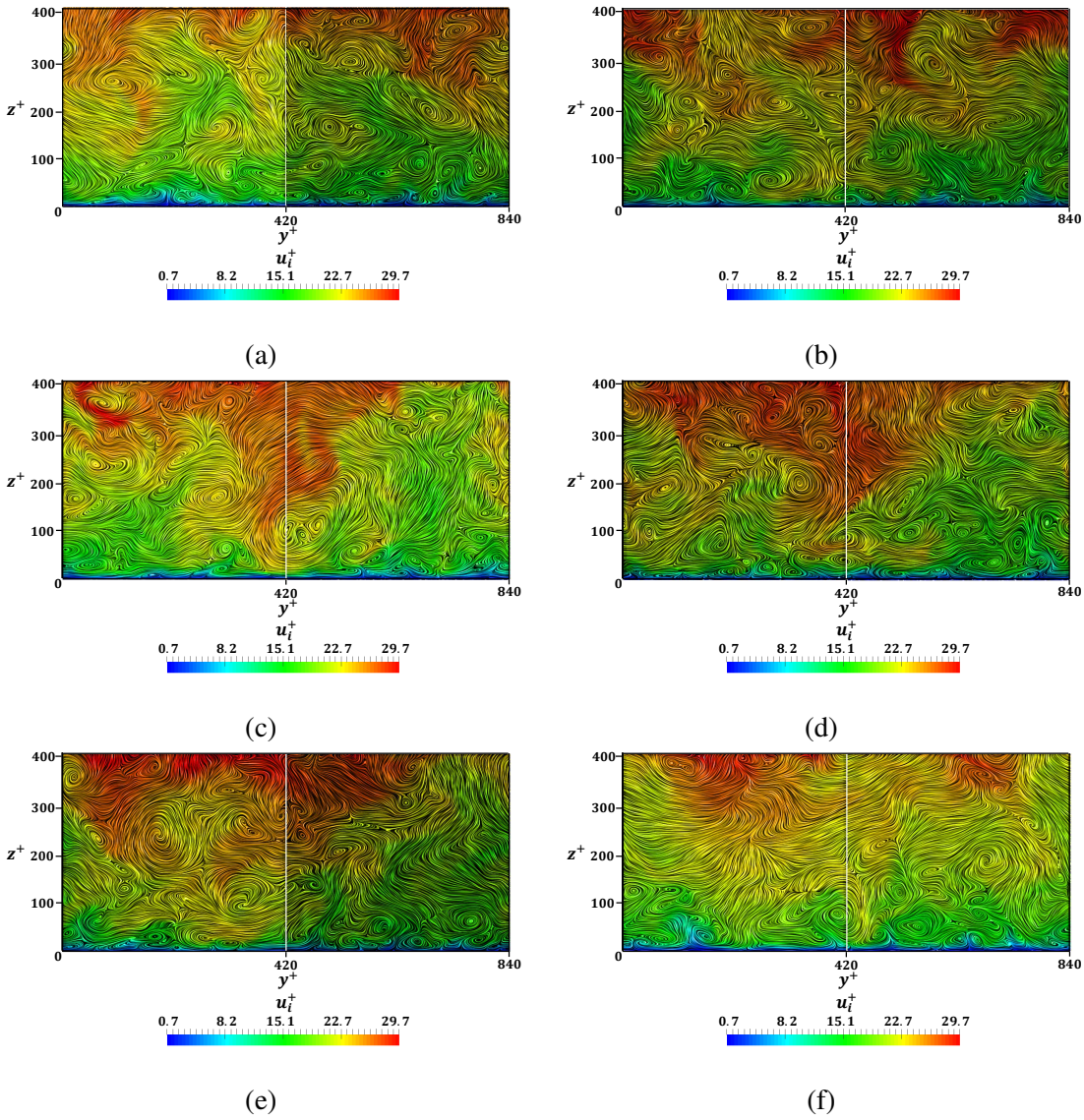

Figure 3.20 – Streamwise velocity maps ($u_i{}^+$) in various cross-sections at (a) $x^+ = 195.5$, (b) $x^+ = 580.2$, (c) $x^+ = 964.9$, (d) $x^+ = 1349.7$, (e) $x^+ = 1734.45$ and (f) $x^+ = 2112.7$ when no turbulence forcing is applied.

3.5.2 Simulations performed for larger domain with artificial turbulence at turbulent intensity 20%

Section 3.5.1 revealed that results of DNS wall bounded turbulence with turbulence forced in the external region are compared well with the literature results for a channel flow. Now, a similar is considered in which turbulence forcing is added. Since in a metallurgical reactor turbulence generated by the bubbles in the core of the ladle diffuses towards the walls, turbulence is generated in the top box of the simulation domain to mimic such conditions. Diffusion and convection by large eddies transport the generated turbulence to the bottom box where the wall boundary layer is studied.

In such simulations, turbulence has two origins: (a) shear induced turbulence at the

Table 3.3 – LBM and physical parameters for wall bounded turbulence with artificial forcing at turbulent intensity of 20%.

$\epsilon_{0\,LBM}$	$\epsilon_{0\,\text{phys}}$	$\nu_{0\,LBM}$	ν_f	$\mathbf{T}_{0\,LBM}$	$\mathbf{T}_w$
–	m^2s^{-3}	–	m^2s^{-1}	–	Pa
5×10^{-8}	590	5×10^{-4}	1.5×10^{-5}	5×10^{-5}	3

wall and (b) artificial isotropic turbulence due to linear forcing in the top box. Hence, the results obtained for the profile plots and velocity maps are different from those obtained in channel flow (see section 3.5.1). The simulation domain was the same as mentioned in section 3.5 and a constant shear stress was applied. The control parameter (ϵ_0) for the energy dissipation rate in the forcing region was set as reported in Table 3.3.

The turbulence intensity (I_{turb}) is defined as the ratio between the RMS of the fluctuation velocity (u') to the mean velocity outside of the boundary layer ($\bar{u}_\infty$):

$$I_{\text{turb}} = \frac{u'_{RMS}}{\bar{u}_\infty} \tag{3.24}$$

Figure 3.21 presents the evolution of the mean velocity and the RMS of fluctuation velocity with distance from the wall. The mean velocity profile appears to be in perfectly good agreement with the viscous sublayer profile ($u^+ = z^+$) and the turbulent log-law profile ($u^+ = 2.44 \ln z^+ + 5.5$). The mean velocity perfectly coincides with the log law profile from $z^+ = 30$ to $z^+ = 150$, which are commonly observed values for inertial sublayer [88], meaning that in this simulation the transition from inertial sublayer to external flow is not due to the isotropic forced turbulence, but rather corresponds to the natural transition between the two regions (see the discussion of Figure 3.12 in section 3.4). The increase of velocity at the end of the inertial region is still there, as expected, but is less pronounced than in the more confined domain.

The curves for fluctuation velocities presented in Figure 3.21 need to be explained. Indeed, they show a strange behaviour at interface between the boundary layer and the forced region. To understand this behaviour, one must go back to the way average calculations are done from equations (3.15) and (3.18). To avoid pulsating flow induced by linear forcing, the time averages in the forcing region are calculated over limited period of time. This was discussed in section 3.3.4 and one of the consequences of such calculations is that the RMS of the fluctuation velocities are underestimated during the simulation, which means that the turbulence production in the top box is actually greater that the one set through the control parameter of linear forcing. Outside of the forcing region, there is no need to limit the averaging period, so a much longer one was used in the bottom box, ensuring that turbulence properties in the region of interest are calculated properly. This is why there seems to be a jump in fluctuation velocity at the interface between the two boxes. In the region close to the wall, it is calculated accurately but it is underestimated in the forcing region. The

amount of underestimation can even be read from Figure 3.21, where it corresponds to the magnitude of the steep jump at the interface. The actual curve with no discrepancy due to the averaging method would be continuous throughout the whole domain as shown by the green curve in Figure 3.21(b). The RMS of fluctuation velocity evaluated by taking the volume average over the whole turbulence production region is larger than the one calculated by the time average in the turbulence forcing scheme (which matches the control value). A corrected curve is obtained by adding the difference between volume based calculation and the control value to the RMS profile in the forcing region. Such a corrected profile appears to be smooth, which confirms that time and volume average yield similar values as long as the averaging period is long enough.

In the end, it means that the turbulence generated in the top box is stronger than the one set through the controlled energy dissipation rate (ϵ_0). In this simulations targeted at 20% intensity, it results in an actual intensity around 23.247%. This value is calculated from equation (3.24), using volume averages in the forcing region for both calculations of the mean velocity and the RMS of the fluctuations. Beside that, homogeneous isotropic turbulence is created in the forcing region and travels in the wall boundary layer as expected. As indicated by the profile of fluctuation velocity, after a steep increase close to the wall, it attains a plateau in the boundary layer and later increases again till it reaches the turbulence production region where it is constant.

Now, such a combined wall shear induced and forced turbulence can be compared to turbulence in channel flow. Figure 3.22 represents the comparison of our DNS with that of Moser et al. [125] that was already used as a comparison case in section 3.5.1 (for $z^+ < 100$). The mean velocity profiles perfectly match. That is, turbulent flow with fairly different properties end up showing the same mean flow, which is a strong warning that mean flow must not be considered alone for validation. The fluctuation velocity profiles obviously differ significantly away from the wall. While fluctuations decrease with the distance to the wall in the channel flow case, they reach a plateau in our forced turbulence. However, they match surprisingly well for $z^+ \leq 20$, which means that turbulence in the

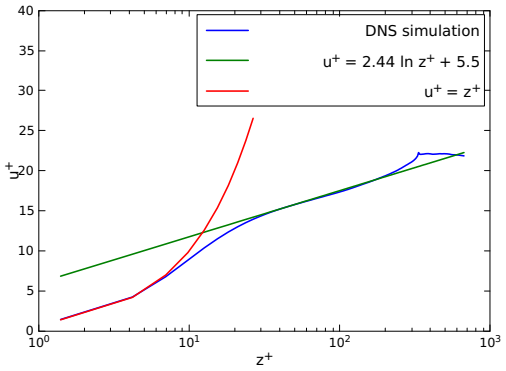

(a) Mean velocity from DNS (blue) and comparison with law of wall in the viscous sublayer (red) and with the logarithmic profile (green)

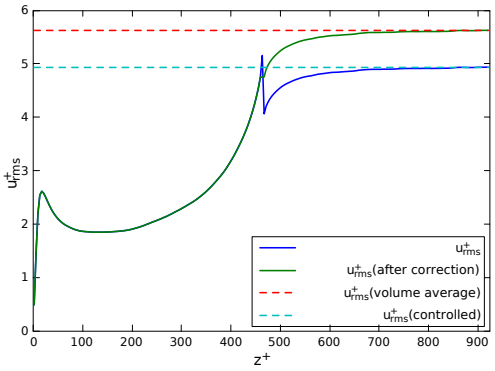

(b) Fluctuation velocity from the DNS simulation: time based RMS (blue) and corrected curve (green)

Figure 3.21 – Velocity profiles along the wall-normal direction from simulation performed at $\gtrapprox 20\%$ turbulent intensity.

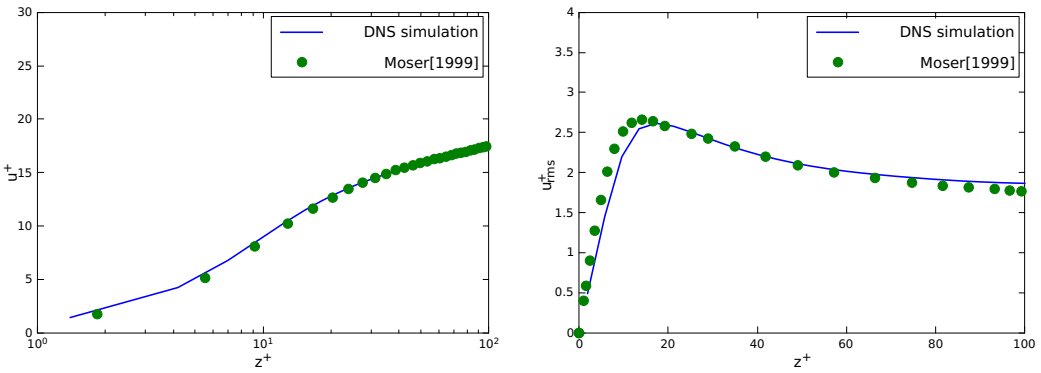

(a) (b)

Figure 3.22 – Profiles at turbulent intensity $\gtrapprox 20\%$ from this work's DNS (line) and comparison with Moser et al. [125] (points) for (a) mean velocity and (b) RMS of fluctuation velocity.

sublayer is very similar in both cases. This is explained by the role of the wall in this region that prevails over the difference in the far field between the two simulations, and this means that the smaller turbulent structures at the wall have a very low sensitivity to turbulence in the external region.

Figure 3.23 presents a color map of the streamwise component of the velocity in the plane $z^+ = 4$ as well as velocity vectors in the same plane, in the viscous sublayer. Streaks form similarly to what has been observed in the literature on channel flows [81, 98] and in our simulations without forced turbulence. This is confirmed by the isocontour from Figure 3.24 that looks very similar to the one in channel flow from Figure 3.18. Also the second invariant of velocity gradient shown in Figure 3.25 looks very much comparable to the one in Figure 3.19 with the same visualization of streaks and horseshoe structures close to the wall.

Figure 3.26 shows small eddies at the wall, swirling around the streamwise direction

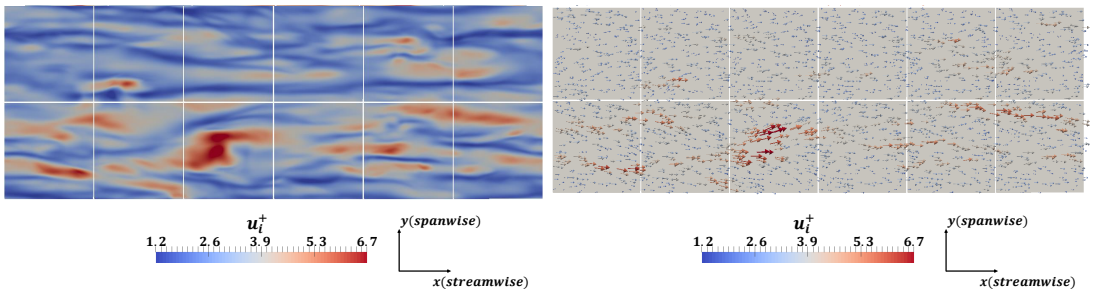

(a) (b)

Figure 3.23 – Instantaneous velocity field in the plane $z^+ = 4$ from DNS with turbulence intensity $\gtrapprox 20\%$ as (a) color map of its streamwise component and (b) vector field.

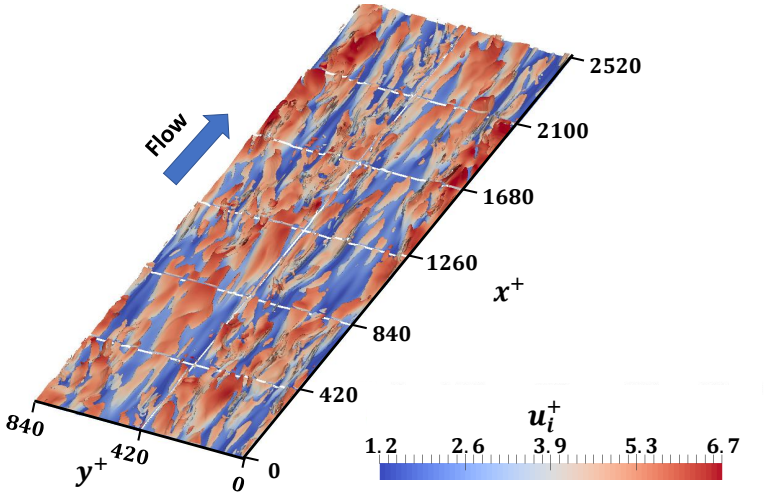

(a)

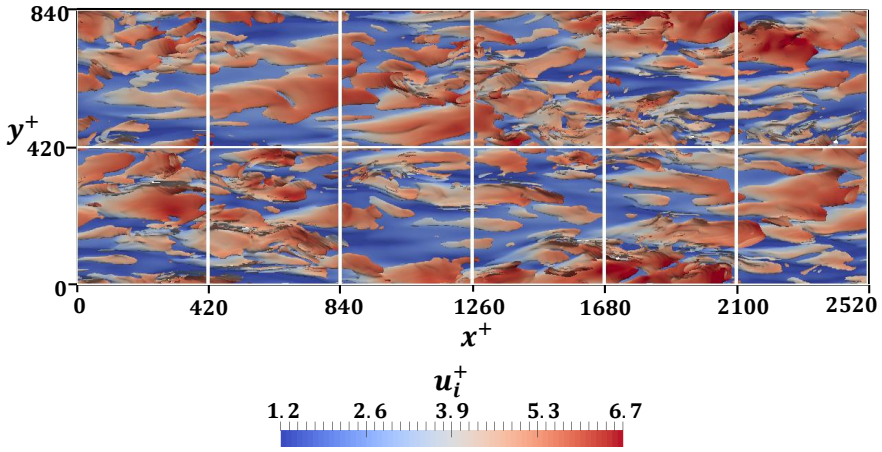

(b)

Figure 3.24 – Isocontour of q from equation (3.21) colored by instantaneous streamwise velocity component in the viscous sublayer region at turbulent intensity $\gtrapprox$ 20%: (a) 3D view and (b) top view, $q^+ = 0.00085$.

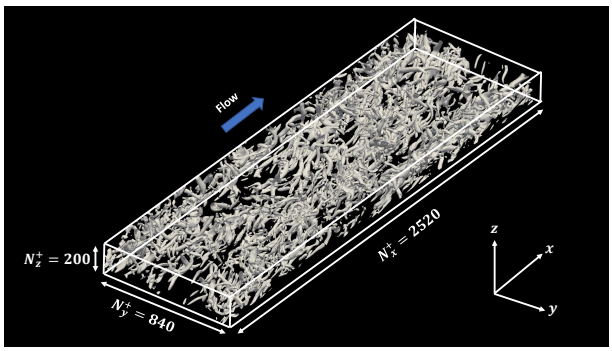

Figure 3.25 – Isocontour of second invariant of velocity gradient tensor, $Q^+ = 0.028$ at turbulent intensity $\gtrapprox$ 20%.

which is the signature of streaks discussed in section 3.2.1 and already seen in Figure 3.20. Farther from the wall, eddy sizes spread over a wider range of sizes. Some bigger eddies can be seen while some as small as in the wall region still exist. This is because turbulence properties reach a plateau right from the buffer region, so there is no turbulence decrease with the distance to the wall, and the smallest scales responsible for energy dissipation remains the same. Moreover, right after the buffer sublayer, the turbulence seems much more isotropic than in Figure 3.20, so that the swirling axis of eddies is not as easy so see in the y-z planes.

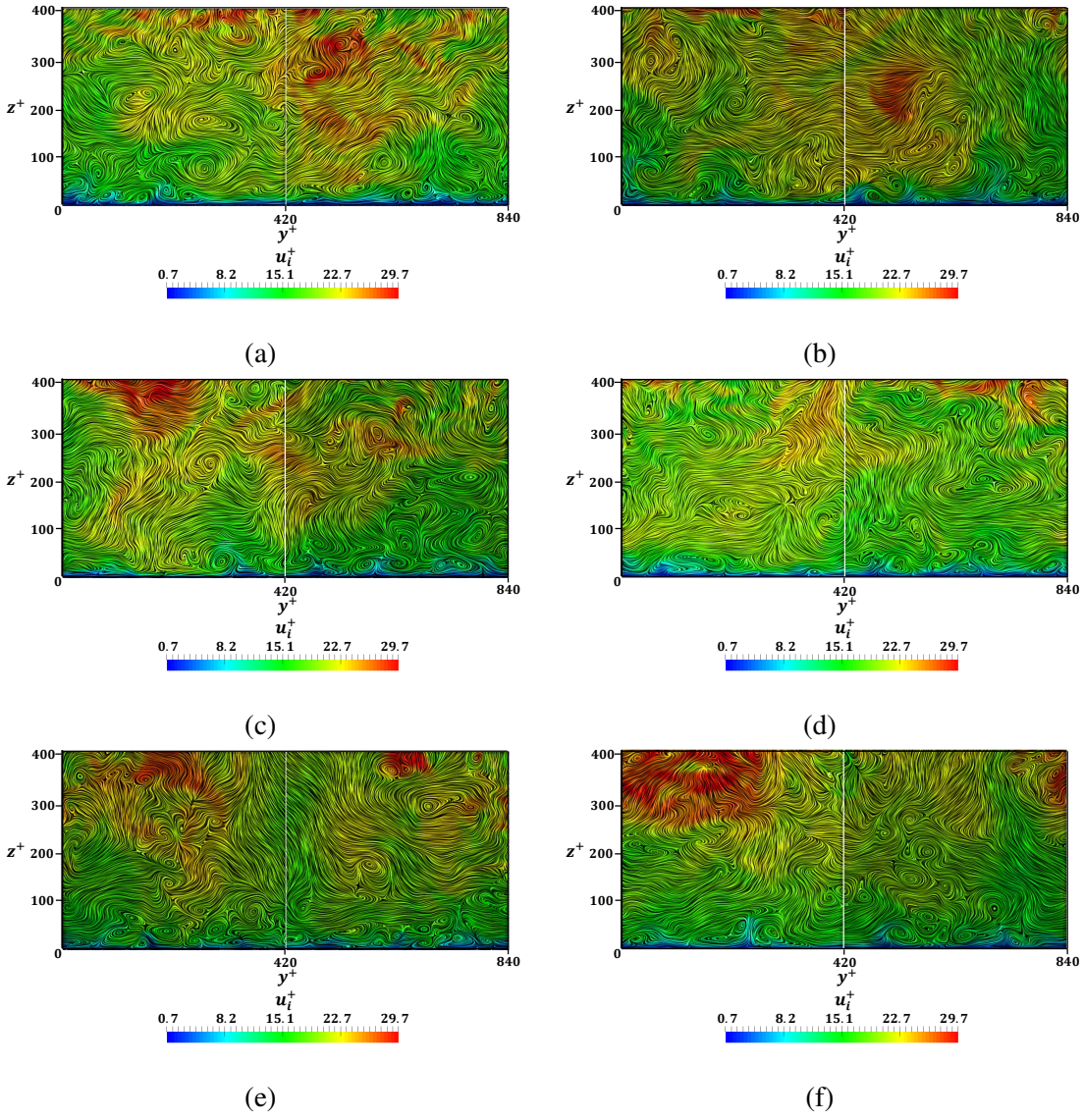

Figure 3.26 – Streamwise velocity maps ($u_i{}^+$) in various cross-sections at (a) $x^+ = 195.5$, (b) $x^+ = 580.2$, (c) $x^+ = 964.9$, (d) $x^+ = 1349.7$, (e) $x^+ = 1734.45$ and (f) $x^+ = 2112.7$ at turbulent intensity $\gtrapprox 20\%$.

3.5.3 Simulations performed for larger domain with artificial turbulence at turbulent intensity 10%

After discussing the wall bounded flow with no forced turbulence and with a forced turbulence intensity $\gtrapprox 20\%$, in this section simulations were performed by decreasing the turbulent intensity to $\gtrapprox 10\%$. To do that the control value of the dissipation rate was reduced. The simulation domain used was the same as mentioned in section 3.5 and constant shear stress was applied as reported in Table 3.4.

Figure 3.27 shows the mean and fluctuating velocity profiles along the wall normal direction. Since it followed the law of wall for both 0 and $\gtrapprox 20\%$ turbulence intensity, it is unsurprising that mean velocity follows again a linear profile in the viscous sublayer and the log-law in the inertial layer. The fluctuation velocity profile does decrease after it is maximum in the buffer sublayer, but it reaches a lower plateau value farther from the wall, before it increases again to reach the forced turbulence properties in the top box, with the same discontinuity as observed in Figure 3.21, that arises due to a change in the way time averages are done between the two regions. The same correction as in Figure 3.21 shows that linear forcing works but our implementation generates a little more turbulence than what is provided as control parameters. In this case, the actual turbulent intensity is around 13.314%.

In accordance with the previous comments, Figure 3.28 shows that mean velocity perfectly coincides with the profile from Moser et al. [125]. In the same figure, the fluctuation velocity profile resembles much more the profile with no forced turbulence (see Figure 3.16) than the profile with $\gtrapprox 20\%$ turbulence intensity (see Figure 3.22). This means that even though there is extra turbulence injected in the forcing region, it is injected far enough from the wall that is dissipates before it reaches the wall, so that at the wall, the only seen turbulence is the wall-induced one.

Figure 3.29 represents the velocity in the plane $z^+ = 4$ as color map of its streamwise component and as vectors, revealing the existence of streaks.

Also, Figures 3.30 and 3.31 present the 3D structure of such streaks. Figure 3.32 shows the streamwise component of the velocity and streamlines of the projected velocity in different sections (y-z planes). It is interesting to compare these with their counterparts for the no forced turbulence case and the strong forced turbulence case (figures 3.20 and 3.26). The turbulence coming from the top region here contains smaller eddies than when no tur-

Table 3.4 – LBM and physical parameters for wall bounded turbulence with artificial forcing at turbulent intensity of 10%.

$\epsilon_{0\,LBM}$	$\epsilon_{0\,\text{phys}}$	$\nu_{0\,LBM}$	ν_f	$\mathbf{T}_{0\,LBM}$	$\mathbf{T}_w$
–	m^2s^{-3}	–	m^2s^{-1}	–	Pa
2×10^{-8}	280	5×10^{-4}	1.5×10^{-5}	5×10^{-5}	3

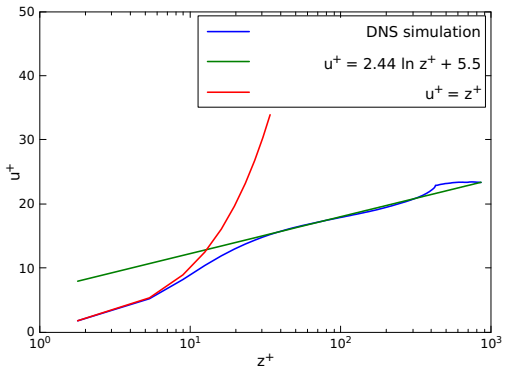

(a) Mean velocity from DNS (blue) and comparison with law of wall in the viscous sublayer (red) and with the logarithmic profile (green)

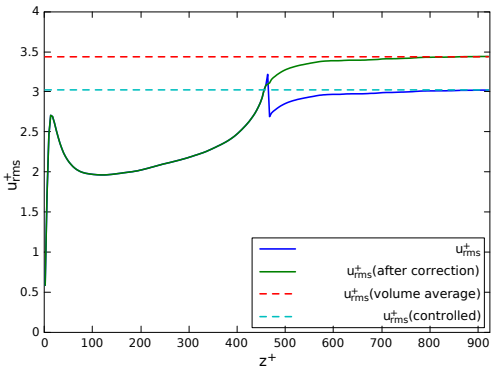

(b) Fluctuation velocity from the DNS simulation: time based RMS (blue) and corrected curve (green)

Figure 3.27 – Velocity profiles along the wall-normal direction from simulation performed at $\gtrapprox$ 10% turbulent intensity.

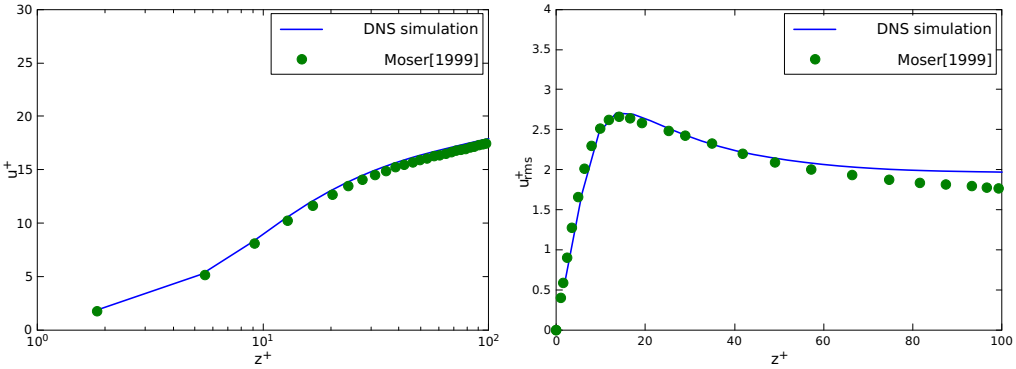

(a) (b)

Figure 3.28 – Profiles at turbulent intensity $\gtrapprox$ 10% from this work's DNS (line) and comparison with Moser et al. [125] (points) for (a) mean velocity and (b) RMS of fluctuation velocity.

bulence is injected, but the smallest eddies are still bigger than the ones produced at the wall, contrary to the strongly forced turbulence case. Although the eddies are not as small, the overall orientation of eddies varies from one plane to another in a similar way as it does for the strongly forced turbulence case. This means, that although the injected turbulence dissipates before it reaches the wall, it interacts with the turbulent structures generated at the wall when they develop further away and makes them evolve into a more isotropic flow than in a channel flow.

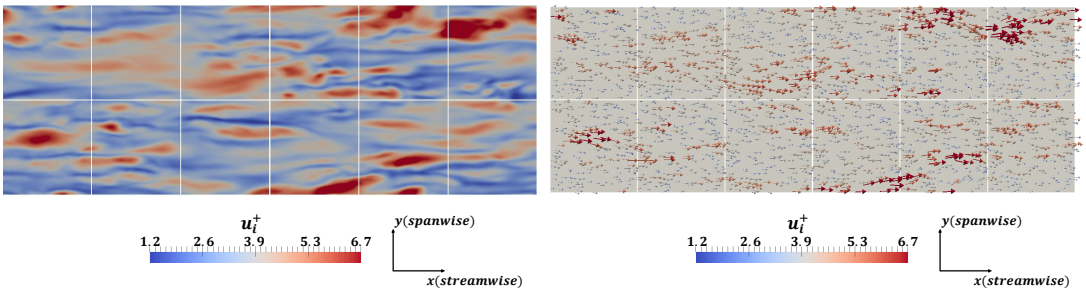

(a) (b)

Figure 3.29 – Instantaneous velocity field in the plane $z^+ = 4$ from DNS with turbulence intensity $\gtrapprox 10\%$ as (a) color map of its streamwise component and (b) vector field.

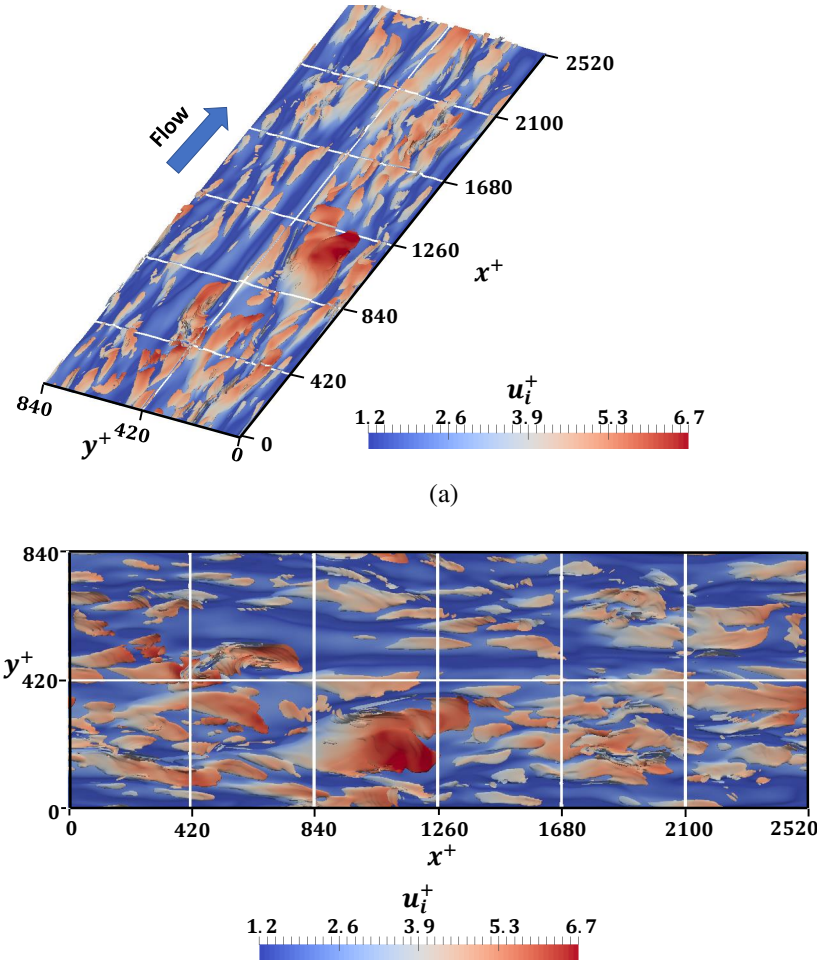

(a)

(b)

Figure 3.30 – Isocontour of q from equation (3.21) colored by instantaneous streamwise velocity component in the viscous sublayer region at turbulent intensity $\gtrapprox 10\%$: (a) 3D view and (b) top view, $q^+ = 0.00085$.

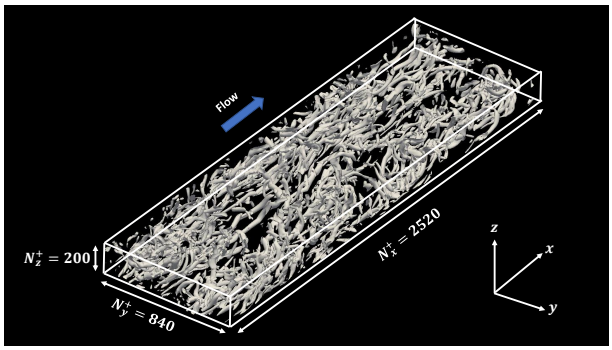

Figure 3.31 – Isocontour of second invariant of velocity gradient tensor, $Q^+ = 0.028$ at turbulent intesity $\gtrapprox 10\%$.

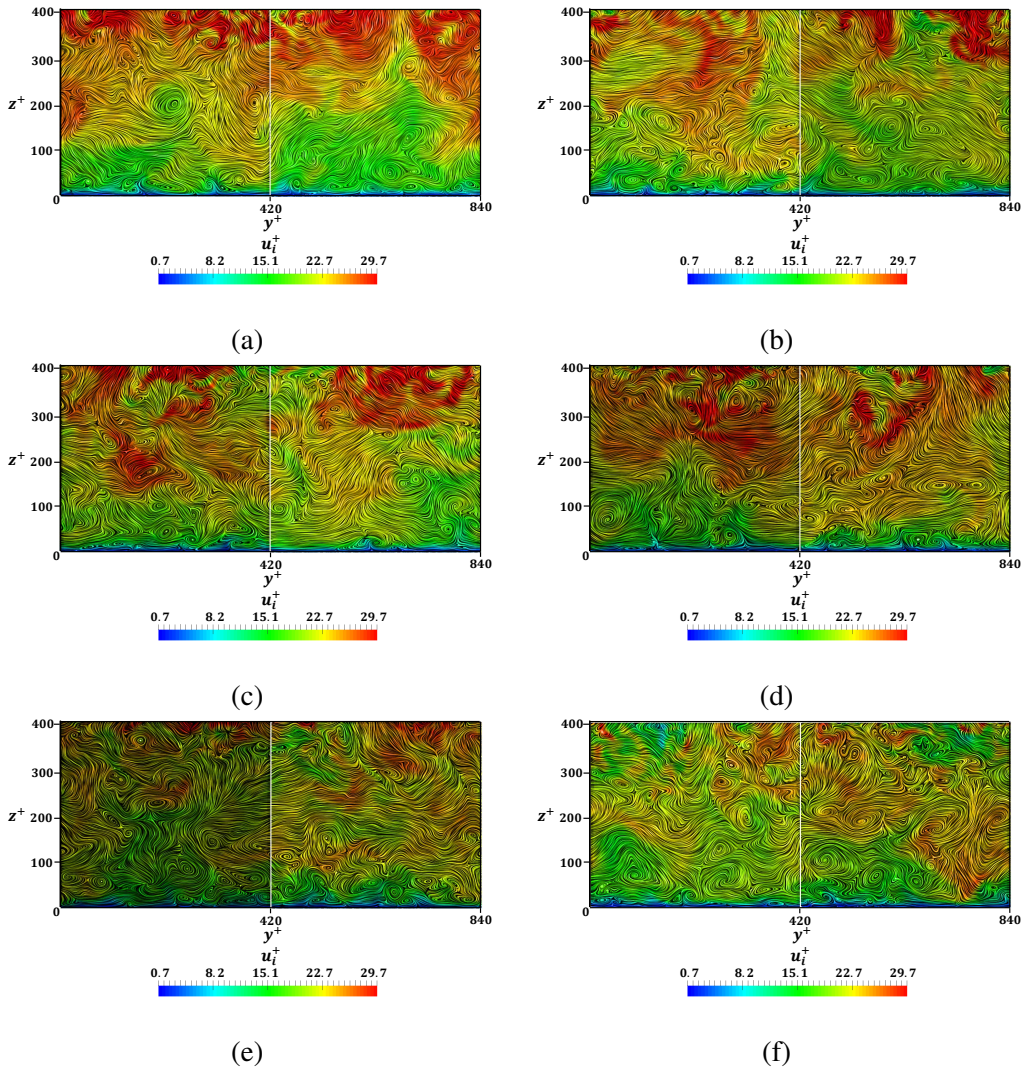

Figure 3.32 – Streamwise velocity maps ($u_i{}^+$) in various cross-sections at (a) $x^+ = 195.5$, (b) $x^+ = 580.2$, (c) $x^+ = 964.9$, (d) $x^+ = 1349.7$, (e) $x^+ = 1734.45$ and (f) $x^+ = 2112.7$ at turbulent intensity $\gtrapprox 10\%$.

3.6 Conclusion on simulations of a turbulent boundary layer

This chapter mainly dealt with the generation of fully developed three-dimensional wall bounded turbulence where simulations were performed both for larger domain and smaller domain. For the smaller domain it was seen that the turbulence log-law profile mimicked the law of wall plot from the literature. Before attaining constant velocity in turbulence region there is an increase in the mean velocity which occurs due to the fact that the forced turbulence is isotropic, and thus corresponds to turbulence far from the wall. Simulations were performed for larger domain where three cases were considered: no forcing, forcing with $\gtrapprox 20\%$ turbulence intensity and forcing with $\gtrapprox 10\%$ turbulence intensity. For the first case, that is with no forcing, the results of streamwise mean and fluctuation velocities were compared with Moser et al. [125], and good agreement of the curves were visualized. Also isocontours of second variant of velocity gradient tensor was drawn to observe all the low and high speed streaks formed in the viscous sublayer region. Then, after proper validation with the literature, simulations were run for two turbulent intensities. Good agreement was observed for the velocities close to the wall. But far from the wall at the interface there is a jump in the fluctuation velocity which is due to a longer time averaging taken to calculate the turbulent properties properly close to the wall. Also the maps for streamwise velocity at different x^+ locations show the eddies swirling around the streamwise and spanwise directions. Close to the wall the eddies are anisotropic and when we move towards the forcing region, the vortices are isotropic.

Chapter 4 : Introducing particles

Contents

As discussed in the previous chapter, the simulation of a fully developed turbulent flow has been achieved and compared to the well-known law of wall and the turbulent structures generated near the wall such as streaks have been observed. The main objective of the thesis is to evaluate the deposition rate of particles on a wall in a fully developed turbulent flow. Consequently in this chapter, the deposition and capture mechanism of inertial point particles in the fully developed turbulent boundary layer is modelled and then simulated. In the first part of this chapter we detail the Lagrangian tracking technique for the particle dynamics as well as the expressions of the forces acting on particles and statistical post-processing. Then we present the simulation of tracer particles whose instantaneous velocity is the same as the fluid to check validity of the method. The second part of the chapter deals with introduction of aerosol particles in the DNS of the fully developed turbulent flow where validation by comparison with the abundant literature is performed. A thorough investigation of transport and accumulation of aerosol particles for different Stokes number near the wall is then presented. Finally, as a consequence of time constrains, the simulation of hydrosols in liquid conditions mimicking the conditions of liquid steel in a ladle is only initiated. Preliminary results have been reported in Appendix A.

4.1 Equation of motion and implementation in the simulation

The movement of inertial particles in a fluid flow is expressed by solving the Lagrangian Particle Tracking (LPT) ordinary differential equation. Calculation is done in translational frame and thereby position and velocity of the particles are evaluated at each instant. The turbulent flow calculated by the lattice Boltzmann method is not supposed to be modified by the disperse particles. As a consequence the coupling between the continuous turbulent flow and the particle transport is assumed to be weak, so a one-way coupling exists where fluid induced forces on the particles. Basically the LPT is achieved by solving the Newton's equation of motion, where several forces are taken into account to achieve relevant coupling:

$$m_p \frac{\mathrm{d}\vec{u}_p}{\mathrm{d}t} = \sum_i \vec{F}_{pi} \tag{4.1}$$

The left hand side of equation (4.1) represents the inertia of the particles. The right hand side of the expression represents the external forces acting on the particles thus leading to their motion [19]:

$$m_p \frac{\mathrm{d}\vec{u}_p}{\mathrm{d}t} = \vec{F}_B + \vec{F}_D + \vec{F}_A + \vec{F}_P + \vec{F}_L \tag{4.2}$$

The forces $\vec{F}_B$, $\vec{F}_D$, $\vec{F}_A$, $\vec{F}_P$ and $\vec{F}_L$ are the buoyancy force, drag force, added mass or virtual force, pressure gradient force and lift force respectively. Here the expressions of these forces are that used by Dupuy et al. [19]. The drag force is expressed for particle Reynolds number lower than 0.1 and a Faxen correction can be added to take into account the inhomogeneity of the flow. Finally the Basset history force is not included in equation (4.2) since it is neglected. All the forces mentioned in equation (4.2) are implemented using a semi-implicit approach where force contributions are linearised functions of particle velocity and

acceleration:

$$m_p \frac{\mathrm{d}\vec{u}_p}{\mathrm{d}t} = \alpha \frac{\mathrm{d}\vec{u}_p}{\mathrm{d}t} + \beta \vec{u}_p + \vec{\gamma} \tag{4.3}$$

In equation (4.3), α and β are coefficients that sum contributions from the forces that can be expressed as proportional to acceleration and velocity [129]. These coefficients are functions of particle/fluid properties and flow conditions. Here the $\vec{\gamma}$ coefficient represents all the forces that are not related to the movement of particles i.e. in the forces described in the later part of the chapter: $\vec{\gamma}$ comprises of all the expressions related to fluid velocity. These three coefficients must be identified from the mathematical expression of each force as it will be derived thereafter. The evaluation of particle velocity at each time step is obtained from equation (4.3) thus producing the following linear equation:

$$m_p \frac{\vec{u}_p(t) - \vec{u}_p(t - \Delta t_p)}{\Delta t_p} = \alpha \frac{\vec{u}_p(t) - \vec{u}_p(t - \Delta t_p)}{\Delta t_p} + \beta \vec{u}_p(t) + \vec{\gamma} \tag{4.4}$$

The solution for $\vec{u}_p(t)$ is then given by:

$$\vec{u}_p(t) = \frac{(\frac{m_p - \alpha}{\Delta t_p})\vec{u}_p(t - \Delta t_p) + \vec{\gamma}}{\frac{m_p - \alpha}{\Delta t_p} - \beta} \tag{4.5}$$

Here the new values of parameters like α, β and $\vec{\gamma}$ are estimated based on the values of the previous time step. In particular, the value of $\vec{\gamma}$ is calculated at older particle location $\vec{x_p}(t - \Delta t_p)$. Hence the updated particle position from velocity can be calculated as:

$$\vec{x}_p(t) = \vec{x}_p(t - \Delta t_p) + \vec{u}_p(t)\Delta t_p + \frac{1}{2}\frac{\vec{u}_p(t) - \vec{u}_p(t - \Delta t_p)}{\Delta t_p}(\Delta t_p)^2 \tag{4.6}$$

Since the time step is constant is our numerical scheme, this expression boils down to:

$$\vec{x}_p(t) = \vec{x}_p(t - \Delta t_p) + \left(\left(1 + \frac{1}{2}\right)\vec{u}_p(t) - \frac{1}{2}\vec{u}_p(t - \Delta t_p)\right)\Delta t_p \tag{4.7}$$

To calculate fluid velocity at the particle location (x, y, z), trilinear interpolation scheme is used. This interpolation technique is the process of linearly interpolating within a 3D lattice cube, where the fluid velocities are known at the vertices of the cube. Consider a unit cube with lower/left/base vertex at the origin as shown in Figure 4.1. The velocity values at each vertex are represented as $\vec{V}_{f,000}$, $\vec{V}_{f,100}$, $\vec{V}_{f,010}$, …, $\vec{V}_{f,111}$. Suppose a particle is located inside the cube at position (x, y, z), the fluid velocity seen by the particle is denoted by $\vec{V}_{f,xyz}$.

$$\begin{aligned} \vec{V}_{f,xyz} = \vec{V}_{f,000}(1-x)(1-y)(1-z) + \vec{V}_{f,100}x(1-y)(1-z) + \\ \vec{V}_{f,010}(1-x)y(1-z) + \vec{V}_{f,001}(1-x)(1-y)z + \\ \vec{V}_{f,101}x(1-y)z + \vec{V}_{f,011}(1-x)yz + \\ \vec{V}_{f,110}xy(1-z) + \vec{V}_{f,111}xyz \end{aligned} \tag{4.8}$$

However, as discussed later in this chapter, while plotting the Faxen correction by tri-

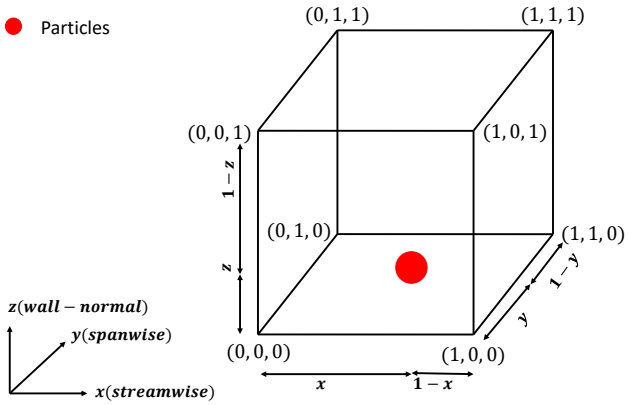

Figure 4.1 – Lattice cube in LBM with corresponding vertices with a particle inside the cube.

linear interpolation, cubic spline interpolation has also been used which uses more fluid vertices in the LBM cube to give higher precision interpolated values of fluid properties and yields much smoother curves.

The particle time step Δt_p can be chosen different from the LBM time step, in particular $\Delta t_p < \Delta t_{LBM}$ can be applied to compensate for the explicit resolution of particle motion, but we have observed that it has no impact on our simulation results since the LBM time step is also constrained by an explicit solver. So, in the following, $\Delta t_p = \Delta t_{LBM} = 1$ [tu].

4.2 Boundary conditions

The entire simulation domain is divided into two subdomains for the required MPI communication. Similarly to MPI usage for communicating fluid properties in the streamwise and spanwise directions, particles are also communicated along the streamwise and spanwise directions (Figure 4.2(a)). Also, for particles along the wall normal direction, when a particle reaches the last fluid node of one domain (Domain 1) it is reintroduced back to the other domain (Domain 2) but with negative wall normal particle velocity. This is summarized in Figure 4.2(b) where communications are represented by the black arrows. The values stored in A will be similar as A' but their components along the normal direction are flipped. This is similar to the type of boundary condition also used for fluid as described in section 3.3.

At the wall, the values of fluid properties in the boundary node has been set so that interpolation yields a controlled value at the wall. For velocity, its value in the wall nodes is set as the opposite of the first range fluid nodes, so the wall (halfway between the nodes) has a zero velocity. Values that have no known value at the wall are extrapolated from the fields inside the fluid, using second order extrapolation.

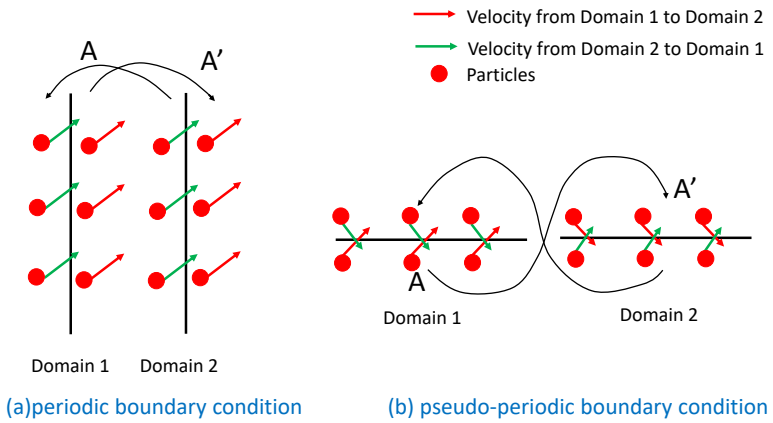

Figure 4.2 – Particle communication for (a) periodic and (b) pseudo-periodic boundary conditions.

4.3 Calculation of statistical data

With the aim of providing statistical data on the particle dynamics, the entire domain has been divided into small bins, indexed i along the wall-normal direction. All bins are the same size. Most curves shown later have been plotted with a bin size of 0.4 wall units. The mean number of particles $\bar{N_{pi}}$ is calculated by doing a time averaging of the number of particles present in each bin over a sampling time (t_{sam}) and is later saved at each bin. Here t_{sam} is the time period taken when the particles tend to reach a steady deposition rate.

$$\bar{N_{pi}} = \sum_{t_{sam}} \frac{N_{pi}(t)}{t_{sam}} \tag{4.9}$$

The mean concentration is derived by dividing the particle number by the corresponding volume of each bin.

$$\bar{C_{pi}} = \frac{\bar{N_{pi}}}{V_i} \tag{4.10}$$

The dimensionless mean concentration, $\bar{C^*_{pi}}$ is finally obtained by normalizing the concentration in each bin by the mean concentration of particles over the entire domain, $\bar{C}_{p0}$:

$$\bar{C^*_{pi}} = \frac{\bar{C_{pi}}}{\bar{C}_{p0}} \tag{4.11}$$

where the mean concentration of particles over the entire domain ($\bar{C}_{p0}$) is calculated by dividing the total number of particles ($\bar{N_p}$) initially introduced in the whole domain, by the volume of the simulation domain (V_T):

$$\bar{C}_{p0} = \frac{\sum \bar{N_p}}{V_T} \tag{4.12}$$

To investigate particle transport towards the wall, dimensionless mean drift velocity

($\bar{w}_p^+$) and RMS of wall normal fluctuating velocity (${w'}^+_{p,rms}$) have been calculated. They are calculated by considering the z component of drift velocity and the fluctuating velocity of each particle and then by taking their average (or RMS) over the total number of particles (N_{pi}) present in each bin. Hence, each individual bin has its own average velocities for each time step. Then time averaging of these velocities is done over a sampling time (t_{sam}) for each bin. Finally the velocities are made dimensionless by dividing with the fluid friction velocity ($u_{\mathbf{T}}$).

$$\bar{w}_{pi}^+ = \sum_{t_{sam}} \left(\frac{\sum_p w_p(t)}{t_{sam}\, N_{pi}(t) u_{\mathbf{T}}}\right), \quad {w'}^+_{pi,rms} = \sum_{t_{sam}} \left(\frac{\sum_p (w_p(t) - \bar{w}_p)}{t_{sam}\, N_{pi}(t) u_{\mathbf{T}}}\right) \tag{4.13}$$

4.4 Forces acting on particles

4.4.1 Drag force

Drag force, $\vec{F}_D$ is considered to be the prime force in fluid-particle interaction. It results from the difference of velocity between particles and the fluid parcel at their location. By definition, the drag accounts for the force contribution that is collinear with the drift velocity. It integrates the fluid stresses applied to the surface of the particle and as such it has two components, the friction and pressure drag. In its general form, drag is expressed according to a drag coefficient (C_D), the value of which is based on analytical development at low Reynolds number and empirical correlations derived from performed experiments or direct numerical simulations for higher Reynolds numbers.

$$C_D = \frac{||\vec{F}_D||}{\frac{\rho_f}{2}(\vec{u}_f - \vec{u}_p)^2 A_p} \tag{4.14}$$

A_p is the cross sectional area which for spherical particles equals $A_p = \frac{\pi}{4}{\mathrm{d}_p}^2$. The final expression of the drag force is thus given by:

$$\vec{F}_D = \frac{3}{4}\frac{\rho_f}{\rho_p}\frac{m_p}{\mathrm{d}_p} C_D(\vec{u}_f - \vec{u}_p)|\vec{u}_f - \vec{u}_p| \tag{4.15}$$

The drag coefficient C_D is obtained as a function of particulate Reynolds number (Re_p) which is defined as the ratio between inertial force to friction force in the flow at the particle surface, and is hence based on drift velocity:

$$Re_p = \frac{\rho_f d_p |\vec{u}_f - \vec{u}_p|}{\mu_f} \tag{4.16}$$

For small particulate Reynolds number ($Re_p < 0.1$) viscous effects prevail with no wake. Thus the drag coefficient can be derived analytically from Stokes flow:

$$C_D = \frac{24}{Re_p} \tag{4.17}$$

Because of their very small size, aerosols and inclusions remain in the Stokes condition

and the expression of C_D at higher Reynolds number does not concern the present work. The drag force used is thus given by:

$$\vec{F}_D = 3\pi\mu_f d_p \left(\vec{u}_f - \vec{u}_p\right) \tag{4.18}$$

The drag contribution to coefficient α in equation (4.4) will then be zero since the expression of drag force is not proportional to the acceleration of particles. Drag will however contribute to coefficients β and $\vec{\gamma}$ because the drag expression is related to particle velocity $\vec{u}_p$ and to fluid velocity $\vec{u}_f$. Therefore we identify:

$$\alpha = 0 \tag{4.19}$$

$$\beta = -3\pi\mu_f d_p \tag{4.20}$$

$$\vec{\gamma} = 3\pi\mu_f d_p \, \vec{u}_f \tag{4.21}$$

Inserting the three coefficients in equation (4.3) the following expression for drag force is well obtained:

$$m_p \frac{\mathrm{d}\vec{u}_p}{\mathrm{d}t} = 3\pi\mu_f d_p \left(\vec{u}_f - \vec{u}_p\right) \tag{4.22}$$

The expression of the drag force acting on a sphere translating in a non-uniform flow field, which is particularly the situation near the wall, can be extended to account for it considering the flow in Stokes condition. A so-called "Faxen correction" [130] is then added to Stokes drag force, and the coefficient $\vec{\gamma}$ will have an added parameter:

$$\vec{\gamma} = 3\pi\mu_f d_p \, \vec{u}_f + \frac{\pi}{8} \, \mu_f \, {d_p}^3 \, \vec{\nabla}^2 \, \vec{u}_f \tag{4.23}$$

Henceforth the final drag force expression with the Faxen correction is given as:

$$m_p \frac{\mathrm{d}\vec{u}_p}{\mathrm{d}t} = \underbrace{3\pi\mu_f d_p \left(\vec{u}_f - \vec{u}_p\right)}_{\text{Stokes Drag}} + \underbrace{\frac{\pi}{8} \, \mu_f \, {d_p}^3 \, \vec{\nabla}^2 \, \vec{u}_f}_{\text{Faxen correction}} \tag{4.24}$$

Notice that the ratio between the Faxen correction and Stokes drag is given by:

$$\frac{\text{Faxen}}{\text{Drag}} = \frac{1}{24} \frac{{d^2}_p \vec{\nabla}^2 \vec{u}_f}{\left(\vec{u}_f - \vec{u}_p\right)} \tag{4.25}$$

When the diameter of the particle decreases, the value of the Faxen correction decreases resulting in a decrease of this ratio.

4.4.2 Pressure gradient and buoyancy forces

The pressure gradient force is a volumetric force that accounts for the difference in the pressure across the fluid seen by the particle. The local stress tensor in the flow is related to fluid acceleration through Navier-Stokes equation. Thus the pressure gradient and the divergence of viscous stresses can be estimated from local fluid acceleration and volume forces acting on the fluid. Calculating fluid acceleration as material derivative of fluid velocity and

considering gravity as the only volume force, it yields:

$$-\vec{\nabla}p + \vec{\nabla}\cdot\bar{\bar{\tau}} = \rho_f(\frac{\mathrm{D}\vec{u}_f}{\mathrm{D}t} - \vec{g}) \tag{4.26}$$

For particles smaller than all flow scales, the divergence of the stress tensor can be assumed to be constant at the particle scale. The resulting force acting on particle surface can thus be calculated as:

$$\vec{F}_P = \frac{m_p}{\rho_p}\,(-\vec{\nabla}p + \vec{\nabla}\cdot\bar{\bar{\tau}}) \tag{4.27}$$

Hence the overall pressure gradient force becomes:

$$\vec{F}_P = m_p\frac{\rho_f}{\rho_p}\,\frac{\mathrm{D}\vec{u}_f}{\mathrm{D}t} - m_p\,\frac{\rho_f}{\rho_p}\,\vec{g} \tag{4.28}$$

where the second term (i.e. $m_p\rho_f\ g/\rho_p$) is Archimedes force. This force is significant for solid particles in a liquid phase where $\rho_p/\rho_f \sim 1$, but it is negligible for solids in gas flows where $\rho_p/\rho_f \gg 1$. Usually, Archimedes force is combined with the weight (of particle) to give the well known buoyancy force:

$$\vec{F}_B = m_p\,\frac{\rho_f}{\rho_p}\,(\frac{\rho_p}{\rho_f} - 1)\,\vec{g} \tag{4.29}$$

Hence the combination of the dynamic pressure gradient and buoyancy force is expressed as:

$$\vec{F}_P + \vec{F}_B = m_p\frac{\rho_f}{\rho_p}\,\frac{\mathrm{D}\vec{u}_f}{\mathrm{D}t} + m_p\,\frac{\rho_f}{\rho_p}\,(\frac{\rho_p}{\rho_f} - 1)\,\vec{g} \tag{4.30}$$

In equation (4.30), $\mathrm{D}\vec{u}_f/\mathrm{D}t$ represents the local acceleration in the flow, it is calculated as the material derivative fluid velocity at the centre of the particle, which can be expressed as:

$$\frac{\mathrm{D}\vec{u}_f}{\mathrm{D}t} = \frac{\partial\vec{u}_f}{\partial t} + (\nabla\vec{u}_f)\cdot\vec{u}_f \tag{4.31}$$

which requires interpolating both the velocity of the fluid and its gradient at particle location.

Similarly to drag, to implement the expression for pressure gradient force in the code, only the coefficient $\vec{\gamma}$ is taken into consideration since there are no terms in equation (4.28) deriving from particle velocity or acceleration, hence α and β are null.

$$\alpha = 0 \tag{4.32}$$

$$\beta = 0 \tag{4.33}$$

$$\vec{\gamma} = \frac{m_p\rho_f}{\rho_p}\,\frac{\mathrm{D}\vec{u}_f}{\mathrm{D}t} + \frac{m_p\rho_f}{\rho_p}(\frac{\rho_p}{\rho_f} - 1)\vec{g} \tag{4.34}$$

Since we restrict our investigation to non-buoyant particles, the gravity term is omitted in the LPT simulation, so:

$$\vec{\gamma} = \frac{m_p\rho_f}{\rho_p}\,\frac{\mathrm{D}\vec{u}_f}{\mathrm{D}t} \tag{4.35}$$

Hence the overall pressure gradient used for the simulation becomes:

$$\vec{F}_P = m_p \frac{\rho_f}{\rho_p} \frac{\mathrm{D}\vec{u}_f}{\mathrm{D}t} \tag{4.36}$$

4.4.3 Added mass force

Added mass force also known as virtual mass force is the inertia added to the particle when it as accelerating or decelerating due to some amount of fluid from the system surrounding it that is set in motion with the particle. For clarity, this force is modelled as some volume of fluid moving with the object, although in reality all the fluid will be accelerated to various degrees. Also, analytical expressions for added mass force can be obtained for low particulate Reynolds number, but, for higher particulate Reynolds numbers, empirical coefficients have been defined from experimental investigations. Odar and Hamilton [131] performed experiments and provided the expression for added mass force which is given by:

$$\vec{F}_A = C_M \, \rho_f \, \frac{m_p}{\rho_p} \, (\frac{\mathrm{D}\vec{u}_f}{\mathrm{D}t} - \frac{\mathrm{d}\vec{u}_p}{\mathrm{d}t}) \tag{4.37}$$

It has been found that the coefficient C_M is equal or very close to $\frac{1}{2}$ in all flow conditions [132, 133]. $\mathrm{D}u_f/\mathrm{D}t$ is the material derivative of fluid acceleration calculated at the centre of the particle. As observed in equation (4.37), the coefficients which should be defined are α and $\vec{\gamma}$ related to particle acceleration and extra force, they are identified as:

$$\alpha = -\rho_f \, C_M \, \frac{m_p}{\rho_p} \tag{4.38}$$

$$\beta = 0 \tag{4.39}$$

$$\vec{\gamma} = \rho_f \, C_M \, \frac{m_p}{\rho_p} \, \frac{\mathrm{D}\vec{u}_f}{\mathrm{D}t} \tag{4.40}$$

Inserting the three coefficients in equation (4.3), added mass is finally implemented as:

$$\vec{F}_A = \frac{1}{2} \, \rho_f \, \frac{m_p}{\rho_p} \, (\frac{\mathrm{D}\vec{u}_f}{\mathrm{D}t} - \frac{\mathrm{d}\vec{u}_p}{\mathrm{d}t}) \tag{4.41}$$

4.4.4 Slip-Shear lift force

The shear lift originates from differential velocity magnitude at each side of a particle that slides in a shear flow. The drift velocity added to the shear yield different velocities, that in turn yield non-symmetrical distributions of pressure and viscous stresses at the particle surface. Since it is induced by the shear of the flow at a larger scale than the particle, it is fundamentally different from aerodynamic lift force. Saffman [134] derived an expression for the slip shear lift force in a 3D flow, that is:

$$\vec{F}_{SL} = \frac{\rho_f}{2} \, A_p \, C_{SL} \, d_p \, ((\vec{u}_f - \vec{u}_p) \times \vec{\omega}_f) \tag{4.42}$$

that is expressed as a function of vorticity in the flow $\vec{\omega}_f = \vec{\mathrm{rot}}(\vec{u}_f) = \vec{\nabla} \times \vec{u}_f$ and cross section area of the particle $A_p = \frac{\pi}{4} {d_p}^2$.

Sommerfeld [133] provides an empirical correlation for the coefficient C_{SL}:

$$\begin{aligned} C_{SL} = \frac{4.1126}{Re_S^{0.5}} \left(1 - 0.3314 \left(0.5 \frac{Re_s}{Re_p}\right)^{0.5}\right) \exp(-0.1\, Re_p) & \\ + 0.3314 \left(0.5 \frac{Re_s}{Re_p}\right)^{0.5} \quad , Re_p \leq 40 & \\ = 0.15238 \quad , Re_p \geq 40 & \end{aligned} \tag{4.43}$$

It depends on the previously defined particulate Reynolds number as well as on a shear based Reynolds number defined as:

$$Re_s = \frac{\rho_f {d_p}^2 |\vec{\omega}_f|}{\mu_f} \tag{4.44}$$

The coefficients that need to be taken into account are β and $\vec{\gamma}$ which are evaluated as:

$$\alpha = 0 \tag{4.45}$$

$$\beta = 0 \tag{4.46}$$

$$\vec{\gamma} = \frac{\rho_f}{2} \frac{\pi}{4} {d_p}^2 C_{SL}\, d_p \left((\vec{u}_f - \vec{u}_p) \times \vec{\omega}_f\right) \tag{4.47}$$

Inserting the three coefficients in equation (4.3) the following expression for lift force is obtained:

$$\vec{F}_{SL} = \frac{\rho_f}{2} \frac{\pi}{4} {d_p}^2 C_{SL}\, d_p \left((\vec{u}_f - \vec{u}_p) \times \vec{\omega}_f\right) \tag{4.48}$$

4.5 Introducing tracers

The test case that is performed is quite simple as when tracers are included as particles, the inertial effects are excluded and the velocity of the tracer is equal to the instantaneous velocity of the fluid at the particle location. The three parameters α, β and $\vec{\gamma}$ must be chosen appropriately in order to achieve $\vec{u}_p = \vec{u}_f$. It is readily obtained with:

$$\alpha = m_p \tag{4.49}$$

$$\beta = 3\pi\mu_f d_p \tag{4.50}$$

$$\vec{\gamma} = -3\pi\mu_f d_p \vec{u}_f \tag{4.51}$$

that makes Newton's equation of motion (4.3) become:

$$m_p \frac{\mathrm{d}\vec{u}_p}{\mathrm{d}t} = m_p \frac{\mathrm{d}\vec{u}_p}{\mathrm{d}t} + 3\pi\mu d_p \vec{u}_p + (-3\pi\mu d_p \vec{u}_f) \tag{4.52}$$

that boils down to:

$$\vec{u}_p = \vec{u}_f \tag{4.53}$$

The simulation domain used to study tracers was small, that is it had LBM nodes as:

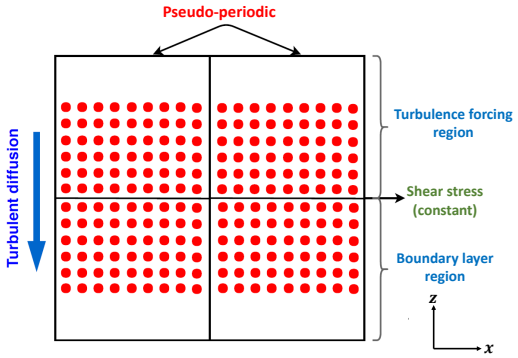

Figure 4.3 – Schematics of initial tracers distribution in the domain.

$N_x \times N_y \times N_z = 160 \times 80 \times 160$. The fluid flow simulation corresponding to this case is illustrated in section 3.4 in Chapter 3, and the physical properties and flow conditions are reported in Table 4.1. Figure 4.3 schematically represents the tracers and how they are placed equidistantly along the three directions initially. As it can be seen, the concentration is not initially homogeneous since volume near the bottom and top walls are free of particles.

Figure 4.4 is plotted for the concentration, which is time averaged over the sampling time t^+_{sam}, which is taken to be 200 τ^+, where

$$\tau^+ = \tau / t^* \tag{4.54}$$

Here, integral time scale is calculated based on the ratio between the size of the largest eddy (which is 20% of domain size) to the characteristic velocity (u_L) of this eddy in the flow.

$$\tau = L / u_L \tag{4.55}$$

u_L can be calculated from the root-mean-square (RMS) of the fluctuation velocity:

$$u_L = \left(\overline{u'^2}\right)^{1/2} \tag{4.56}$$

In equation (4.54), t^* represents the characteristic time of the turbulent flow given by:

$$t^* = \nu_f / u_{\mathbf{T}}^2 \tag{4.57}$$

Simulation results highlight that no fluid parcel crosses the bottom wall meaning that there is no deposition, which means the particle deposition rate is therefore null:

$$(\varphi_p)_{wall} = 0 \tag{4.58}$$

The particle concentration is perfectly homogeneous throughout the domain when the turbulence is fully developed. This can be proved by visualizing the plot of dimensionless concentration with respect to the wall distance as shown in Figure 4.4. It is illustrated clearly that the ratio of the concentration obtained from the simulation to the mean concentration

Table 4.1 – Physical properties and turbulent flow conditions used for tracer simulation

Fluid properties	
ρ_f (kg m^{-3})	1.225
μ_f (kg m^{-1} s^{-1})	1.8×10^{-5}
η_f (µm)	40
$\mathbf{T}_w$ (Pa)	2.2
ϵ (m^2 s^{-3})	280 *
$u_{\mathbf{T}}$ (m s^{-1})	1.2 *
	* *dependent parameters*
Domain size and numerical conditions	
$L_x \times L_y \times L_z$ (mm^3)	$20 \times 10 \times 20$
$N_x \times N_y \times N_z$	$160 \times 80 \times 160$
$\Delta t_p(LBM)$ ([tu])	1
Total sampling time (t^+_{sam})	200 τ^+
Number of bins	160
Particle conditions	
d_p (µm)	38
Initial number of particles	400000

is equal to unity thus attaining equal homogeneous concentration in all the domain.

4.6 Aerosol deposition

The main objective of the simulation for deposition of aerosols is to compare the simulation results against the abundant literature on this topic. The only forces taken into account in such simulations are the inertia and the drag force which prevail in aerosol conditions [135, 136]. Other forces remain negligible because of the high density ratio. This assumption will be evaluated and confirmed at the end of this chapter. Also, Faxen correction is not included in the drag force and it will also be discussed in the latter part of this chapter. Here, simulations were performed in the regime of moderate inertia ($0.1 \leq {\tau_p}^+ \leq 40$) and a correlation was extracted for the dimensionless deposition velocity versus Stokes number.

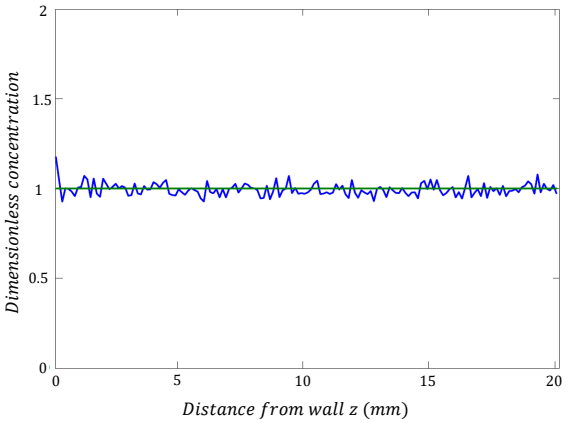

Figure 4.4 – Schematics of tracers distribution in the domain.

4.6.1 Domain geometry and simulation conditions

The simulation domain used to study aerosol deposition is the same as the one used for tracers, it has LBM nodes as: $N_x \times N_y \times N_z = 160 \times 80 \times 160 = 20 \times 10 \times 20$ mm^3. The rationale for using this small domain rather than the larger domain studied in Chapter 3 is to obtain the simulation results in a faster computational time. The domain under study is divided into two regions: the top part consists in the turbulence production region while the bottom part is the boundary layer region which was studied vividly in chapter 3. As shown schematically in Figure 4.5, the aerosol point particles are initially introduced in the turbulence production region, then particles are transported towards the wall by turbulent eddies before finally depositing. The simulation conditions are reported in Table 4.2. When particles deposit, they are reintroduced at a random position in the turbulence production region, so that the total number of particles and the corresponding concentration are constant during simulations.

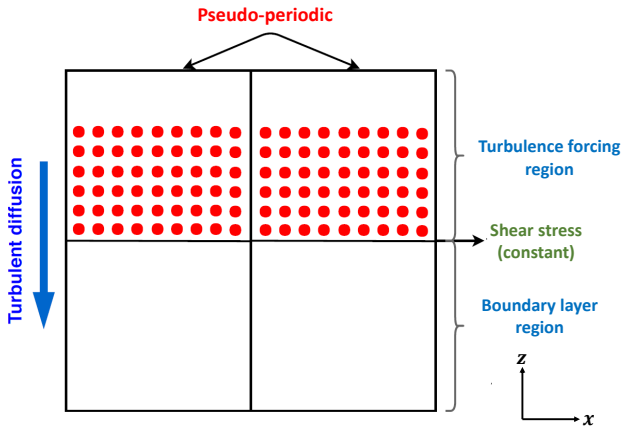

Figure 4.5 – Schematics of initial aerosol distribution in the domain.

The physical properties of the fluid phase, reported in Table 4.2 are that of air since most of experimental and numerical investigations are performed with air in the literature [25, 26, 137, 138]. The diameters of the aerosol particles are chosen in the range from 1 to 40 microns. These values are smaller than the Kolmogorov length scale, in order to satisfy the condition of point inertial particles. They are also larger than sub-micrometer because Brownian diffusion is not considered in our investigation. These set of simulations are performed for aerosol particles and compared with the literature on this topic. The density ratio between the solid and gas phases is kept constant ($\rho_p/\rho_f = 965$), which is the order of magnitude usually observed for aerosols ($\approx 10^3$) while the diameter of the particles is changed for each simulation (from 2 to 38 µm) thus changing the Stokes number between

Table 4.2 – Physical properties and turbulent flow conditions used for aerosol simulation.

Fluid properties	
ρ_f (kg m^{-3})	1.225
μ_f (kg m^{-1} s^{-1})	1.8×10^{-5}
η_f (µm)	40
$\mathbf{T}_w$ (Pa)	2.2
ϵ (m^2 s^{-3})	280 *
$u_{\mathbf{T}}$ (m s^{-1})	1.2 *
	* *dependent parameters*
Domain size and numerical conditions	
$L_x \times L_y \times L_z$ (mm^3)	$20 \times 10 \times 20$
$N_x \times N_y \times N_z$	$160 \times 80 \times 160$
$\Delta t_p(LBM)$ ([tu])	1
Total sampling time (t^+_{sam})	300 τ^+
Number of bins	640
Particle conditions	
d_p (µm)	$2 - 38$
ρ_p ($kg\ m^{-3}$)	1182
Initial number of particles	400000

0.1 and 40. The expression of the Stokes number (${\tau_p}^+$) is given by:

$${\tau_p}^+ = \frac{\rho_p {d_p}^2}{18\mu_f t^*} \tag{4.59}$$

The Stokes number (${\tau_p}^+$) for the present simulations is taken to be larger than or equal to 0.1, so that particle transport remains in the turbulent dispersion and moderate inertia regimes [27].

The parameters like concentration, mean drift velocity and RMS of fluctuation velocity are evaluated by time averaging over a sampling time (t^+_{sam}), which, in these simulations, is taken to be $300\tau^+$, where $\tau^+ = \tau/t^*$, as detailed in equations (4.54), (4.55) and (4.57). Also the time step for the resolution of the motion of particles in the simulation (Δt_p) is taken to be equal to the time step of the flow i.e. $\Delta t_p = \Delta t_{LBM}$.

4.6.2 Particle capture condition at wall

Particles are assumed to be captured when there is a direct contact with the wall, in other words when the separation distance (z_c) between point particles and the wall is lower than or equal to particle radius:

$$z_c \leq \frac{d_p}{2} \tag{4.60}$$

In the present study, we considered a perfectly smooth wall without any roughness and we did not take into account attractive Van der Waals forces acting at very short range distance (10 to 100 nm) between the wall and the particles. As a consequence, the lubrication effect is not introduced in the modeling because the deposition rate would then vanish when the roughness height tends to zero [19].

Here no rebound and re-entrainment effects are considered which means that when a particle touches the wall, it is considered as deposited, and it is again reintroduced back to the turbulence production region so as to maintain constant concentration of particles throughout the simulation. It is compulsory to attain constant concentration of particles so as to evaluate the deposition flux which depends on mean concentration. The deposition velocity (u_d) is defined as the ratio between the mean flux density of particles that are deposited on wall ($\bar{\varphi}_p)_{wall}$) to the mean concentration of particles in the bulk fluid flow ($\bar{C}_{p0}$):

$$u_d = \frac{(\bar{\varphi}_p)_{wall}}{\bar{C}_{p0}} \tag{4.61}$$

where

$$(\bar{\varphi}_p)_{wall} = \sum_{t_{sam}} \frac{N_{p,wall}}{S_{xy} t_{sam}} \tag{4.62}$$

Here $N_{p,wall}$ represents the total number of particles deposited on the wall over the area S_{xy} over a period of sampling time t_{sam} and S_{xy} denotes the surface area which is expressed by $S_{xy} = L_x \times L_y$.

4.6.3 Aerosol particle deposition rate

Figure 4.6 shows the dimensionless plot between deposition velocity and particulate Stokes number for ${\tau_p}^+ > 0.1$ which corresponds to turbulent dispersion and moderate inertia regime. The black colored squared markers denote our simulation results, covering the same range as the experimental and numerical values obtained by different authors [20, 26, 27, 139, 140] and a very good agreement is observed. As already well established, the deposition velocity (${u_d}^+$) increases with the Stokes number in turbulent dispersion conditions until it reaches a regime dominated by particle inertia where it levels off. The reason behind the constant deposition velocity is that when particle inertia gets bigger than some critical value, the effect of smaller scales of turbulence (shorter in time) are only perceived by the particles on average over a period scaled by particle response time, so that their contribution to turbulent transport it capped. In other words, when particle inertia is big enough to smooth the effects of smaller turbulence scales, the effect of such scales on particle motion becomes negligible. The value of constant deposition velocity (${u_d}^+ = 0.14$) extracted from our simulations agrees very well with the values in the literature.

For a deeper investigation of the deposition mechanism, we have distinguished the transport of relatively high inertia aerosols (${\tau_p}^+ = 25$ and 6 corresponding to $d_p = 14.3$ and 29.2 µm respectively) from lower inertia aerosols (${\tau_p}^+ = 0.4$ and 0.2 corresponding to $d_p = 3.7$ and 2.6 µm respectively).

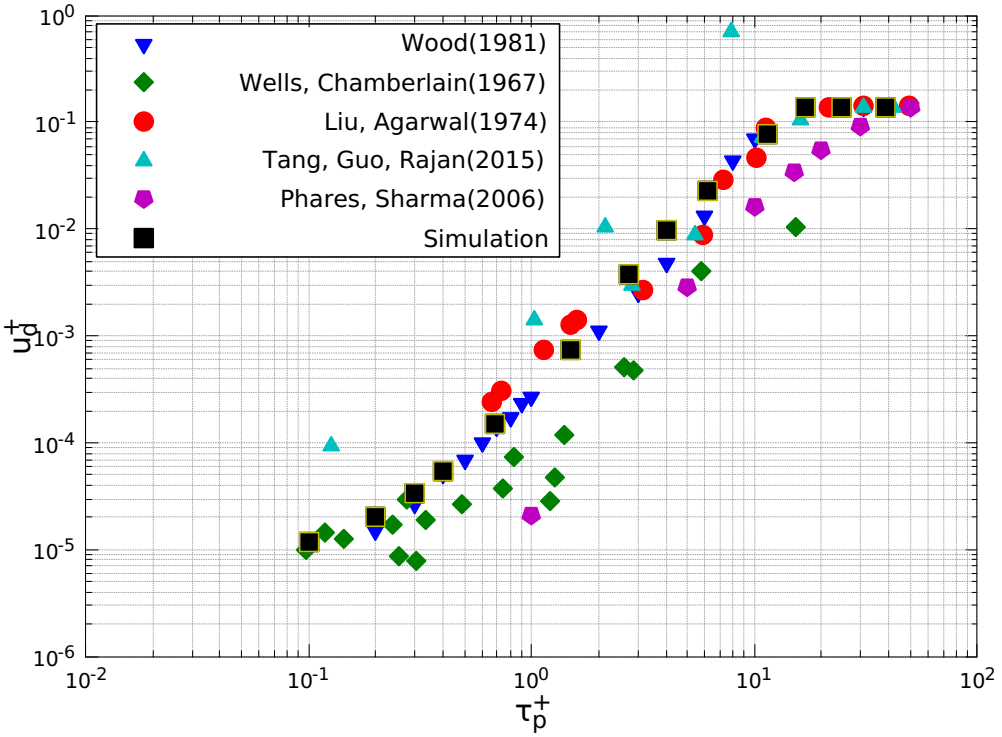

Figure 4.6 – Dimensionless plot of deposition velocity vs. Stokes number. Comparison between our simulation results with literature data.

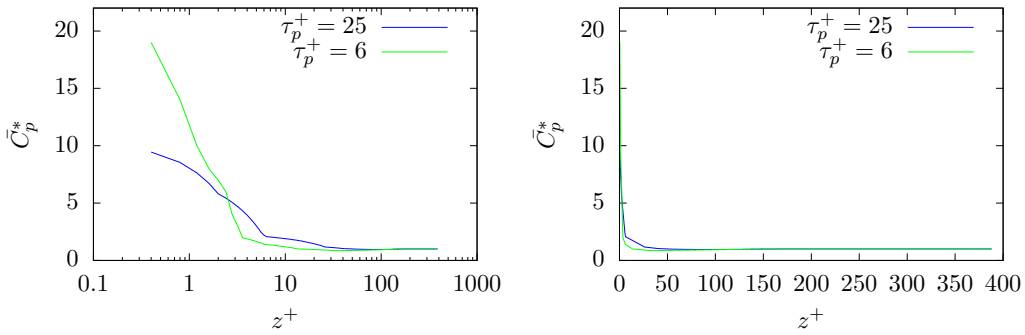

Figure 4.7 – Dimensionless mean particle concentration plotted in (a) logscale and (b) cartesian scales, for high Stokes numbers (${\tau_p}^+ = 25$ and 6).

4.6.3.1 High inertia aerosols (${\tau_p}^+ = 25$ and 6)

Figure 4.7(a) plots the evolution of the mean concentration of higher inertia particles (${\tau_p}^+ = 25$ and 6) along the wall normal direction. It clearly emphasizes a relatively constant concentration far from the wall and a high concentration close to the wall, corresponding to the accumulation region observed by many authors [34, 35]. Outside the accumulation region, the relatively high turbulence, produced either by the wall friction or by artificial forcing, eases particle transport.

This trend of accumulation of particles close to the wall was observed and discussed by several authors in the literature [17, 19, 32, 141, 142], and Stokes number is considered as a prime parameter which plays a strong role in accumulation. With the insight provided by Soldati's team [35], the accumulation of aerosols is the result of the near wall flux balance between the following contributions: (i) turbophoresis phenomenon which transports particles from the bulk turbulent flow towards accumulation region, (ii) free flight mechanism which passes the particles through the accumulation region and (iii) depositional diffusional flux which eliminates particles from the accumulation region by deposition because of the weak (but sufficient) turbulent fluctuations in this region. From Figure 4.7(a), which is plotted in semi-log scale, it can be seen that the concentration profile for ${\tau_p}^+ = 6$ is much higher than that of ${\tau_p}^+ = 25$ close to wall in the viscous sublayer region. It can be readily explained by the importance of the free-flight mechanism since particles with lower inertia less likely to execute a free-flight through whole accumulation region and thus depend more on diffusion flux to deposit at the wall as illustrated in Figure 4.8. Figure 4.8 compares the RMS of the particle wall-normal velocity ($w'^+_{p,rms}$) close to the wall in the accumulation region. Turbulence induced particle velocity fluctuations are damped by inertia leading to a more efficient flux of diffusion for lower inertia particles. Since turbulence is low in the near wall region, fluctuations are not much damped, even by higher inertia particles, so that fluctuation damping does not compensate for the higher deposition rate of higher inertia particles driven by free flight mechanism.

An other way to point out the particle drift velocity and the deposition rate is provided in Figure 4.9, plotting the profiles of particle wall normal velocity along the wall-normal axis. In this figure, the different regions of the boundary layer are also indicated, based

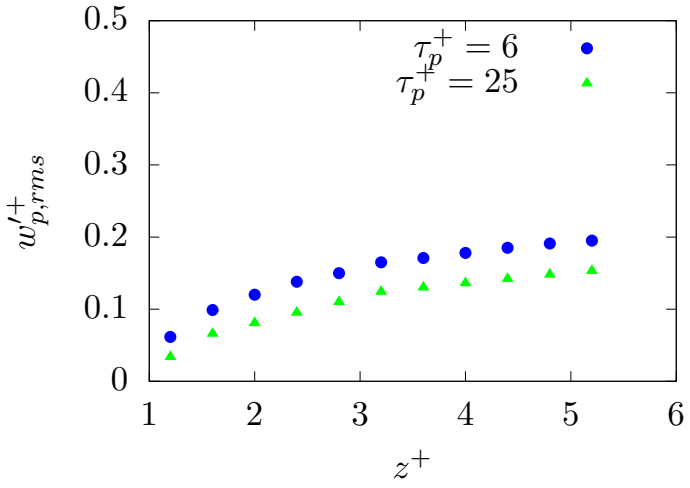

Figure 4.8 – Near-wall variation of the fluctuating particle wall normal velocity, for high Stokes number ($\tau_p{}^+ = 25$ and 6).

on the results presented in Chapter 2, such as in Figure 3.12. The particle velocity profiles from Figure 4.9 indicate negative values since the particles are travelling towards the wall from the top of the domain before finally depositing on the wall. Moreover, the average wall-normal particle velocity is higher for $\tau_p{}^+ = 25$, thus leading to higher deposition rate. Same trends are qualitatively obtained for the open channel flow problem [35].

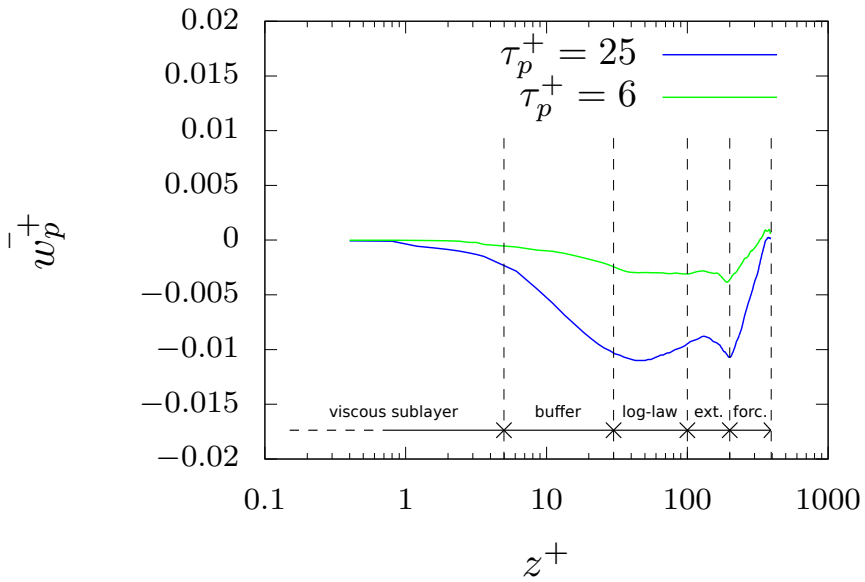

Figure 4.9 – Mean particle wall normal velocity along the wall normal direction for high Stokes number ($\tau_p{}^+ = 25$ and 6).

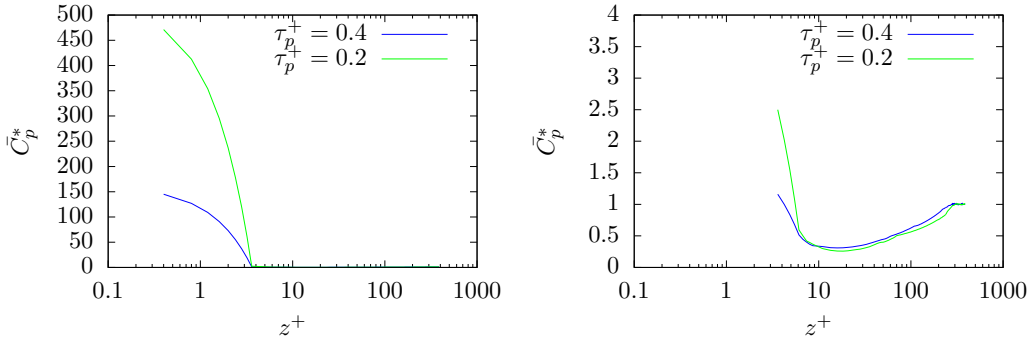

Figure 4.10 – Dimensionless mean concentration of particles as a function of the distance to the wall (a) for all the bins, (b) leaving one node (4 bins) close to the wall for low Stokes numbers (${\tau_p}^+ = 0.4$ and 0.2).

4.6.4 Low inertia aerosols (${\tau_p}^+ = 0.4$ and 0.2)

The dynamic behavior of low inertia particles (${\tau_p}^+ < 1$) is much more pronounced as seen in Figure 4.10, revealing a very high accumulation of aerosols near the wall. Low inertia prevents particles from crossing the low turbulence region from free flight transport. Figures 4.10(a) and (b) are plotted with two different scales, and Figure 4.10(b) ignores the first 4 bins closest to the wall. This is done because for lower inertia particles the concentration of particles in that single fluid node (which consists of 4 bins) closest to the wall is so high that it is difficult to observe concentration profile on the remaining nodes. Figure 4.10 clearly reveals the trend of concentration profile and it can be seen that from the wall to the forcing region, the concentration first decreases and then slowly increases before reaching the mean concentration value (i.e. unity for dimensionless concentration). As a huge number of particles accumulate in the 4 bins closest to the wall, the value of the concentration is below unity in most of the bins.

The profiles of the mean wall normal velocity (Figure 4.11) have the same trend that those obtained for the higher inertia particles (see Figure 4.9), i.e. negative values indicate the particle transport toward the wall. However, because of the low inertia, the velocity magnitude is five times lower. It can also be seen that the drift velocity for ${\tau_p}^+ = 0.4$ has a slightly more negative value than ${\tau_p}^+ = 0.2$ which shows that the higher inertia, the higher the drift velocity.

4.6.5 Dynamics of aerosols

Figure 4.12 compares the profile of wall-normal particle fluctuation velocity ($w_p'^+$) with the fluid fluctuation velocity. We first notice, as discussed earlier in Chapter 3, that the profiles are relatively flat (for $z^+ > 30$) in contrast with that obtained in wall-bounded turbulence. This is readily explained by the turbulence forcing smoothing the turbulence intensity in a large part of the simulation domain. Otherwise Figure 4.12 shows that the particle turbulent fluctuations are lower than that of the fluid, and the difference logically increases with particle inertia. Hence as Stokes number increases, particles are not able to follow all fluid fluctuations: this effect is referred as inertial filtering [35]. For instance the

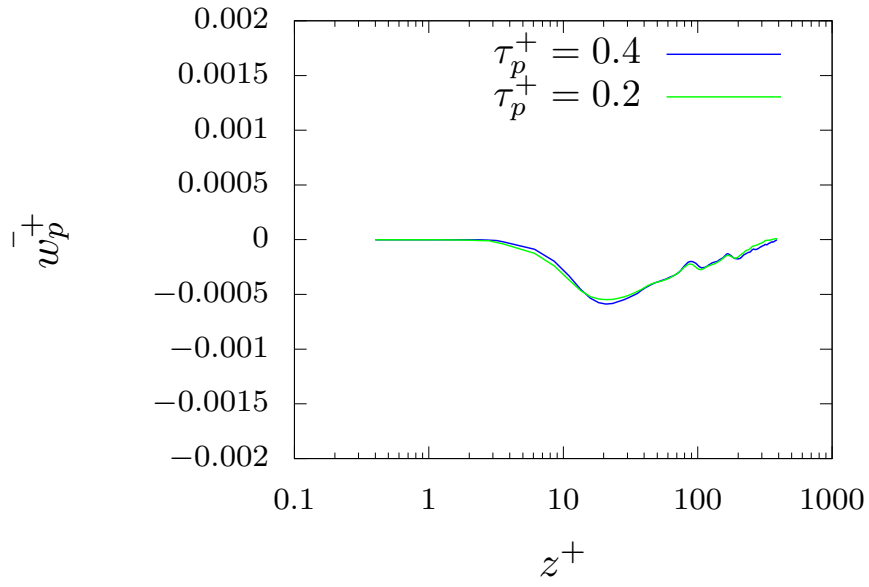

Figure 4.11 – Mean particle wall normal velocity along the wall normal direction for low Stokes number ($\tau_p{}^+ = 0.4$ and0.2).

fluctuation velocity profile for $\tau_p{}^+ = 25$ is lower than the one for $\tau_p{}^+ = 0.2$, while this latter profile is close to the local fluctuation velocity of the fluid. Fluctuations of particle velocity in the wall-normal direction reveal a qualitatively good agreement with the numerical results performed by Narayanan et al. [35] for an open channel flow and reported in Figure 4.13.

For a better description of the dynamics of individual aerosol particles near the wall,

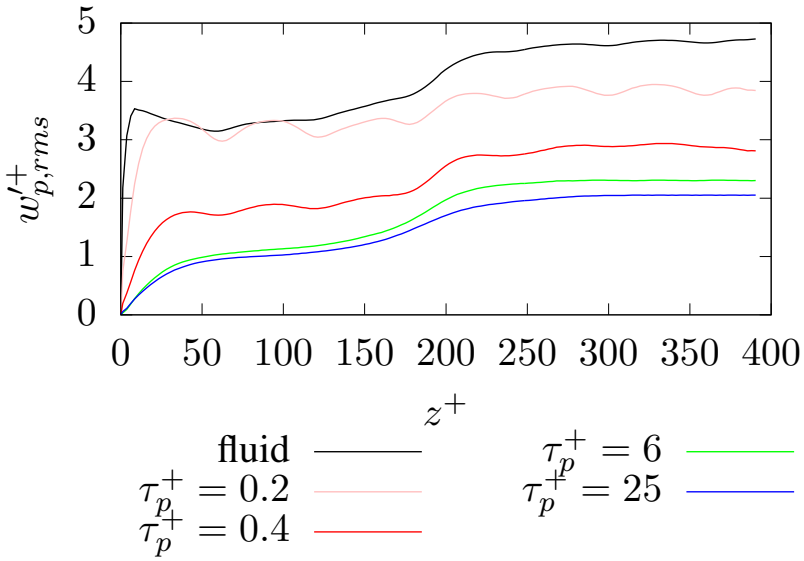

Figure 4.12 – Fluctuating particle wall normal velocity along the wall normal direction for Stokes number ($\tau_p{}^+ = 0.2; 0.4; 6; 25$).

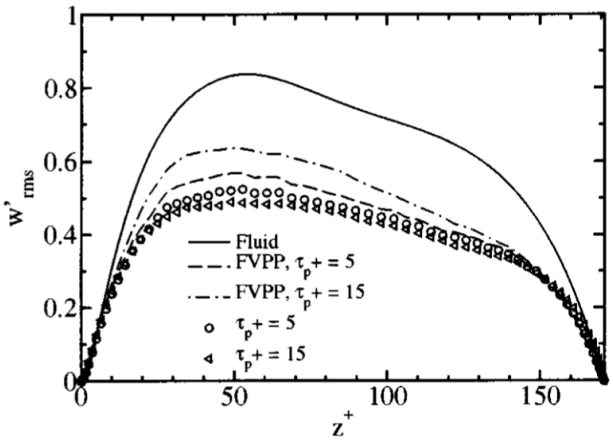

Figure 4.13 – Particle-phase turbulence intensity in wall-normal direction from Narayanan et al. [35].

Figure 4.14 reports the wall normal velocity evolution with time and the trajectory of a single particle which finally deposits, for each Stokes numbers from the same set as in Figure 4.12. It can be observed that as Stokes number decreases, residence time of aerosols in the boundary layer strongly increases. For low inertia particles (${\tau_p}^+ = 0.2; 0.4$), the wall-normal velocity remains very small during a long period of time corresponding to its stagnation in the accumulation region ($z^+ \leq 3$). It explains why the concentration of particles in the accumulation region is much higher for low inertia particles than for high inertia. In other words, the trajectories show how inertial particles do not linger very close to the wall and are directly transported and deposited following the free flight mechanism, while lower inertia particles remain for a longer time close to the wall before finally depositing. Furthermore, the trajectories of particles (${\tau_p}^+ \leq 6$) illustrate the particle boundary conditions applied at $y = 0$ and $y = L_y$; that is particles reaching $y = L_y$ are reintroduced back at $y = 0$ (x and z positions being obviously conserved).

Values of the instantaneous particulate Reynolds number have been retrieved from the simulation. Such a dimensionless number is defined as:

$$Re_p = \frac{\rho_f \, d_p \, ||\vec{u_p} - \vec{u_f}||}{\mu_f} \tag{4.63}$$

The value of particulate Reynolds number* range between 0 and 0.03 and confirm the relevance of the Stokes flow regime around the particles, especially important for drag coefficient calculation.

Due to turbulent flow structures at the wall, particles form deposition pattern on the wall that can be observed by recording the location where particles deposit. Particles deposition pattern at the wall over a certain period of time is shown in Figure 4.15, for Stokes number ${\tau_p}^+ = 25$ and ${\tau_p}^+ = 6$ and it can be observed that particles preferentially deposit as streamwise oriented streaks. Figures 4.15(a) and (b) are obtained by calculating particle deposition over a sampling time period of $5\tau^+$. The particles present in the streamwise streaks, tends to remain for a longer time because of the very small streamwise velocity

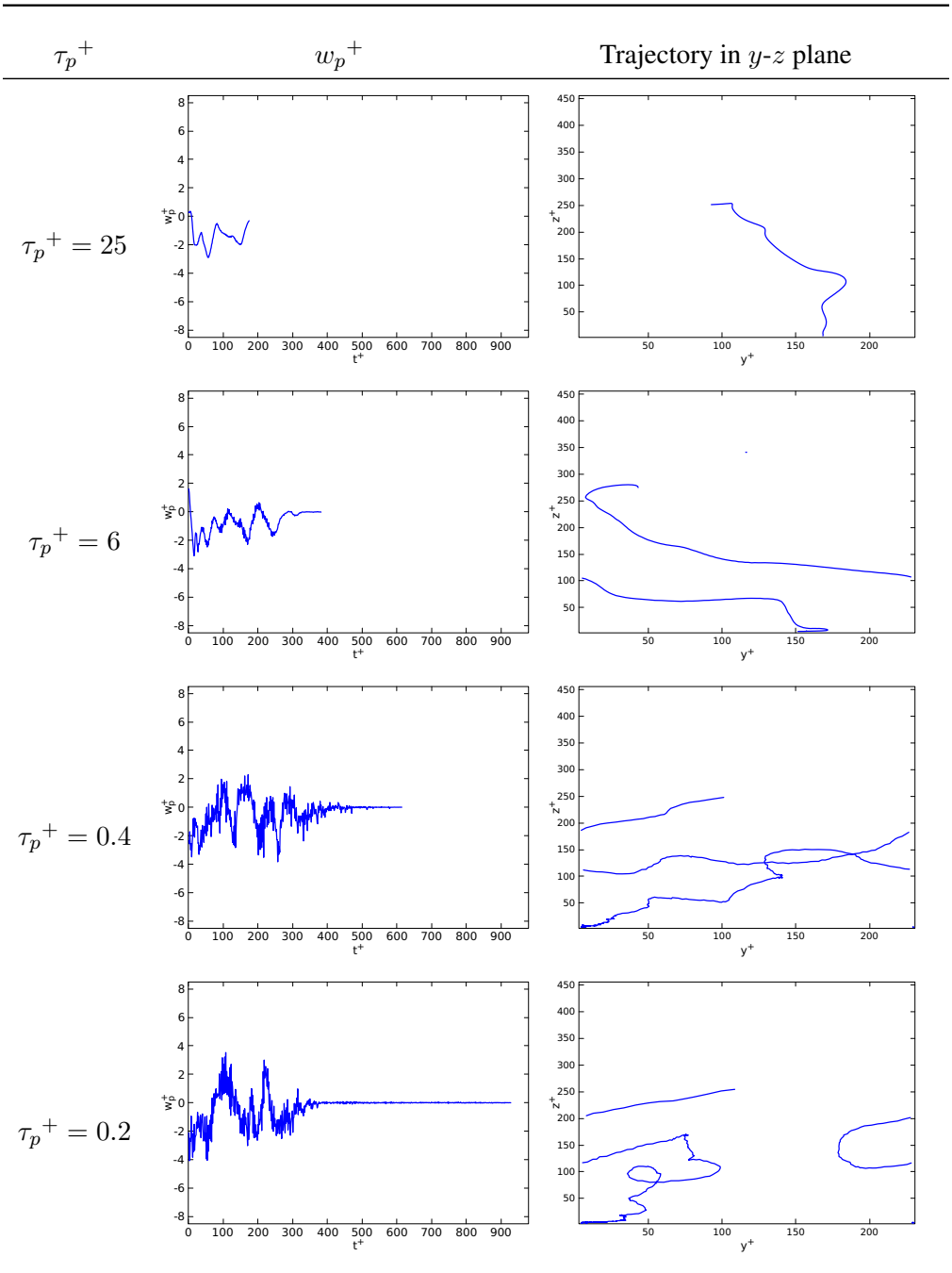

Figure 4.14 – Examples of trajectory and wall-normal velocity of aerosols for four different Stokes numbers ($\tau_p{}^+ = 0.2; 0.4; 6; 25$).

close to the wall. Thereby, as Narayanan et al. [35] clearly stated before, these deposition patterns reflect the distribution of particles in the accumulation zone.

As observed in the Figures 4.15, three streaks can be observed for the given domain size. Comparing the deposition pattern between Figure 4.15(a) and 4.15(b), it can be observed that greater inertia results in higher density of the deposition pattern on the wall, thus leading to higher deposition rate. Also, particles tend to deposit in the region of low speed streaks.

Figure 4.16 represents the plot of the three components of drag force along wall normal

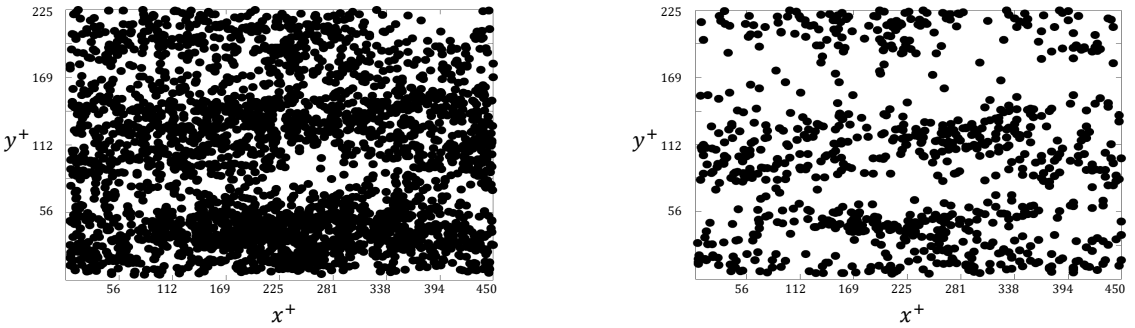

(a) $\tau_p{}^+ = 25$ (b) $\tau_p{}^+ = 6$

Figure 4.15 – Particle deposition patterns for high inertia particles

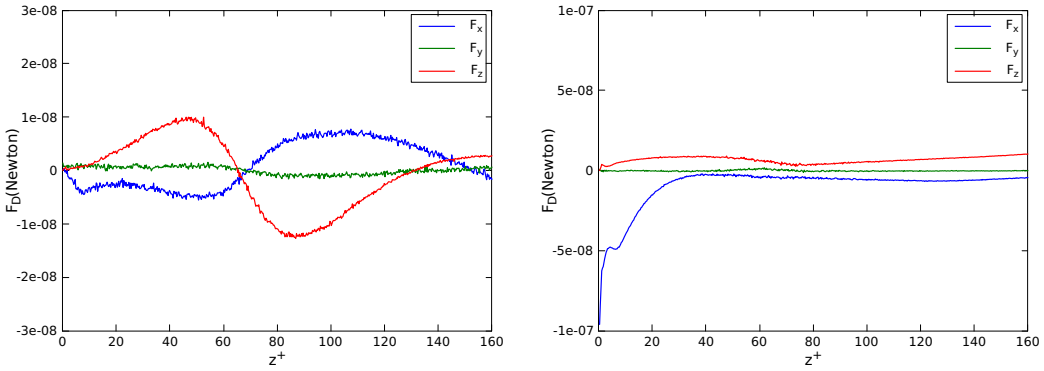

(a) (b)

Figure 4.16 – Evolution of streamwise, spanwise and wall normal components of drag force along wall normal direction for (a) $\tau_p{}^+ = 0.2$; (b) $\tau_p{}^+ = 25$

direction in the boundary layer. For $\tau_p{}^+ = 0.2$, the wall normal drag force (F_z in red) has a negative value while moving towards the wall till $z^+ = 65$ which means that particles are pushed towards the wall. This is due to the transportation by turbulence structures from the turbulent production region through the boundary layer. Closer to the wall, the force becomes positive, corresponding to a friction force which slows down the z component of the particle velocity as already shown previously (Figure 4.11). In this second region, particles are influenced by eddies which are taking them away from the wall. The force reaches a maximum positive value at $z^+ = 45$ before finally decreasing as particles move towards the wall and then becoming zero because fluid and particle z velocities reach zero values. Also lower inertia particles remain for a longer time close to the wall before finally depositing since the turbulent transport influences the motion of particles in a way that makes them accumulate in the near wall region.

Moving on to higher inertia $\tau_p{}^+ = 25$, the wall normal drag force (F_z) always remains positive in the boundary layer. The wall normal velocity of aerosols has a much larger

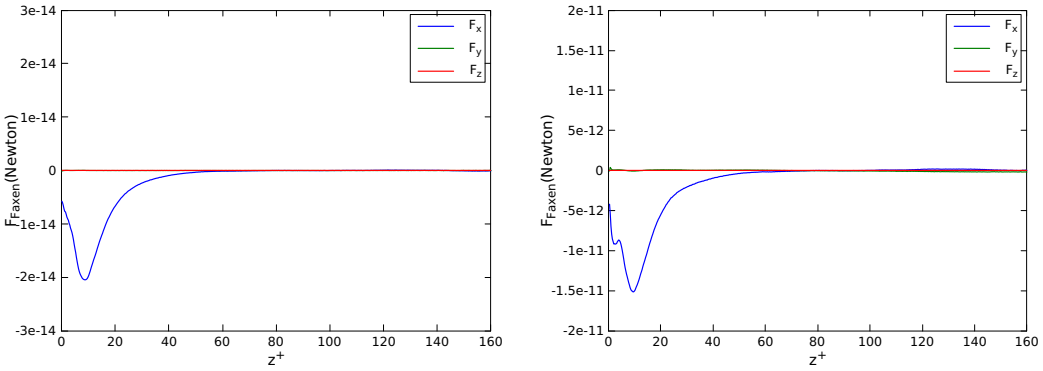

(a) (b)

Figure 4.17 – Evolution of streamwise, spanwise and wall normal components of Faxen correction force along wall normal direction for (a) ${\tau_p}^+ = 0.2$; (b) ${\tau_p}^+ = 25$

negative value than the z fluid component thus making the drag force positive. The trend of the wall-normal drag force (red curve) as seen in Figure 4.16(b) reveals a minimum of F_z around $z^+ = 70$.

All the simulations in this chapter have been performed without the additional Faxen correction with the aim of easing comparison with the literature data (where the Faxen correction was ommited). However, we have calculated this Faxen correction based on the fluid flow, and its profiles are presented in Figure 4.17. It obviously confirms that due to the much smaller values of Faxen correction as compared to the drag force, it will not play a significant role in the deposition and capture mechanisms of aerosols.

4.6.6 Simulation of hydrosols

To perform numerical simulation for determining the deposition mechanism of hydrosols was the main objective of the thesis but there were some difficulties to perform it. The main goal was to perform simulations in the larger domain as mentioned in section 3.5 in chapter 3 as we were able to observe more streaks and get better guaranties that such flow structures are not too constrained by the periodicity of the simulation domain. But due to the lack of computational time, it was rather difficult to study the deposition rate in the larger domain. Henceforth smaller domain was used for the initial investigation of hydrosol deposition. Only a first set of simulations have been performed and reported in Appendix A, being preliminary information.

Conclusions and perspectives

The major challenge in metallurgical processes is driven by weight reduction and consequently improvement of mechanical properties which depends on proper inclusion cleanliness. The inclusion population is controlled during ladle furnace processes upstream from solidification. A way to recover inclusions from the liquid bath is through their capture at the ladle walls and at the slag interface. Henceforth the main objective of the thesis was to develop numerical modelling to investigate turbulent deposition and capture of particles on the wall of the ladle furnace. The study of deposition and capture mechanisms must lead to the prediction of the deposition velocity.

A 3D numerical tool was developed to study the mesoscopic behavior of particle dynamics in a fully developed turbulent flow. The aforementioned mesoscopic scale simulations are performed using in-house software based on a Lattice Boltzmann Method (LBM) to solve the flow dynamics, in which a linear isotropic forcing generates artificial turbulence. Lagrangian particle tracking of inclusions is used to achieve the one way coupling between inclusion motion and the transient flow field.

The aim of the first step of this work was to generate DNS of turbulence through linear isotropic forcing. The simulation results have clearly shown that the physical linear forcing scheme used for the production of homogeneous turbulence conditions can be combined with the lattice-Boltzmann scheme in the software. The evaluated turbulent properties such as the turbulent dissipation rate and the kinetic energy achieve statistically stationary state. Also the integral length scale reaches 20% of the domain size thus allowing a ratio between large and small scales that is large enough to represent the inertial subrange of the turbulence energy spectrum. Such spectra showed an accurate cascade of energy from larger scales to smaller scales that matches Kolmogorov's $-5/3$ slope. Unrealistic physical behavior were only observed when the flow was knowingly under-resolved. Also our simulations were validated with the work performed by Valiño et al. [143], by comparing turbulent properties of the flow.

After DNS of isotropic turbulence, the second step was to produce fully developed 3D DNS of wall bounded turbulence. The originality of these simulations stems from the two different sources of turbulence combining in the boundary layer, the first is due to the diffusion of the isotropic turbulence maintained in the outer layer and the second generated by the wall shear stress. Simulations were performed both for smaller domain and larger domain which differ by their number of fluid nodes, that is ($N_x \times N_y \times N_z = 160 \times 80 \times 160$) LBM nodes and ($N_x \times N_y \times N_z = 720 \times 240 \times 240$) LBM nodes respectively. Simulation performed for smaller domain emphasized that the turbulence log-law profile

was in good agreement with the one from the literature [88, 125]. Furthermore simulations were performed for larger domain where three cases were considered: no forcing, forcing with $\gtrapprox 20\%$ and $\gtrapprox 10\%$ turbulence intensity.

The results obtained for no forcing turbulence for streamwise mean and fluctuation velocities were compared with the plots of [125], and good agreement of the results were visualized. Also isocontours of second invariant of velocity gradient tensor revealed the low and high speed streaks formed in the viscous sublayer region. The streamwise velocity color map for different streamwise locations showed that the wall shear generates eddies which swirls around the streamwise and spanwise directions and the isotropy of the eddies is obtained in regions far from the wall.

Concerning the two simulations with turbulence forcing, the plots for mean velocity and RMS of fluctuation velocity were in good agreement with those obtained by Moser et al. [125] close to the wall (till $z^+ = 100$). We noticed a non-physical steep jump at the interface for RMS of fluctuation velocity because a longer time averaging was used in the boundary layer region compared to turbulence forcing. This leads to proper calculation of turbulence properties close to the wall. The streamwise velocity maps and vectors along with isocontour maps show that streaks are formed in the same way as described in the literature on channel flows. Similarly, the streamwise velocity maps at different streamwise locations show eddies swirling around the streamwise and spanwise directions, thus proving the formation of streaks and other horseshoe-like structures.

The third step of this study has consisted in evaluating particle deposition rate for particles in a turbulent flow. As a question of time availability the main part of this work was devoted to aerosols, but the simulation of hydrosols (i.e. inclusions in liquid metal for representative flow conditions prevailing in a ladle furnace) have been initiated. Firstly, the dynamic behaviour of tracers is studied, and we obviously found that the tracer concentration is perfectly homogeneous throughout the domain when the turbulence is fully developed and that the tracer deposition rate is null. Next the simulation of aerosol deposition allowed us to calculate the deposition velocity as a function of the Stokes number. The deposition velocity increases with inertia till it levels off.

We clearly observed an accumulation of particles close to the wall ($z^+ < 3$) as stated by many authors [34, 35], and the peak of particle concentration increases when the particle inertia decreases. This is readily explained by the wall-normal velocity and RMS fluctuation velocity damping when the inertia of particles is small (such as ${\tau^+}_p = 0.4 \; or \; 0.2$), thus leading to the capture of aerosols by turbulence scales close to the wall. Finally, the deposition patterns highlighted streak shapes and confirmed that higher the inertia, higher the deposition rate.

The drag forces plot for higher inertia revealed positive values along the wall-normal distance to the wall, meaning that the particles continuously slow down when approaching the wall. But for lower inertia particles, the drag force has a negative value at some distance from the wall ($z^+ > 70$), thus accelerating particles towards the wall. Closer to the wall ($z^+ < 70$), low inertia particles decelerate because of positive values of the drag.

Some future perspectives that would valuably complete this work are listed as follows:

1. One of the objective of the PhD was to study the deposition mechanism of hydrosol

which are representative of inclusions in a metallurgical reactor. As observed in Appendix A, preliminary results were obtained for hydrosols where the effect of forces like drag, added mass, pressure gradient and lift close to the wall was studied. These simulations were performed for the smaller domain due to lack of time availability. From the first results obtained, only very little information could be extracted regarding the effect of various forces and finally obtaining the deposition rate. In the future, simulations can be performed in the same smaller domain in hydrosol conditions, by taking cases which relates to different particle-fluid density ratio and particle diameters as can be seen for inclusions in a liquid metal bath. A more vivid study can be done so as to extract more important and effective results concerning the effect of the forces leading to the deposition. As we have seen for aerosol deposition, wall bounded streaks play an important role, same can be expected for hydrosol deposition. Finally the deposition velocity can be evaluated by taking the ratio of the flux of particles depositing on the wall to the bulk concentration of particles as done for aerosols.

2. After getting a general idea about the effect of forces and deposition rate in a smaller domain, eventually larger domain can be simulated which provides better representation of wall bounded streaks as compared to smaller domain. A 3D DNS of the wall bounded turbulence in a larger domain has already been generated during the PhD and necessary validations have been performed with comparison to the corresponding literature. So, future prospects lie on introducing hydrosols in the larger domain and carry on the simulations. Various density ratios and particle diameters can be considered and finally the relative effect of each force close to the wall can be studied along with the deposition rate. Due to the better visualization of the wall bounded streaks close to the wall, deposition patterns could thus be accurately studied. Henceforth deposition mechanism can be analyzed and quantified into a statistical law for deposition velocity in terms of particle and flow properties such as Stokes number and particle-fluid density ratio.

3. The above mentioned perspectives can only be helpful in studying deposition mechanism for inclusions smaller than the smallest turbulent length scale present in the liquid metal bath. But in a liquid metal bath there can be inclusions larger than the smallest turbulent scales present in the vicinity of walls. In such conditions, modelling particles as mass points and weak coupling with the liquid phase will not capture accurate particle dynamics. Particles will then need be fully resolved and fully coupled with the liquid flow. To do that, Immersed Boundary Method (IBM) can be used which is already implemented in the in-house code FLUA. Future investigations dealing with such resolved particles would first require proper parallelization and MPI communication between periodic and pseudo-periodic boundary conditions, which is not yet fully implemented in this code. The statistical law for the deposition rate could thus be evaluated, which would help in quantifying deposition mechanisms of inclusions on ladle walls.

4. After obtaining the deposition velocity expression, preferably for both point and re-

solved particles, the longer term objective of such research it to provide statistical deposition models for macroscopic simulations such as the ones used in process scale simulations, where inclusion behavior is coupled with CFD through population balance equation. Feeding such simulations with deposition models accurately parameterized with local turbulence properties and particle properties would greatly improve the reliability and accuracy of process scale models. The results of deposition kinetics obtained from larger scale models is necessary to improve the control of inclusion recovery and consequently inclusion cleanliness in industrial processes.

Appendix A : Hydrosol deposition

Contents

In Chapter 4, section 4.6, results have been provided for aerosol particles depositing on a wall in a turbulent boundary layer and thereby compared and validated against the literature about aerosols. This appendix now covers simulations that have been initiated for hydrosol particles in fully developed wall bounded turbulence. First results include the effect of different forces acting on inclusion-like particles as presented in details in Chapter 4. The final goal of such studies would be to derive deposition velocity and also particle concentration close to the wall to quantify inclusion deposition and capture. However, simulations performed for hydrosol in this PhD work are quite recent, so discussion and analysis are unfortunately limited. Some focus is given to the impact on interpolation schemes on the

Table A.1 – Physical properties and turbulent flow conditions used for hydrosol simulation

Fluid properties	
ρ_f (kg m^{-3})	7000
μ_f (kg m^{-1} s^{-1})	5.5×10^{-3}
η_f (µm)	40
$\mathbf{T}_w$ (Pa)	2.2
ϵ (m^2 s^{-3})	0.2 *
$u_{\mathbf{T}}$ (m s^{-1})	0.0177 *
	* *dependent parameters*
Domain size and numerical conditions	
$L_x \times L_y \times L_z$ (mm^3)	$20 \times 10 \times 20$
$N_x \times N_y \times N_z$	$160 \times 80 \times 160$
$\Delta t_p(LBM)$ ([tu])	1
Total sampling time (t^+_{sam})	100 τ^+
Number of bins	1600
Particle conditions	
ρ_p/ρ_f	0.5
d_p (µm)	4.4
${d_p}^+$	0.1
${\tau_p}^+$	0.005
Initial number of particles	400000

results by comparing two interpolation schemes: trilinear and cubic spline.

A.1 Simulation parameters and geometry

The important physical and numerical parameters are listed in Table A.1. The simulation domain that was used for hydrosol simulations is taken to be the smaller domain introduced in Chapter 3 which has a number of LBM fluid nodes of $N_x \times N_y \times N_y = 160 \times 80 \times 160$. This is the same domain that was also taken for aerosol deposition as described in section 4.6. Similar to aerosol simulation, the domain is divided into two subdomains where the particles are initially introduced equidistantly from each other along the three directions in the turbulence production region. Boundary conditions are kept periodic for both fluid and particles along the streamwise and spanwise directions. Along the wall normal direction, opposite to the wall boundary condition itself, the same pseudo-periodic boundary condition is applied as mentioned in sections 4.5 and 4.6 in Chapter 4. This ensures a constant total number of particles that helps keeping constant the concentration profile of inclusions in the simulation domain throughout the simulation duration.

Moving from aerosol simulation corresponding to gas for the fluid phase to hydrosol simulation representing liquid steel, physical parameters such as density and viscosity change. Hence flow conditions to simulate hydrosol deposition also change. The imposed shear stress in the simulation happens to be the same for both gas and liquid steel simulations, but now due to the change in kinematic viscosity, the physical duration of a simulation time step is very different between both cases. This results in a different shear stress parameter in LBM units. Figure A.1 shows the evolution of the RMS of fluctuating velocity along the wall normal direction and it clearly shows that there is an increase in the fluctuating velocity close to the wall as observed in the literature. Then the velocity decreases before attaining a plateau and then increasing again before reaching the turbulence production region, where it is fairly constant as imposed by the linear forcing scheme. This same kind of profile was also observed in DNS of gas flow. In Figure A.1(b), the same plot is provided in physical units and it can be seen that the range of the obtained values are comparable with the values obtained by RANS simulations that were plotted in Figure 1.7. The plot of the dimensionless mean velocity profile provided in Figure A.2(a) once again shows that the logarithmic law of wall profile can be observed in our simulations, which is a signature of wall bounded turbulence that proves that the boundary layer behaviour is properly captured in the simulation.

Physical properties such as density and kinematic viscosity are taken as those of liquid steel to mimic physical conditions in a metallurgical reactor. Since hydrosols are modelled as inertial point particles, their size is taken to be smaller than the Kolmogorov length scale. The simulation is restricted to 4.4 µm diameter inclusions with a density of $3500\ kg\ m^{-3}$. The forces that are applied on particles are the drag along with Faxen correction, added mass, pressure gradient and the slip-shear lift forces.

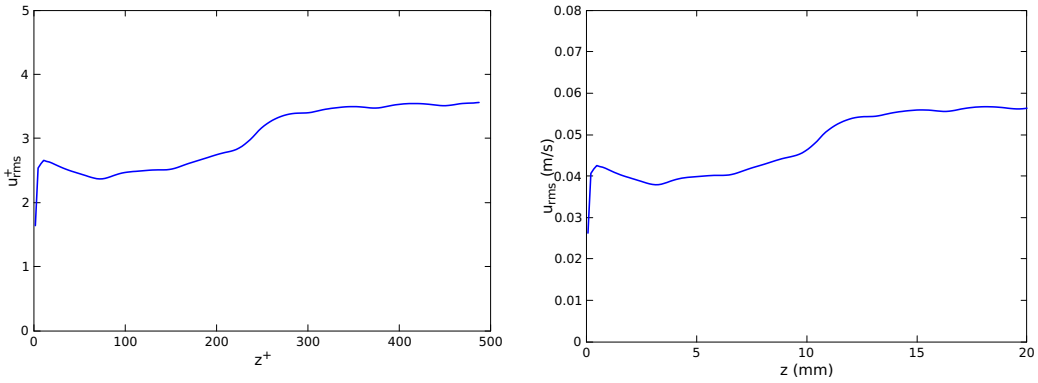

(a) (b)

Figure A.1 – RMS of the fluctuation velocity from the DNS simulation in (a) dimensionless units and (b) physical units

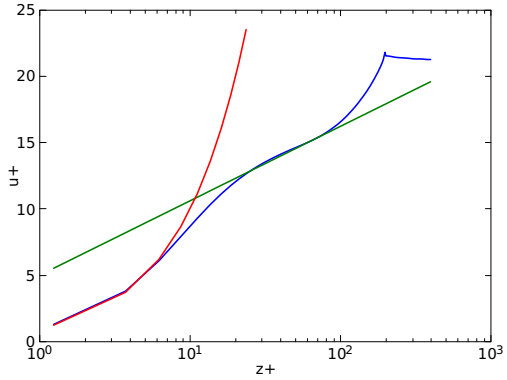

Figure A.2 – Mean velocity from the DNS simulation in dimensionless units.

A.2 Simulation results for deposition of hydrosol particles

A key objective of such simulations is to quantify the role played in deposition by the different forces close to the wall like the drag with Faxen correction, added mass, pressure gradient and shear lift forces. First, a trilinear interpolation scheme was used, as described in section 4.1 from Chapter 4.

Figure A.3 represents the preliminary results of the contribution of the forces along the wall normal direction. It shows clear oscillation patterns in force profiles, especially for the added mass force, in Figure A.3(c). We observed that such oscillations were caused by inaccurate computation of the fluid acceleration term in the added-mass force and that such inaccuracy was due to the low order interpolation scheme. This interpolation scheme is the one that is used for estimating at the particle location the fluid properties that are calculated at fluid nodes (such as partial time derivative of velocity and velocity gradient). Consequently, cubic spline interpolation was used in a second batch of simulations to plot the forces. This issue did not exist in aerosol simulations were particle dynamics do not depend explicitly on local fluid acceleration. Obviously, moving from an interpolation function

over two fluid nodes to 4 has severe impact on simulation performance, making hydrosol simulations require longer computation times. It can be clearly observed from Figure A.4(c) that the added mass force is much smoother and that the clearly visible oscillations from Figure A.3(c) have disappeared. However, the remaining random noise on the curves of the drag and pressure gradient forces is mainly due to the too short of sampling time needed to perform time average for obtaining statistical profiles.

With cubic interpolation, the trends highlighted by the drag force plot from Figure A.4(a) are very similar to the evolution of the drag forces along the wall normal direction described in Figure 4.16(a) for aerosol conditions, even the force magnitude is comparable between these two very different particle-fluid systems. The wall normal drag force is negative while moving towards the wall which means that particles are pushed and accelerated towards the wall by turbulence transport. Close to the wall, the force becomes positive as particles are slowed down by friction with the liquid phase.

Less expectedly, other forces like shear-lift, added mass and pressure gradient, obtained from the DNS are nearly four, six and five orders of magnitude lower than the drag force, which means that drag force is the prevailing force driving the motion of particles, just as observed for aerosols. For the added mass and pressure gradient forces, close to the wall a sudden positive peak can be seen, which, in cases when such forces are non-negligible, would require special care to keep sufficient interpolation order at the boundary condition. Nonetheless, deposition can be noticed as the simulation proceeds thus confirming capture of hydrosol particles.

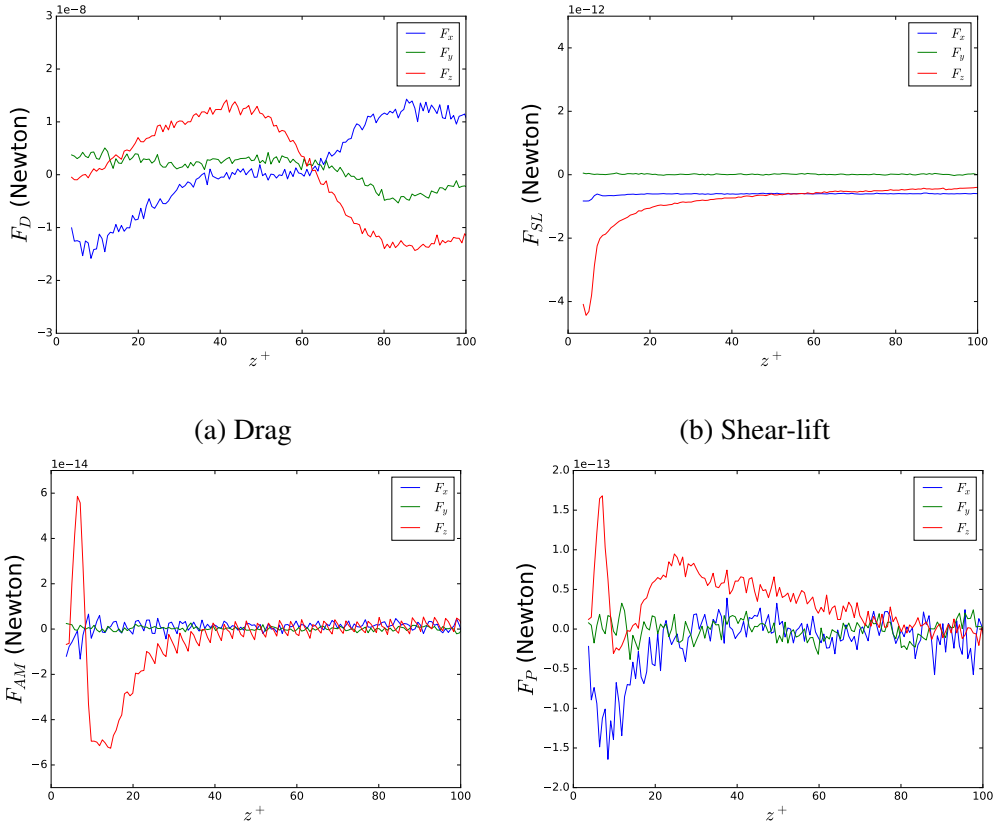

(a) Drag

(b) Shear-lift

(c) Added mass

(d) Pressure gradient

Figure A.3 – Evolution of forces acting particles along the wall normal direction, using linear interpolation for fluid properties at particle position.

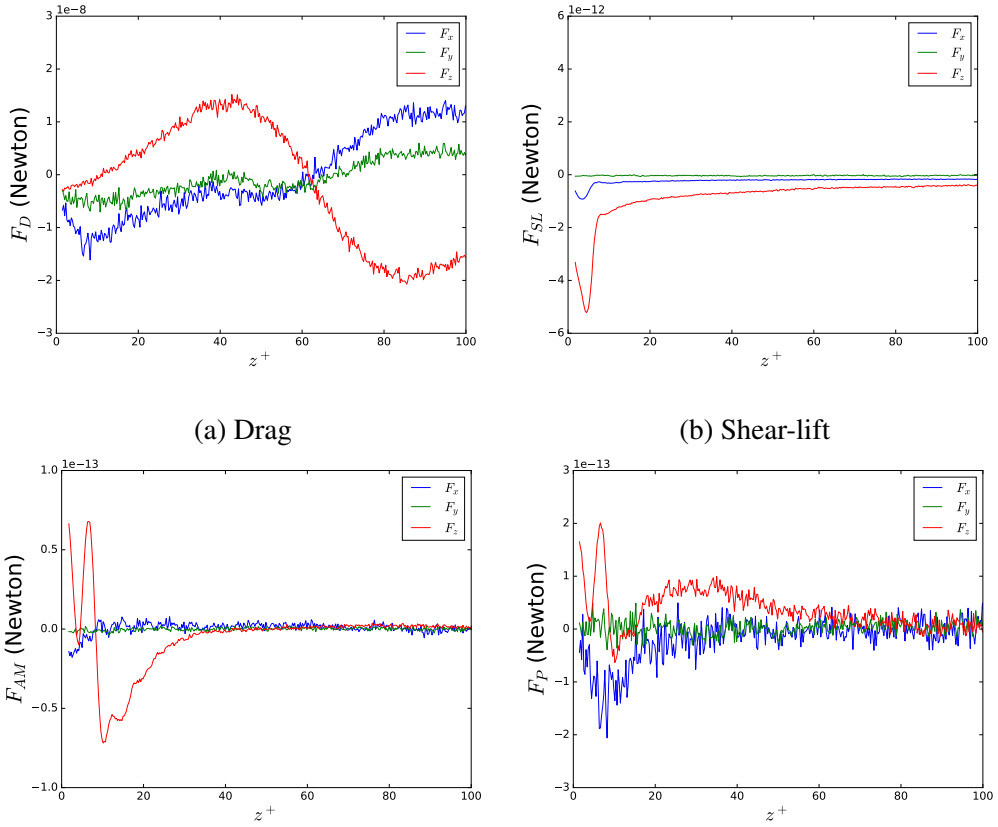

(a) Drag

(b) Shear-lift

(c) Added mass

(d) Pressure gradient

Figure A.4 – Evolution of forces acting particles along the wall normal direction, using cubic spline interpolation for fluid properties at particle position.

List of Tables

List of Figures

Bibliography

[1] J. Eggels and J. Somers. Numerical simulation of free convective flow using the lattice-boltzmann scheme. *International Journal of Heat and Fluid Flow*, 16(5): 357–364, 1995.

[2] P. L. Bhatnagar, E. P. Gross, and M. Krook. A model for collision processes in gases. I. Small amplitude processes in charged and neutral one-component systems. *Physical Review*, 94(3):511–525, 1954. ISSN 0031899X. doi: 10.1103/PhysRev.94.511.

[3] World steel in figures 2018 now available, website of the worldsteel association. May 2018.

[4] A European Steel Industrial Renaissance Domenico ROSSETTI di VALDALBERO and Bogdan European Commission – DG RTD Unit D4 Coal and Steel Paper for the 10 th International Conference on CLEAN STEEL 18-20 September 2018. pages 1–7, 2018.

[5] L. Zhang and B. G. Thomas. State of the art in evaluation and control of steel cleanliness. *ISIJ international*, 43(3):271–291, 2003.

[6] L.-f. ZHANG, Y.-l. LI, and Y. REN. Fundamentals of non-metallic inclusions in steel: Part 2. evaluation method of inclusions and thermodynamics of steel deoxidation. *Iron & Steel*, (12):1, 2013.

[7] V. De Felice, I. L. A. Daoud, B. Dussoubs, A. Jardy, and J.-P. Bellot. Numerical modelling of inclusion behaviour in a gas-stirred ladle. *ISIJ international*, 52(7): 1273–1280, 2012.

[8] E. C. Cedeno. Study of calcium cored wire injection in an industrial steel ladle. 2019.

[9] Z. Liu, L. Li, and B. Li. Modeling of gas-steel-slag three-phase flow in ladle metallurgy: Part i. physical modeling. *ISIJ International*, 57(11):1971–1979, 2017.

[10] R. Guthrie. Engineering in process metallurgy (oxford science publications). 1989.

[11] T. Emi, M. Suzukl, H. Yin, and H. Shibata. Agglomeration of Various Inclusion Pa rticles on Molten Steel Surf ace mm. 37(10):946–955, 1997.

[12] E.-I. Castro-Cedeño, M. Herrera-Trejo, M. Castro-Román, F. Castro-Uresti, and M. López-Cornejo. Evaluation of steel cleanliness in a steel deoxidized using al. *Metallurgical and Materials Transactions B*, 47(3):1613–1625, 2016.

[13] J.-P. Bellot, V. Descotes, and A. Jardy. Numerical modeling of inclusion behavior in liquid metal processing. *JOM*, 65(9):1164–1172, 2013.

[14] J.-P. Bellot, V. De Felice, B. Dussoubs, A. Jardy, and S. Hans. Coupling of cfd and pbe calculations to simulate the behavior of an inclusion population in a gas-stirring ladle. *Metallurgical and Materials Transactions B*, 45(1):13–21, 2014.

[15] F.-G. Fan and G. Ahmadi. Analysis of particle motion in the near-wall shear layer vortices—application to the turbulent deposition process. *Journal of colloid and interface science*, 172(2):263–277, 1995.

[16] L. Tian and G. Ahmadi. Particle deposition in turbulent duct flows—comparisons of different model predictions. *Journal of Aerosol Science*, 38(4):377–397, 2007.

[17] A. Guha. Transport and deposition of particles in turbulent and laminar flow. *Annu. Rev. Fluid Mech.*, 40:311–341, 2008.

[18] A. Mehel, A. Tanière, B. Oesterlé, and J.-R. Fontaine. The influence of an anisotropic langevin dispersion model on the prediction of micro-and nanoparticle deposition in wall-bounded turbulent flows. *Journal of Aerosol Science*, 41(8):729–744, 2010.

[19] M. Dupuy, A. Xayasenh, H. Duval, and E. Waz. Analysis of non-brownian particle deposition from turbulent liquid-flow. *AIChE Journal*, 62(3):891–904, 2016.

[20] A. Wells and A. Chamberlain. Transport of small particles to vertical surfaces. *British Journal of Applied Physics*, 18(12):1793, 1967.

[21] M. Reeks. The transport of discrete particles in inhomogeneous turbulence. *Journal of aerosol science*, 14(6):729–739, 1983.

[22] J. W. Brooke, T. Hanratty, and J. McLaughlin. Free-flight mixing and deposition of aerosols. *Physics of Fluids*, 6(10):3404–3415, 1994.

[23] C.-J. Tsai, J.-S. Lin, S. G. Aggarwal, and D.-R. Chen. Thermophoretic deposition of particles in laminar and turbulent tube flows. *Aerosol Science and Technology*, 38 (2):131–139, 2004.

[24] A. Mehel, B. Sagot, A. Tanière, and B. Oesterlé. On the mutual effect of the turbulent dispersion model and thermophoresis on nanoparticle deposition. *International Journal of Nonlinear Sciences and Numerical Simulation*, 13(6):417–425, 2012.

[25] S. Friedlander and H. Johnstone. Deposition of suspended particles from turbulent gas streams. *Industrial & Engineering Chemistry*, 49(7):1151–1156, 1957.

[26] B. Y. Liu and J. K. Agarwal. Experimental observation of aerosol deposition in turbulent flow. *Journal of Aerosol Science*, 5(2):145–155, 1974.

[27] N. Wood. A simple method for the calculation of turbulent deposition to smooth and rough surfaces. *Journal of aerosol Science*, 12(3):275–290, 1981.

[28] M. Rashidi, G. Hetsroni, and S. Banerjee. Particle-turbulence interaction in a boundary layer. *International Journal of Multiphase Flow*, 16(6):935–949, 1990.

[29] J. Cleaver and B. Yates. A sub layer model for the deposition of particles from a turbulent flow. *Chemical Engineering Science*, 30(8):983–992, 1975.

[30] J. B. McLaughlin. Aerosol particle deposition in numerically simulated channel flow. *Physics of Fluids A: Fluid Dynamics*, 1(7):1211–1224, 1989.

[31] J. W. Brooke, K. Kontomaris, T. Hanratty, and J. B. McLaughlin. Turbulent deposition and trapping of aerosols at a wall. *Physics of Fluids A: Fluid Dynamics*, 4(4): 825–834, 1992.

[32] C. Marchioli and A. Soldati. Mechanisms for particle transfer and segregation in a turbulent boundary layer. *Journal of fluid Mechanics*, 468:283–315, 2002.

[33] J. Yao, M. Fairweather, and Y. Zhao. Numerical simulation of particle deposition in turbulent duct flows. *Industrial & Engineering Chemistry Research*, 53(8):3329–3341, 2014.

[34] A. Soldati and C. Marchioli. Physics and modelling of turbulent particle deposition and entrainment: Review of a systematic study. *International Journal of Multiphase Flow*, 35(9):827–839, 2009.

[35] C. Narayanan, D. Lakehal, L. Botto, and A. Soldati. Mechanisms of particle deposition in a fully developed turbulent open channel flow. *Physics of Fluids*, 15(3): 763–775, 2003.

[36] S. Pirozzoli, M. Bernardini, and P. Orlandi. Turbulence statistics in couette flow at high reynolds number. *Journal of Fluid Mechanics*, 758:327–343, 2014.

[37] H. Lu and L.-z. Zhang. Particle deposition characteristics and efficiency in duct air flow over a backward-facing step: Analysis of influencing factors. *Sustainability*, 11 (3):751, 2019.

[38] F.-G. Fan and G. Ahmadi. A sublayer model for turbulent deposition of particles in vertical ducts with smooth and rough surfaces. *Journal of Aerosol Science*, 24(1): 45–64, 1993.

[39] L. Browne. Deposition of particles on rough surfaces during turbulent gas-flow in a pipe. *Atmospheric Environment (1967)*, 8(8):801–816, 1974.

[40] B. Arcen, A. Tanière, and B. Oesterlé. On the influence of near-wall forces in particle-laden channel flows. *International Journal of Multiphase Flow*, 32(12): 1326–1339, 2006.

[41] J. Boussinesq. Theorie de l'ecoulement tourbillonnant et tumultueux des liquides dans les lits rectilignes a grande section, gauthier-villars paris vol. 1. *Open Library OL7070543M*, 1897.

[42] O. Reynolds. Experiments showing the boiling of water in an open tube at ordinary temperatures. *Scientific Papers on Mechanical and Physical Subject*, 2:1900–1903, 1894.

[43] H. Poincaré. Sur le problème des trois corps et les équations de la dynamique. *Acta mathematica*, 13(1):A3–A270, 1890.

[44] E. N. Lorenz. Deterministic nonperiodic flow. *Journal of the atmospheric sciences*, 20(2):130–141, 1963.

[45] L. Prandtl. 7. bericht über untersuchungen zur ausgebildeten turbulenz. *ZAMM-Journal of Applied Mathematics and Mechanics/Zeitschrift für Angewandte Mathematik und Mechanik*, 5(2):136–139, 1925.

[46] G. I. Taylor. The spectrum of turbulence. *Proceedings of the Royal Society of London. Series A-Mathematical and Physical Sciences*, 164(919):476–490, 1938.

[47] A. N. Kolmogorov. The local structure of turbulence in incompressible viscous fluid for very large reynolds numbers. *Cr Acad. Sci. URSS*, 30:301–305, 1941.

[48] L. F. Richardson. Weather prediction by numerical process cambridge university press. *Cambridge Richardson Weather prediction by numerical process*, 1922, 1922.

[49] D. Ruelle and F. Takens. On the nature of turbulence. *Les rencontres physiciens-mathématiciens de Strasbourg-RCP25*, 12:1–44, 1971.

[50] H. Kim, S. Kline, and W. Reynolds. The production of turbulence near a smooth wall in a turbulent boundary layer. *Journal of Fluid Mechanics*, 50(1):133–160, 1971.

[51] P. A. Mantz. Bedforms produced by fine, cohesionless, granular and flakey sediments under subcritical water flows. *Sedimentology*, 25(1):83–103, 1978.

[52] H. T. Moon, P. Huerre, and L. Redekopp. Transitions to chaos in the ginzburg-landau equation. *Physica D: Nonlinear Phenomena*, 7(1-3):135–150, 1983.

[53] S. Thorpe. Transitional phenomena and the development of turbulence in stratified fluids: A review. *Journal of Geophysical Research: Oceans*, 92(C5):5231–5248, 1987.

[54] J. W. Deardorff. A numerical study of three-dimensional turbulent channel flow at large reynolds numbers. *Journal of Fluid Mechanics*, 41(2):453–480, 1970.

[55] S. A. Orszag and G. Patterson Jr. Numerical simulation of three-dimensional homogeneous isotropic turbulence. *Physical Review Letters*, 28(2):76, 1972.

[56] B. E. Launder and D. B. Spalding. *Mathematical models of turbulence*. Number BOOK. Academic press, 1972.

[57] J. Jiménez. Turbulence Structure and Vortex Dynamics. *European Journal of Mechanics - B/Fluids*, 20(5):746–747, 2001. ISSN 09977546. doi: 10.1016/S0997-7546(01)01149-9. URL http://linkinghub.elsevier.com/retrieve/pii/S0997754601011499.

[58] E. D. Siggia and G. Patterson. Intermittency effects in a numerical simulation of stationary three-dimensional turbulence. *Journal of Fluid Mechanics*, 86(3):567–592, 1978.

[59] T. S. Lundgren. Linearly forced isotropic turbulence. *Annual Research Briefs*, (2): 461–473, 2003.

[60] C. Rosales and C. Meneveau. Linear forcing in numerical simulations of isotropic turbulence: Physical space Implementations and convergence properties. *Physics of Fluids*, 17(9):1–8, 2005. ISSN 10706631. doi: 10.1063/1.2047568.

[61] T. Ishihara and Y. Kaneda. High resolution DNS of incompressible homogeneous forced turbulence: time dependence of the statistics. *Statistical Theories and Computational Approaches to Turbulence*, (January 2003): 177–188, 2003. doi: 10.1007/978-4-431-67002-5_11. URL http://link.springer.com/10.1007/978-4-431-67002-5{%}5Cnhttp://link.springer.com/10.1007/978-4-431-67002-5{_}11.

[62] J. Jiménez, A. A. Wray, P. G. Saffman, and R. S. Rogallo. The structure of intense vorticity in isotropic turbulence. *Journal of Fluid Mechanics*, 255:65–90, 1993. ISSN 0022-1120. doi: 10.1017/S0022112093002393. URL http://www.journals.cambridge.org/abstract{_}S0022112093002393.

[63] A. G. Lamorgese, D. A. Caughey, and S. B. Pope. Direct numerical simulation of homogeneous turbulence with hyperviscosity. *Physics of Fluids*, 17(1):1–10, 2005. ISSN 10706631. doi: 10.1063/1.1833415.

[64] K. Mohseni, B. Kosović, S. Shkoller, and J. E. Marsden. Numerical simulations of the Lagrangian averaged Navier-Stokes equations for homogeneous isotropic turbulence. *Physics of Fluids*, 15(2):524–544, 2003. ISSN 10706631. doi: 10.1063/1.1533069.

[65] S. Ghosal, T. S. Lund, P. Moin, and K. Akselvoll. A dynamic localization model for large-eddy simulation of turbulent flows, 1995. ISSN 0022-1120. URL http://www.journals.cambridge.org/abstract{_}S0022112095000711.

[66] D. Carati, D. Carati, S. Ghosal, S. Ghosal, P. Moin, and P. Moin. On the representation of backscatter in dynamic localization models. *Physics of Fluids*, 7(1995):606, 1995. ISSN 10706631. doi: 10.1063/1.868585. URL http://link.aip.org/link/PHFLE6/v7/i3/p606/s1{&}Agg=doi.

[67] N. P. Sullivan, S. Mahalingam, and R. M. Kerr. Deterministic forcing of homogeneous, isotropic turbulence. *Physics of Fluids*, 6(1994):1612, 1994. ISSN 10706631. doi: 10.1063/1.868274. URL `http://link.aip.org/link/PHFLE6/v6/i4/p1612/s1{&}Agg=doi`.

[68] C. Seror, P. Sagaut, C. Bailly, and D. Juv?? On the radiated noise computed by large-eddy simulation. *Physics of Fluids*, 13(2):476–487, 2001. ISSN 10706631. doi: 10.1063/1.1336150.

[69] L.-P. Wang, S. Chen, J. G. Brasseur, and J. C. Wyngaard. Examination of hypotheses in the kolmogorov refined turbulence theory through high-resolution simulations. part 1. velocity field. *Journal of Fluid Mechanics*, 309:113–156, 1996.

[70] S. Chapman. Vi. on the law of distribution of molecular velocities, and on the theory of viscosity and thermal conduction, in a non-uniform simple monatomic gas. *Philosophical Transactions of the Royal Society of London. Series A, Containing Papers of a Mathematical or Physical Character*, 216(538-548):279–348, 1916.

[71] D. Enskog. Kinetische theorie der vorgänge in mässig verdünnten gasen. 1917.

[72] F. Dubois. Une introduction au schéma de boltzmann sur réseau. In *ESAIM: proceedings*, volume 18, pages 181–215. EDP Sciences, 2007.

[73] S. Chen and G. D. Doolen. Lattice Boltzmann Method for Fluid Flows. *Http://Dx.Doi.Org/10.1146/Annurev.Fluid.30.1.329*, (Kadanoff 1986), 2003. ISSN 0066-4189. doi: 10.1146/annurev.fluid.30.1.329.

[74] D. D'Humières, I. Ginzburg, M. Krafczyk, P. Lallemand, and L.-S. Luo. Multiple-relaxation-time lattice Boltzmann models in three dimensions. *Philosophical transactions. Series A, Mathematical, physical, and engineering sciences*, 360(1792):437–451, 2002. ISSN 1364-503X. doi: 10.1098/rsta.2001.0955.

[75] A. ten Cate, E. van Vliet, J. J. Derksen, and H. E. A. V. den Akker. Application of spectral forcing in lattice-Boltzmann simulations of homogeneous turbulence. *Computers and Fluids*, 35(10):1239–1251, 2006. ISSN 00457930. doi: 10.1016/j.compfluid.2005.06.001.

[76] P. Moin and K. Mahesh. DIRECT NUMERICAL SIMULATION: A Tool in Turbulence Research. *Annual Review of Fluid Mechanics*, 30(1):539–578, 1998. ISSN 0066-4189. doi: 10.1146/annurev.fluid.30.1.539.

[77] L. Valiño, J. Martín, and G. Házi. Dynamics of isotropic homogeneous turbulence with linear forcing using a lattice boltzmann method. *Flow, Turbulence and Combustion*, 84(2):219–237, 2010. ISSN 13866184. doi: 10.1007/s10494-009-9222-2.

[78] M. Carbone and A. D. Bragg. Is vortex stretching the main cause of the turbulent energy cascade? *arXiv preprint arXiv:1906.07144*, 2019.

[79] D. Guszejnov, N. Lazányi, A. Bencze, and S. Zoletnik. On the effect of intermittency of turbulence on the parabolic relation between skewness and kurtosis in magnetized plasmas. *Physics of Plasmas*, 20(11):112305, 2013.

[80] K. Alvelius. Random forcing of three-dimensional homogeneous turbulence. *Physics of Fluids*, 11(7):1880, 1999. ISSN 10706631. doi: 10.1063/1.870050. URL `http://scitation.aip.org/content/aip/journal/pof2/11/7/10.1063/1.870050`.

[81] J. Kim, P. Moin, and R. Moser. Turbulence statistics in fully developed channel flow at low reynolds number. *Journal of fluid mechanics*, 177:133–166, 1987.

[82] S. K. Robinson. Coherent motions in the turbulent boundary layer. *Annual Review of Fluid Mechanics*, 23(1):601–639, 1991.

[83] S. Nakagawa, Y. Na, and T. Hanratty. Influence of a wavy boundary on turbulence. *Experiments in Fluids*, 35(5):422–436, 2003.

[84] J. M. Österlund. *Experimental studies of zero pressure-gradient turbulent boundary layer flow*. PhD thesis, Mekanik, 1999.

[85] A. J. Smits, B. J. McKeon, and I. Marusic. High–reynolds number wall turbulence. *Annual Review of Fluid Mechanics*, 43:353–375, 2011.

[86] S. Hoyas and J. Jiménez. Scaling of the velocity fluctuations in turbulent channels up to re_τ= 2003. *Physics of fluids*, 18(1):011702, 2006.

[87] P. Schlatter and R. Örlü. Assessment of direct numerical simulation data of turbulent boundary layers. *Journal of Fluid Mechanics*, 659:116–126, 2010.

[88] S. B. Pope. Turbulent flows, 2001.

[89] P. A. Monkewitz. Revisiting the quest for a universal log-law and the role of pressure gradient in "canonical" wall-bounded turbulent flows. *Physical Review Fluids*, 2(9): 094602, 2017.

[90] A. Townsend. *The structure of turbulent shear flow*. Cambridge university press, 1980.

[91] S. J. Kline, W. C. Reynolds, F. Schraub, and P. Runstadler. The structure of turbulent boundary layers. *Journal of Fluid Mechanics*, 30(4):741–773, 1967.

[92] A. Roshko. Structure of turbulent shear flows: a new look. *AIAA journal*, 14(10): 1349–1357, 1976.

[93] B. J. Cantwell. Organized motion in turbulent flow. *Annual review of fluid mechanics*, 13(1):457–515, 1981.

[94] J. Laufer. Deterministic and stochastic aspects of turbulence. *Journal of applied mechanics*, 50(4b):1079–1085, 1983.

[95] R. S. Rogallo and P. Moin. Numerical simulation of turbulent flows. *Annual review of fluid mechanics*, 16(1):99–137, 1984.

[96] F. R. Hama. *Boundary-layer transition induced by a vibrating ribbon on a flat plate*. University of Maryland, Institute for Fluid Dynamics and Applied Mathematics, 1960.

[97] L. Sirovich. Turbulence and the dynamics of coherent structures. i. coherent structures. *Quarterly of applied mathematics*, 45(3):561–571, 1987.

[98] J. Jeong, F. Hussain, W. Schoppa, and J. Kim. Coherent structures near the wall in a turbulent channel flow. *Journal of Fluid Mechanics*, 332:185–214, 1997.

[99] J. Jiménez. Coherent structures in wall-bounded turbulence. *Journal of Fluid Mechanics*, 842, 2018.

[100] A. F. Hussain. Coherent structures and turbulence. *Journal of Fluid Mechanics*, 173: 303–356, 1986.

[101] W. Reynolds and W. Tiederman. Stability of turbulent channel flow, with application to malkus's theory. *Journal of Fluid Mechanics*, 27(2):253–272, 1967.

[102] C. Smith and S. Metzler. The characteristics of low-speed streaks in the near-wall region of a turbulent boundary layer. *Journal of Fluid Mechanics*, 129:27–54, 1983.

[103] S. Chernyshenko and M. Baig. The mechanism of streak formation in near-wall turbulence. *Journal of Fluid Mechanics*, 544:99–131, 2005.

[104] N. Hutchins and I. Marusic. Evidence of very long meandering features in the logarithmic region of turbulent boundary layers. *Journal of Fluid Mechanics*, 579:1–28, 2007.

[105] T. Theodorsen. Mechanism of turbulence. *Proc. Midwest. Conf. Fluid Mech., Colombus, Ohio*, 2nd edition:1–18, 1952.

[106] D. J. Dennis. Coherent structures in wall-bounded turbulence. *Anais da Academia Brasileira de Ciências*, 87(2):1161–1193, 2015.

[107] C. Liu and P. Lu. DNS study on physics of late boundary layer transition. In *50th AIAA Aerospace Sciences Meeting Including the New Horizons Forum and Aerospace Exposition*, page 83, 2012.

[108] M. Guala, S. Hommema, and R. Adrian. Large-scale and very-large-scale motions in turbulent pipe flow. *Journal of Fluid Mechanics*, 554:521–542, 2006.

[109] R. F. Blackwelder and L. S. Kovasznay. Time scales and correlations in a turbulent boundary layer. *The Physics of Fluids*, 15(9):1545–1554, 1972.

[110] J. Murlis, H. Tsai, and P. Bradshaw. The structure of turbulent boundary layers at low reynolds numbers. *Journal of Fluid Mechanics*, 122:13–56, 1982.

[111] R. Falco. Coherent motions in the outer region of turbulent boundary layers. *The Physics of Fluids*, 20(10):S124–S132, 1977.

[112] R. J. Adrian. Hairpin vortex organization in wall turbulence. *Physics of Fluids*, 19 (4):041301, Apr. 2007. ISSN 1070-6631. doi: 10.1063/1.2717527. URL `http://aip.scitation.org/doi/10.1063/1.2717527`.

[113] S. Lu and W. Willmarth. Measurements of the structure of the reynolds stress in a turbulent boundary layer. *Journal of Fluid Mechanics*, 60(3):481–511, 1973.

[114] C. Tomkins and R. Adrian. Energetic spanwise modes in the logarithmic layer of a turbulent boundary layer. *Journal of Fluid Mechanics*, 545:141–162, 2005.

[115] M. Head and P. Bandyopadhyay. New aspects of turbulent boundary-layer structure. *Journal of Fluid Mechanics*, 107:297–338, 1981.

[116] N. Université de Lorraine. Explor. 2018.

[117] OpenMP Architecture Review Board. OpenMP application program interface version 4.5, 2015. URL `https://www.openmp.org/wp-content/uploads/openmp-4.5.pdf`.

[118] R. L. Graham, T. S. Woodall, and J. M. Squyres. Open mpi: A flexible high performance mpi. In *International Conference on Parallel Processing and Applied Mathematics*, pages 228–239. Springer, 2005.

[119] X. He and L.-S. Luo. Lattice boltzmann model for the incompressible navier–stokes equation. *Journal of statistical Physics*, 88(3-4):927–944, 1997.

[120] F. J. Alexander, H. Chen, S. Chen, and G. Doolen. Lattice boltzmann model for compressible fluids. *Physical Review A*, 46(4):1967, 1992.

[121] Q. Zou, S. Hou, S. Chen, and G. D. Doolen. A improved incompressible lattice boltzmann model for time-independent flows. *Journal of Statistical Physics*, 81(1-2):35–48, 1995.

[122] A. Zhou and J. Klewicki. Properties of the streamwise velocity fluctuations in the inertial layer of turbulent boundary layers and their connection to self-similar mean dynamics. *International Journal of Heat and Fluid Flow*, 51:372–382, 2015.

[123] F. Durst, E. Zanoun, and H. Nagib. The mean velocity profile of two-dimensional fully developed turbulent plane-channel flows. In *IUTAM Symposium on Reynolds Number Scaling in Turbulent Flow*, pages 129–136. Springer, 2004.

[124] D. Bespalko, A. Pollard, and M. Uddin. Direct numerical simulation of fully-developed turbulent channel flow using the lattice boltzmann method and analysis of openmp scalability. In *International Symposium on High Performance Computing Systems and Applications*, pages 1–19. Springer, 2009.

[125] R. D. Moser, J. Kim, and N. N. Mansour. Direct numerical simulation of turbulent channel flow up to re τ= 590. *Physics of fluids*, 11(4):943–945, 1999.

[126] J. Jiménez and P. Moin. The minimal flow unit in near-wall turbulence. *Journal of Fluid Mechanics*, 225:213–240, 1991.

[127] S. Heinz and H. Gopalan. Realizable versus non-realizable dynamic subgrid-scale stress models. *Physics of Fluids*, 24(11):115105, 2012.

[128] Y. Yamamoto, T. Kunugi, and A. Serizawa. Turbulence statistics and scalar transport in an open-channel flow. *Journal of Turbulence*, 2(10):1–16, 2001.

[129] A. Saxena, J.-S. Kroll-Rabotin, and R. S. Sanders. A numerical approach to model aggregate restructuring in shear flow using dem in lattice-boltzmann simulations. 2017.

[130] M. R. Maxey and J. J. Riley. Equation of motion for a small rigid sphere in a nonuniform flow. *The Physics of Fluids*, 26(4):883–889, 1983.

[131] F. Odar and W. S. Hamilton. Forces on a sphere accelerating in a viscous fluid. *Journal of Fluid Mechanics*, 18(2):302–314, 1964.

[132] J. Magnaudet, M. Rivero, and J. Fabre. Accelerated flows past a rigid sphere or a spherical bubble. part 1. steady straining flow. *Journal of Fluid Mechanics*, 284: 97–135, 1995.

[133] M. Sommerfeld. Theoretical and experimental modeling of particulate flows. Lecture Series 2000-06, Institut für Verfahrenstechnik Fachbereich Ingenieurwissenschaften Martin-Luther-Universität Halle-Wittenberg D-06099 Halle (Saale), Germany, 2000.

[134] P. Saffman. The lift on a small sphere in a slow shear flow. *Journal of fluid mechanics*, 22(2):385–400, 1965.

[135] L. Botto, C. Narayanan, M. Fulgosi, and D. Lakehal. Effect of near-wall turbulence enhancement on the mechanisms of particle deposition. *International journal of multiphase flow*, 31(8):940–956, 2005.

[136] S. Parker, T. Foat, and S. Preston. Towards quantitative prediction of aerosol deposition from turbulent flows. *Journal of Aerosol Science*, 39(2):99–112, 2008.

[137] A. Li and G. Ahmadi. Deposition of aerosols on surfaces in a turbulent channel flow. *International Journal of Engineering Science*, 31(3):435–451, 1993.

[138] P. W. Longest and M. Hindle. Quantitative analysis and design of a spray aerosol inhaler. part 1: effects of dilution air inlets and flow paths. *Journal of aerosol medicine and pulmonary drug delivery*, 22(3):271–283, 2009.

[139] G. Sharma and D. J. Phares. Turbulent transport of particles in a straight square duct. *International journal of multiphase flow*, 32(7):823–837, 2006.

[140] Y. Tang, B. Guo, and D. Ranjan. Numerical simulation of aerosol deposition from turbulent flows using three-dimensional rans and les turbulence models. *Engineering Applications of Computational Fluid Mechanics*, 9(1):174–186, 2015.

[141] I. Fouxon, L. Schmidt, P. Ditlevsen, M. van Reeuwijk, and M. Holzner. Inhomogeneous growth of fluctuations of concentration of inertial particles in channel turbulence. *Physical Review Fluids*, 3(6):064301, 2018.

[142] M. Bernardini. Reynolds number scaling of inertial particle statistics in turbulent channel flows. *Journal of Fluid Mechanics*, 758, 2014.

[143] L. Valiño, J. Martín, and G. Házi. Dynamics of isotropic homogeneous turbulence with linear forcing using a lattice boltzmann method. *Flow, turbulence and combustion*, 84(2):219, 2010.

Abstract

Deposition of particles on a wall plays a significant role in fluid-solid processes such as inclusions recovery from liquid steel in ladle furnace, that controls inclusion cleanliness upstream from solidification. The aim of this work is to study the turbulent deposition and capture of particles on a wall, in a situation where turbulence in the boundary layer originates both from wall shear and from agitation in the external flow. In a ladle furnace, such an agitation would result from bubble injection.

A framework for simulations at mesoscopic scale in which particles are represented as points but the turbulence is fully resolved has been developped using an in-house solver, where a Lattice Boltzmann Method (LBM) solves flow dynamics and linear isotropic forcing generates artificial turbulence. Lagrangian Particle Tracking (LPT) is used to achieve one way coupling between particle motions and turbulent flow. These numerical methods were applied to Direct Numerical simulation (DNS) of a fully developed turbulent boundary layer in which particles smaller than the Kolmogorov length scale are introduced. The deposition mechanisms in aerosol conditions have been analyzed and quantified into a statistical law for deposition velocity in terms of Stokes number, and validated against data from the literature.

Such simulations have provided a better understanding of deposition and capture mechanisms, depending on the turbulent flow in a wall boundary layer and on particle physical properties. Also, preliminary simulations in hydrosol conditions that match actual ladle operation have shown that the framework developed in this work can be applied to investigate inclusion behaviour in secondary steelmaking although statistical analysis in this work focused on aerosols.

Résumé

Le dépôt de particules sur une paroi joue un rôle significatif dans les procédés polyphasiques fluide-solides, tels que la séparation inclusionnaire dans les poches d'acier liquide en métallurgie secondaire qui permettent de contrôler la propreté du métal avant solidification. L'objectif de ce travail est d'étudier le dépôt turbulent et la capture de particules sur une paroi, dans des situations où la turbulence au sein de la couche limite est produite à la fois par la contrainte pariétale et par les forces d'agitation du bain liquide loin de cette paroi.

Les simulations sont mises en œuvre à l'échelle mésoscopique, en considérant des particules ponctuelles mais avec une turbulence complètement résolue. Un code de simulation maison a été développé, utilisant une méthode de Boltzmann sur réseau pour résoudre la dynamique de l'écoulement et en appliquant un forçage linéaire isotrope pour générer artificiellement la turbulence loin de la paroi. Le suivi lagrangien de particules permet enfin d'établir un couplage faible entre le mouvement des particules et l'écoulement turbulent. Ces techniques numériques ont été appliquées à la simulation directe d'une couche limite turbulente dans laquelle les particules de taille plus petite que l'échelle de Kolmogorov sont introduites. Les mécanismes de dépôt pour des aérosols ont été analysés et une loi statistique de vitesse de dépôt en fonction du nombre de Stokes a été extraite et comparée à la littérature.

L'ensemble de ces simulations permet une meilleure compréhension des mécanismes de dépôt et de capture, en fonction de la turbulence du fluide au sein de la couche limite et des propriétés des particules. De plus, les résultats préliminaires obtenus pour des particules hydrosols, qui correspondent à des conditions qui prévalent pour des inclusions dans les poches d'acier liquide, ont montré que l'outil numérique peut être appliqué à l'étude quantitative de la capture inclusionnaire aux parois des réacteurs métallurgiques.